Interferometric wavefront sensing for extreme adaptive optics

Oag, Thomas J. D.

Interferometric wavefront sensing for extreme adaptive optics

by Thomas J D Oag

A thesis submitted to the University of Durham
in accordance with the regulations for
admittance to the Degree of Doctor of Philosophy.

Department of Physics
University of Durham
June 2004

Abstract

Adaptive optics is concerned with the correction of phase distortions in wavefronts which degrade the quality of images produced by optical systems. It was originally developed for both astronomy and the military, where the Earth's atmosphere causes distortions, although other uses are now being developed. As ground based telescopes become increasingly large the size and complexity of adaptive optics systems also increase, creating "extreme adaptive optics".

This thesis deals with such an adaptive optics system. A novel self referenced phase shifting interferometer based on a liquid crystal (LC) waveplate is presented which can measure high spatial frequency phase distortions. This is then coupled to a LC spatial light modulator wavefront corrector. The geometry is matched such that there is no need for a wavefront reconstructor.

The performance is measured in two stages. Firstly, spatially where static phase distortions are measured by the interferometer and corrected. Secondly, temporally where a simple analogue feedback is implemented to show correction over a single corrector pixel for fast time varying phase distortions.

This work builds on other published research on using point diffraction interferometry in adaptive optics. The novelty lies in the development of a new implementation of a point diffraction interferometer, and in the demonstration of a high speed closed loop single channel system. This work therefore contributes to the groundwork required to build an extreme adaptive optics system whose complexity scales linearly with the size (area) of the telescope aperture.

Preface

The work reported in this thesis has not been submitted previously for any other degree at the University of Durham or at any other University. The work is the author's own unless otherwise indicated.

A portion of this work has appeared in the following:

- T. J. D. Oag, M. Langlois and G. D. Love
  Wavefront sensing with point diffraction interferometry
  Photon 02, 2-5 Sept, OP5.3.1, ISBN 0-7503-0916-4 (2002)

Acknowledgements

I would like to thank various people who have helped me create this thesis:

Firstly Dr Gordon Love, my supervisor during my time in Durham, without whom none of this would have been possible. Maud Langlois for her knowledge of various interferometers, Andrew Kirby and Sasha Naumov for their knowledge on controlling dual frequency liquid crystals. Chris Saunter and Nirmal Bissonauth for various aspects of computing. Tim Morris for introducing me to the Zygo interferometer.

Various other people who have helped out in some way or another: Graham Murray; Robert Content; Juergen Schmoll; Robin Aspey; John Helly; James and Louisa Turner; Mike Balogh; Dave Gilbank and I should not forget to mention Lucy Broomfield.

My Parents for checking through this thesis and my sister Hannah who has become a different type of doctor during this time. My final mention goes to Esther for being there at the end.

Contents

List of Figures

List of Tables

Chapter 1 | *Introduction*

1.1 Adaptive Optics

Adaptive Optics (AO) is a technique to reduce phase distortions on wavefronts in an optical system and restore plane wavefronts. The technology was initially developed in the 1970's for military applications. More recently the primary focus has shifted to astronomy where the earth's atmosphere causes phase distortions in the incoming wavefronts from astronomical objects. These serve to reduce the resolution of the image in ground based observations. Towards the end of the 1990's the technology has become developed enough so that most large ground based telescopes have some kind of AO system incorporated.

An AO system contains three main components: a corrector which applies the necessary compensation to the wavefront; a sensor which measures the distortions; and a feedback loop which uses the sensor output to control the corrector. The accuracy of an AO system is fundamentally determined by the number of actuators available on the corrector and the resolution of the sensor. Most AO systems operational today have between 100 and 1000 actuators.

1.1.1 Extreme Adaptive Optics

The number of actuators required to obtain a well corrected image scales as the $\lambda^{-\frac{12}{5}}$ power of the wavelength of the astronomical observation and directly with the area of the telescope's primary mirror. Ground based telescopes are becoming larger, with 10m diameter telescopes currently operational. Designs for 30m and 100m diameters exist. The number of actuators required ranges from tens of thousands to a million. Existing AO systems become very difficult to scale up to this

size, and so extreme adaptive optics (XAO) must use new concepts and technology.

This thesis presents an outline for an AO system which could be implemented for XAO. The wavefront sensor (WFS) is derived from a point diffraction interferometer (PDI) and the corrector is a zonal (pixelated) liquid crystal spatial light modulator (LC-SLM). The PDI is a self referenced interferometer overcoming the requirement for a separate undistorted reference beam. The PDI presented employs a novel technique whereby a liquid crystal (LC) waveplate is used to create two simultaneous phase shifted interferograms. The phase is retrieved using a two-step algorithm i.e. by taking the difference between the pair of interferograms. Each individual pixel on the LC-SLM is matched directly to the corresponding area on the interferograms. Each corrector pixel and the corresponding area on the interferograms have no influence on the neighbouring pixels. This implies no need for a wavefront reconstructor. This is ideally suited to extreme AO due to the reduction in computing requirements and because LC-SLMs have the potential for a very large number of actuators.

The aim of this thesis is to test the AO components which could be used to build an XAO system:
Firstly, the spatial performance of this AO system is considered by utilizing 7 pixels on the LC-SLM. Phase distortions are generated which are then measured by the interferometer. The output from the interferometer is used to calculate the required corrective term to restore an undistorted wavefront. The correction obtained is measured by recording the point spread function created by the wavefronts before and after correction.
Secondly, the temporal performance is considered by measuring the correction obtained with fast time varying phase distortions. The AO correction is applied to only one LC-SLM pixel. An analogue electronic feedback is constructed which controls the LC-SLM pixel such that the rms of the phase variation at that pixel is minimized.

1.1.2 Thesis outline

This thesis presents the PDI derived interferometer as a WFS in an AO system and as such:

- Chapter 2 describes the principles behind AO and the components making up an AO system.
- Chapter 3 describes the requirement for extreme adaptive optics. Interferometeric WFSs are then introduced.
- Chapter 4 introduces the interferometer investigated by this thesis. A simulation of the interferometer as a WFS is presented.
- Chapter 5 contains the experimental results to verify that the interferometer can measure phase. The pixelated LC-SLM is then used to induce and correct static phase distortions.
- Chapter 6 contains experimental results when a single pixel is used to correct for fast time varying phase distortions.
- Chapter 7 contains the conclusion and recommendations for future work.

Chapter 2 | *Adaptive optics*

2.1 Introduction

Light from astronomical objects passes through space towards an observer on Earth. The emitted spherical wavefronts can be considered plane as they arrive at the top of the atmosphere. As they pass through the atmosphere air turbulence distorts the phase in the wavefront. The effect of this is to degrade the image quality of telescopes, thereby limiting the resolution obtainable. This effect of the turbulence is referred to as atmospheric seeing. A solution which immediately presents itself is to observe before the wavefronts reach the atmosphere i.e. from space. This has already been achieved with the Hubble space telescope which sits in orbit around the Earth above the atmosphere. The main disadvantage is the cost of both launch and servicing. Another solution is to observe from the ground when the seeing is good, but this limits the time available for observation and the seeing is still poor compared to the diffraction limit. Most large ground based telescopes have been placed at sites where the seeing has been found to be good. A slight variation on this is lucky astronomy where a series of frames is recorded and the frames with good seeing are kept and used to construct the image. This method, although relatively simple, requires more observing time than that required to collect the useful data and observing time is a valuable commodity to the astronomical community. Another drawback of this method is that it is not suitable for spectroscopy. The method of interest in this thesis is that of adaptive optics (AO) where the phase distortions are measured and removed to restore plane wavefronts in real time to improve the image quality.

An AO system consists of three main elements. First, a wavefront corrector which

is able to change its surface profile to cancel out the distortions on the wavefront. This is usually a deformable mirror (DM) although a liquid crystal device is also an option. The phase distortions need to be measured, this is done by the second component, a wavefront sensor (WFS). Thirdly some control electronics are required to take the WFS output and calculate the signals to send to the DM. Figure 2.1

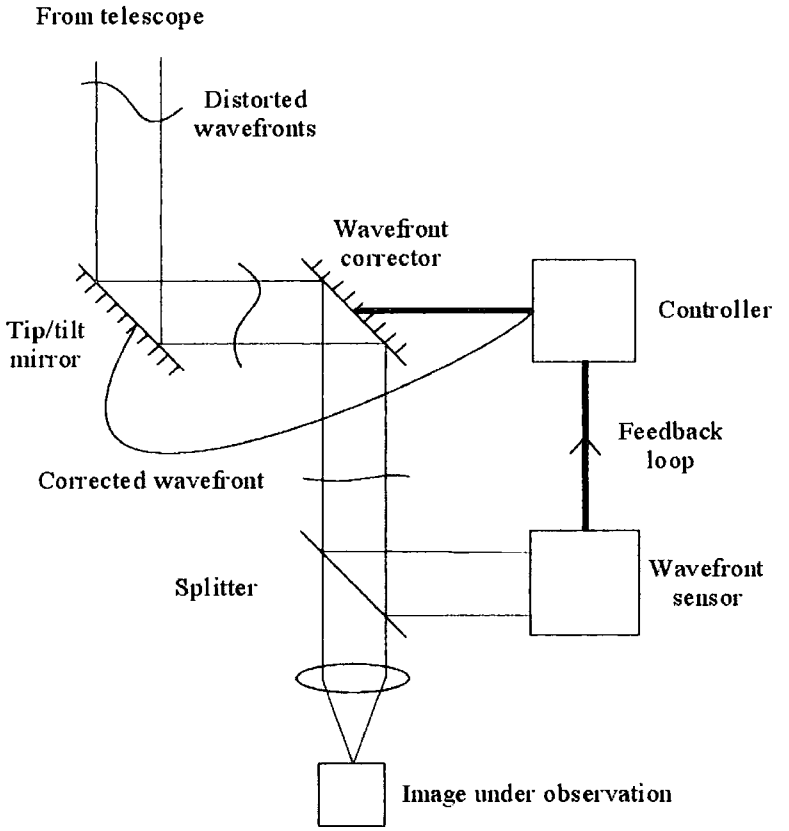

Figure 2.1: *The basic layout of an adaptive optics system, showing the main elements required.*

shows the arrangement of the elements. The additional tip tilt mirror shown is to remove the components of tip and tilt on the wavefront before the DM as these modes usually contain around 90% of the wavefront error and the DMs available usually have difficulty removing this.

For an AO system to operate some photons are required for the WFS which are then not available for observation. The simplest method would be to use a beam splitter to send some of the light to the WFS. This is not employed in astronomy,

as the observer requires all the photons and in many cases the object is not bright enough. A solution which overcomes this is to split the beam spectrally with a dichroic beamsplitter so that the visible light is sent to the WFS while the observation takes place in the infra red. In astronomy however, (and the only method if the object is too dim) the solution is to select a nearby star in the field of view and pickoff all of this light and send it to the WFS. This star becomes a guide star.

It is usual to operate the AO system as shown in figure 2.1 such that the wavefronts are corrected before arriving at the WFS. This is known as closed-loop control. Closed-loop control is preferred as the WFS measured smaller errors and any further errors added by the wavefront corrector are also measured. This setup serves to minimize the overall phase error present on the wavefronts.

The atmosphere is not the only cause of distortions on large telescopes as gravity, thermal and mechanical effects add distortions. These tend to be much slower (≈ 1 Hz) or less. Active optics is used to correct for these low temporal frequency distortions. This has been implemented by using a deformable primary mirror (1) where each segment can move to give the correction, however other methods exist. Adaptive optics deals with the effects of atmospheric turbulence and other distortions of the order 1 Hz to 1 kHz.

This thesis is concerned with AO as a tool for astronomy and the following sections focus on an AO system used in astronomy. AO has found uses in other areas of optics. The principle of operation remains the same, although the optimal method might differ slightly. AO can be used for the correction of a laser beam within a laser cavity (2). Typically high power lasers tend to have poor beam quality inside the cavity due to thermal effects, thus reducing the effect of the gain medium. One mirror can be replaced by a DM and an AO system can improve the beam quality. The AO system can run at a slower speed than required for astronomy although due to high powers the choice of DM is limited. This has been demonstrated on 1 to 10kW CO_2 lasers used for metal cutting. AO allows the retina of the human eye to be imaged at high resolution (3)(4). AO can allow data to be read from below

a distorting layer (such as a multi layer DVD type disk). The problems here are the speed required and due to the laser beam passing through the layer twice some distortions can not be detected so easily. Further uses of AO include line of sight optical communications and underwater imaging. One final military use is where a laser beam is used to destroy a missile (5). AO is required here to maximize the power transfer onto the target. With all of the non astronomical uses the light requirements of the WFS can be less stringent.

2.2 Atmospheric seeing

Meteorlogical and geographical conditions cause eddies of mixed warm and cold air to form in the atmosphere. These cause the refractive index n to vary constantly throughout the atmsophere. As plane wavefronts pass through, the phase, ϕ, at a point will be delayed by

$$\phi = \frac{2\pi}{\lambda}(nd),$$

where d represents the distance traveled through the region and λ is the wavelength.

The atmospheric turbulence can be characterised by Fried's parameter, r_0, given by Fried (6) as,

$$r_0 = 0.185\left[\frac{\lambda^2 \cos(\zeta)}{\int dz C_n^2(z)}\right]^{0.6},$$

where ζ is the zenith angle, $C_n^2(z)$ is the refractive index structure constant and z is the height in the atmosphere. For light at 550nm at zenith r_0 is typically 10cm to 20cm for a site with good seeing. r_0 can be considered as defining an area in the atmosphere done by integrating over z, over which the rms phase variations are 1 rad.

For a diffraction limited image where the wavefronts are ideally plane the resolution obtainable is given by the Rayleigh criterion (7),

$$\Delta\theta = \frac{1.22\lambda}{D}, \tag{2.1}$$

with D as the primary mirror diameter, λ as the wavelenght and $\Delta\theta$ as the minimum angle between two distinguishable objects. For an observation at $\lambda = 550\,\text{nm}$ on a

10m telescope with no distortions present $\Delta\theta = 0.014$". The effect of the turbulence induced distortions is to limit the resolution to

$$\frac{1.22\lambda}{r_0},$$

with r_0 as Fried's parameter from above. This means that the obtainable resolution from a telescope is equivalent to one with a 10 to 20 cm (≈ 1.3" at $\lambda = 550, \text{nm}$) primary mirror regardless of the actual size.

For a diffraction limited image of a point source the point spread function (PSF) produced is the Airy disk, shown in fugre 2.2. This has 95% of the energy in the cen-

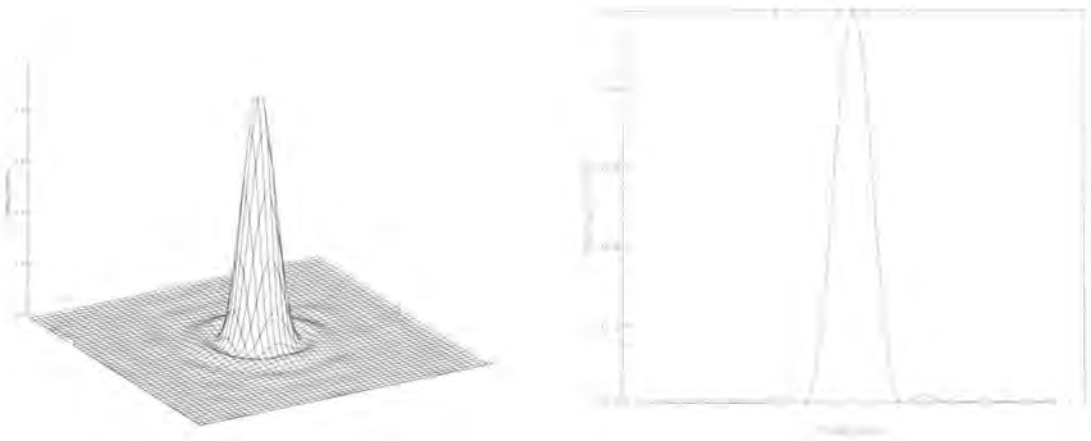

Figure 2.2: *The Airy disk, the resulting PSF for a circular aperture.*

tral peak. The atmospheric distortions generally reduce the intensity and increase the width of the central peak by placing more energy around it. Some examples of the resulting images with phase distortions can be seen in chapter 4. The usual measure of AO system performance is the Strehl ratio. The Strehl ratio measures to what extent the central peak intensity is recovered and is expressed as the ratio of the intensity of the central peak in the distorted image obtained to the intensity that would be obtained in the diffraction limited case,

$$S = \frac{I_{0,dis}}{I_{0,DL}},$$

where $I_{0,dis}$ is the intensity of the peak in the distorted image and $I_{0,DL}$ is the intensity in the diffraction limited case. The Strehl ratio for a typical uncorrected

image is often much less than 1%.

An AO system is said to be well corrected, i.e. close to the diffraction limited case when the Marechal criterion is met. The Marechal criterion is given by,

$$S \geq 0.8.$$

The goal of an AO system is to reach this limit but in reality this is actually a rather difficult target.

When a guide star is used to supply information to the WFS there can be an angle between the guide star and the object under observation. Since the WFS

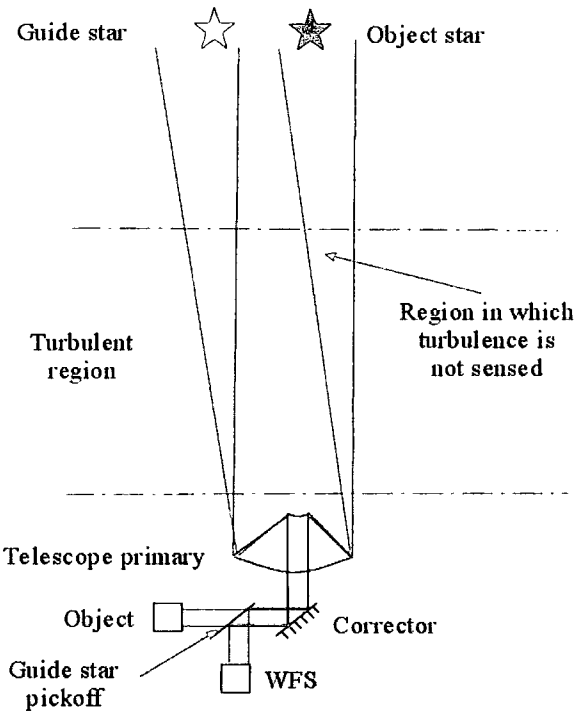

Figure 2.3: *The isoplanatic effect is due to the angle between the guide star and the object star causing a small volume of turbulence to remain undetected by the WFS*

can only measure the turbulence through which the light from the guide star has passed, there remains an area of turbulence where only the light from the object has passed as shown in figure 2.2. When the angle is small, this effect is minimal, but as the angle increases, the quality of correction is reduced. The isoplanatic angle

θ_0 is the maximum angle where the effect can be considered small enough for good correction. θ_0 as given by Fried (8) is,

$$\theta_0 = 0.314\frac{r_o}{H},$$

where H is the average height of the turbulence [1]. The area of sky available for observation around a guide star within θ_0 is called the isoplanatic patch. This limits the field of view available to an observer using an AO system.

Similiary the phase distortions are changing in time. The atmospheric correlation time t_0 is the time over which they can be considered constant (9) is,

$$t_0 = 0.314\frac{r_0}{V},$$

with V as the effective wind speed, given by

$$\frac{\int dz C_n^2(z)|v(z)|^{\frac{5}{3}}}{\int dz C_n^2(z)}$$

where v is the speed of a small region of tubulence.

2.3 Wavefront correctors

The purpose of the wavefront corrector is to restore the wavefront ideally back to a plane wavefront. The corrector is a device which can change its surface profile to that required for correction. The most common method is to use a deformable mirror (DM) which has actuators on one side which change the surface shape. The mirrors need to be able to move by a few microns corresponding to several wavelengths of phase, called the stroke of the mirror. The most common material is piezo electric layer where the shape is changed on application of a voltage. DMs come in three forms, segmented, continuous facesheet or membrane.

A segmented mirror has the reflecting surface made from individual segments which are free to move independently of each other. This is a zonal device as each segment only effects the local surface and has no effect on the neighbouring segments.

[1] If the turbulence was all contained within a thin layer, then H would be the height of this layer from the telescope. In reality H is a weighted average.

Each segment can be controlled by one actuator (piston only) or by three actuators allowing piston, tip and tilt for each segment. This mirror has the advantage that it is easy to control, but there are edge effects between the segments.

Figure 2.4: *Diagram of a deformable mirror: (a) segmented where each segment is free to move in piston, tip and tilt; and (b) where the actuators push and pull at the surface to change the shape.*

A continuous facesheet mirror has no gaps in the reflecting surface. There are different kinds of continuous mirrors available. The first of these is similar to the segmented mirror, but with no actual segments. In this case, the actuators pull on the surface, so changing its shape. Continuous mirrors are modal systems as each actuator influences the entire surface. The influence function[2] of each actuator must be known so that the desired shape can be applied, making these mirrors harder to control than the segmented variety.

The bimorph mirror is another continuous mirror (10). This has a piezo electric layer the same size as the reflecting surface. On one side there is a common electrode with the reflecting surface on top and below there are individual electrodes forming the actuators. When a voltage is applied between one electrode and the common one the piezo electric layer will change shape depending on the applied voltage and so cause the mirror to change. This mirror can be controlled directly by certain wavefront sensors negating the need for complex control.

The membrane mirror (11) consists of a thin membrane of aluminum or titanium

[2]The influence function of an actuator describes how the surface shape changes when a voltage is applied to that actuator.

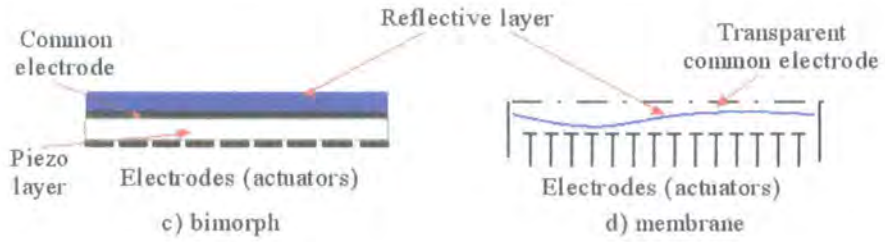

Figure 2.5: *Additional types of DM: (c) Bimorph where the piezo layer changes the shape due to voltages applied; and (d) membrane where the thin reflective membrane is deflected by voltages applied to the electrodes.*

with a transparent continuous electrode above it and individual electrodes etched onto a circuit board below it. When a voltage is applied, the membrane is deflected slightly. These mirrors can have a large number of actuators as the electrodes are often on $50\mu m \rightarrow 100\mu m$ apart and they are very fast. However the stoke tends to be much lower, perhaps of the order of $\frac{\lambda}{2}$. It has been established that the layout of the actuators on the mirror is not a concern for 40 actuators or more (12). Membrane mirrors can be used to make inexpensive AO systems (13).

A liquid crystal (LC) device can also be used as a wavefront corrector. Amplitude modulating liquid crystals are common in displays, however a LC can be constructed that allows phase only modulation. The DMs detailed so far have all operated by changing the physical distance the wavefront travels while a LC functions by varying the refractive index when a voltage is applied across the LC material (14). A LC corrector has many piston only pixels or actuators. LC correctors are zonal with a boundary between each pixel similar to a segmented mirror. LC correctors are of particular interest here as they couple very neatly to interferometry as the WFS. LC wavefront correctors will be covered in detail in chapter 3.

2.4 Wavefront sensors

Retrieving the phase from the wavefronts is non trivial as the phase information is lost when the image is formed. The image $I(x, y)$ when a point (u, v) in the initial

wavefronts is imaged is (15)

$$I(x,y) = \mid FFT(A(u,v)e^{i\phi(u,v)}) \mid^2,$$

where FFT denotes a Fourier transform. A and ϕ are the amplitude and phase of the initial wavefronts and x, y and u, v are the spatial coordinates in the image and initial wavefronts respectively. The entire image is then formed by summing over all of the points (u,v). Given that the we know $I(x,y)$ from the observation ϕ cannot be determined exactly. The wavefront sensor is used to measure the phase before an image is formed.

The first WFS to be used in AO was the shearing interferometer (16). In shearing interferometry the beam containing the distorted wavefronts is split in two and one of these is then sheared laterally by a small distance relative to the other. On recombination an interferogram is formed in the region of overlap and the fringes give a measure of the wavefront slope. The actual distortion can be calculated from the slope measurements. In order to gain all the information, two perpendicular shears are needed. This means the initial beam must be split into two before shearing. Shearing interferometry is not common in astronomy for the following reasons: A brighter guide star would be required to supply enough light for the pair of shears, Shearing interferometry works best with monochromatic light and the control hardware requirements tend to be quite complex. Two other methods for creating the shear exist, radially and rotationally.

The Shack Hartmann (SH) WFS is similar to the shearing interferometer in that it measures the slope of the wavefronts. In this system the wavefront is split into multiple sub-apertures by a lenslet array as shown in figure 2.6. Each lens focusses light from that region of the wavefront which is imaged by a CCD array or a quad cell[3] per lenslet. The effect of any wavefront slope in any sub-aperture is to shift the position of the resulting spot from that produced from a plane wavefront where a square array of spots is produced. The displacement of the spot from the plane

[3]A quad cell is a 2x2 sensor, with the spot imaged in the centre. The displacement is measured by the relative intensity of the spot in each quadrant

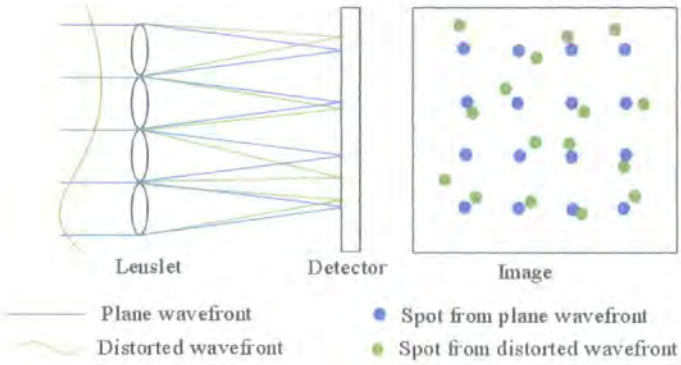

Figure 2.6: *The optical layout of the Shack Hartmann WFS. Each individual lenset images a small section of the wavefront and the displacement of the resulting spot is a measure of the slope on the wavefront at that point.*

wavefront position is a measure of the slope on the wavefront in the related sub-aperture. The Shack Hartmann is useful in that it is a relatively simple device to design and use, and it can be used for extended sources. The SH is the most common WFS used.

The curvature sensor (CS) was first described by Roddier (17) (18) as a method of measuring the curvature or the second derivative of the phase distortions on the wavefront. Figure 2.7 shows the curvature sensor. The intensity of the beam is

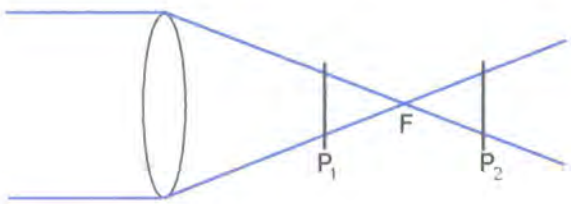

Figure 2.7: *The optical layout of the curvature WFS. The intensity is recorded at two points P_1 and P_2 equidistant either side of the focus F. The difference in intensity in the equivalent point in each is a measure of the curvature at that point*

measured at planes P_1 and P_2, which are placed equidistant from the focus F. A

plane wavefront has the same intensity profile at both P_1 and P_2. Phase distortions cause the intensity measured at P_1 and P_2 to be different, with this difference measuring the curvature. Around the edge of the aperture, the tilts are measured. The wavefront is then calculated by solving the Poisson equation across the wavefront using the edge tilts as the boundary conditions. An actual CS system might use a vibrating membrane to produce P_1 and P_2 alternatively on the same camera. The advantage of the CS system is that the output can be used to control directly certain wavefront correctors (usually a bimorph mirror) without first calculating the distortions. The disadvantage is the CS is a more complex method requiring more computing when this is not the case. A comparison between the SH and CS systems can be found in Rigaut (19) for astronomical AO.

An alternate WFS is to use interferometry to image the phase distortions directly by converting them to amplitude modulations. Interferometry is the usual test method in the laboratory. In conventional inteferometry this is achieved by interfering the distorted wavefronts with coherent plane ones. This is achieved by firstly splitting an undistorted beam, passing one through the medium and recombining them so as to produce an interferogram of the phase distortions. In this form this is unsuitable for astronomical AO as the plane wavefronts are not available. A method first described by Smartt (20) shown in figure 2.8 uses a small pinhole to filter spatially the beam to generate the plane wavefronts, while a semi transparent mask allows the distorted wavefronts to pass through and thereby combine with the plane wavefronts. This method forms the basis of the interferometric methods explored by this thesis and are described in more detail in chapter 3.

The WFS outlined above represent the main ones used for AO, but there are alternative methods. The Pyramid WFS (21) uses a small square based pyramid placed in the focal plane with the focus on the apex. This splits the telescope beam into 4 sub beams where the pupil is imaged in each beam. For plane wavefronts the 4 images will be identical. Any wavefront slope will cause the beam focus at that position on the wavefront to be slightly shifted relative to the pyramid tip so the light is not split evenly into the 4 beams. The slope can be measured from the

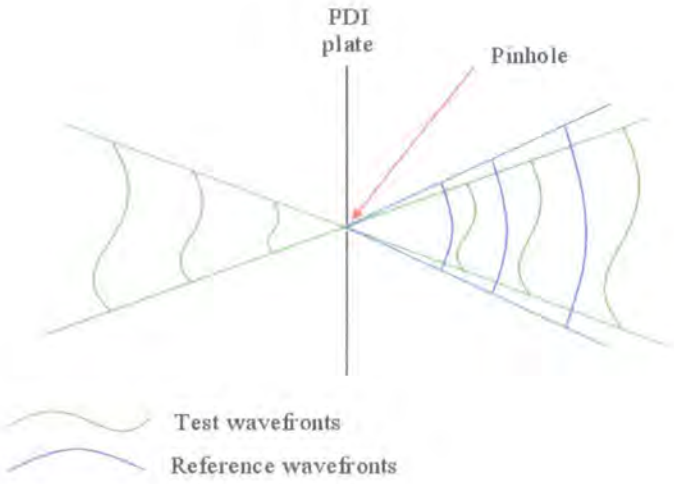

Figure 2.8: *The point diffraction interferomter first described by Smartt (20). A small pinhole spatially filters the beam to generate plane coherent wavefronts, while the semi transparent mask allows the distorted wavefronts to pass through*

differences in intensity on the 4 images. Since the beam is split into 4 this means that both x and y slopes can be measured simultaneously. This system is not yet in widespread use for astronomical AO.

2.5 Control

The function of the control loop is to calculate the signal required to send to the DM so it takes on the best shape for correction.

The mirror influence matrix describes the shape the mirror will assume for a given set of signal voltages. Each actuator has its own influence function which describes how that actuator changes the surface. All these influence functions are combined to create the influence matrix $\mathbf{M}$ where,

$$\phi = \mathbf{M}\mathbf{x},$$

with ϕ as the surface shape of the mirror and $\mathbf{x}$ as a vector of control signals sent to the mirror.

Similarly the WFS response matrix **S** describes the signals received from the WFS,

$$\mathbf{s} = \mathbf{S}\phi_0,$$

with **s** as the vector of signals from the WFS and ϕ_0 as the actual wavefront distortion measured. ϕ_0 is not the distortion present on the wavefront on arrival as the wavefront has already been corrected by the corrector.

The objective is to calculate the required control signal **x** from the WFS signal **s**. This operation can be summarized to

$$\mathbf{x} = \mathbf{C}\mathbf{s} \tag{2.2}$$

where **C** is the control matrix and is a combination of both **M** and **S**. A curvature sensor coupled to a bimorph mirror will operate in this way. Before an AO system can work, the control matrix **C** must be determined. Various methods exist. The least squares method works by applying a signal to each actuator and then recording the response **s**. The control matrix is then the pseudo-inverse of the resultant matrix. This is easy to implement, but it is not necessarily the best as it assumes no knowledge of the initial wavefront distortions. A more optimal method is to minimise the actual wavefront error after correction, equivalent to maximizing the Strehl ratio (22). This requires knowledge of **M** and **S** beforehand.

If the actual wavefront phase is required, the wavefront is reconstructed from the WFS output **s**,

$$\phi_r = \mathbf{R}\mathbf{s},$$

with ϕ_r as the reconstructed wavefront and **R** is the reconstructor matrix. Ideally $\phi_r = \phi_0$. This can be used as a measure of the performance of various WFS.

2.6 Guide stars and sky coverage

One major requirement for astronomical AO is that the WFS uses as few photons as possible. However wavefront sensing requires more photons than are available from the object necessitating the use of a guide star. The WFS requires $\approx 10 - 100$

photons per detector element per exposure corresponding to a star of magnitude 10 or brighter (23). One of the major drawbacks of AO for astronomy is the limited number of bright stars available. Since one can only observe in the isoplanatic patch associated with the guide star this severely limits the sky coverage for an observer.

A method to increase the available sky coverage is to create an artificial guide star in the desired isoplanatic patch on the sky. This is achieved by firing a laser up and using the back scattered photons as the guide star. This is called a laser guide star (LGS). There are 2 principal types: a Rayleigh beacon and a sodium beacon.

With the Rayleigh beacon a pulsed laser is fired up and focussed at height of about 10 to 20km. Rayleigh scattering from the atmosphere then returns some of the photons which are used for the WFS. An optical shutter is used to select only those photons with a round trip time corresponding to the selected beacon height. The disadvantage with this method is that due to the finite height of the

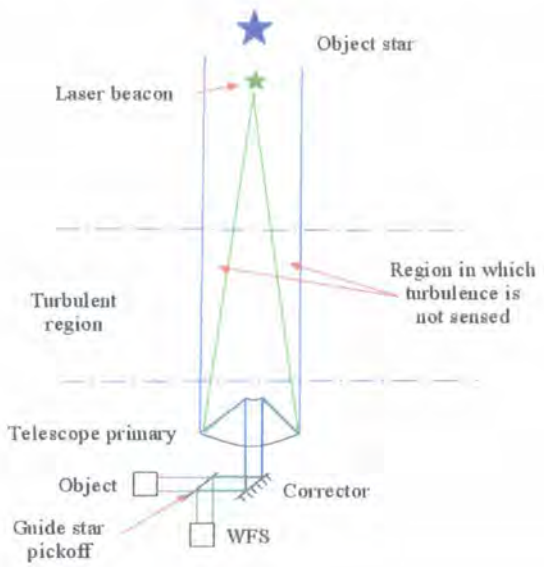

Figure 2.9: *The cone effect caused by the guide star not being at an infinite height causing a conical shaped region of turbulence sampled. This effect is reduced for higher guide stars.*

beacon the returning wavefronts from the laser beacon do not pass through all of

the turbulence traversed by the object wavefronts. This is called the cone effect or focal anisoplanatism and is shown in figure 2.9. This effect is reduced if the beacon height is raised. This also means there is less turbulence above the beacon which is not detected at all. Since the Rayleigh beacon is limited in how high it can go, the sodium beacon offers an alternative method to produce a higher beacon.

The sodium beacon (24) uses the existence of a thin layer of sodium vapour at about 90km accumulated from meteors and volcanic events (25). Although there are other atoms present in this layer, sodium is chosen as it has a large cross section making it the easiest choice to excite. The laser is tuned to the sodium D line at 589nm (26). This excites the layer causing it to fluoresce creating the sodium beacon. This requires a less powerful laser than a Rayleigh beacon at this height would require. The lasers required, however, are more complex than those used in the Rayleigh beacons.

Both methods suffer from tilt reciprocity (27) where the wavefront tilt cannot be measured from the light returning from the laser beacon. This is because the tilt component picked up on the way up is cancelled on the way down. This is a serious problem as without correcting the tilt the effectiveness of an AO system is poor. This means that a guide star is still required but it can be fainter than one which is used for full correction. An alternate solution suggested is to use a dual wavelength laser (28) where on reaching the target layer the two wavelengths combine to produce photons of a new wavelength such as for sodium 589nm and 569nm which would produce a new wavelength at 330nm. These then only pass through the region once allowing tilt to be measured. This requires a very powerful laser to operate, more powerful than can be realistically used on an astronomical site.

Another new concept in AO is multi conjugate adaptive optics (MCAO) (29). This aims to increase the size of the isoplanatic patch such that the corrected field of view is larger. This is achieved by using multiple wavefront correctors and corresponding WFSs to correct for different layers of turbulence in the atmosphere. Each corrector is placed in the conjugate plane to that of the turbulence layer corrected.

This requires multiple guide stars to operate and so is closely linked to laser guide stars.

2.7 Extreme AO

All large ground based telescopes (the largest today are 8 to 10m diameter) now either have an AO system in use or are developing systems for use. As has been shown AO is required to obtain the full resolution available from using large primary mirrors. Not being satisfied with telescopes of this size ground based astronomers are proposing even larger telescopes or "extremely large telescopes" (ELTs). One example proposed at this time is the giant segmented mirror telescope (GSMT) (30) which would have a 30m primary mirror. An even larger scale has been proposed by the European Southern Observatory (ESO) the overwhelmingly large (OWL) telescope which would have a primary mirror of 100m (31), which represents a major engineering challenge just to build a structure to mount this mirror on. Figure 2.7 shows how the telescope site could look. These telescopes would enable astronomers to see even fainter objects in the universe and would have the potential to see directly planets around nearby stars (33) (34). Without AO the performance of these huge telescopes will be severely limited. Extreme AO deals with AO systems which would be suitable for these telescopes.

Another use for Extreme AO is to implement an AO system on an existing telescope such as those with 8 m or 10 m diameter mirrors. These AO systems would have many more actuators per unit area than existing AO systems on these telescopes. These could then also be used to search for extra solar planets.

This thesis discusses the use of interferometry as a WFS for an AO system. Interferometry has the potential to be a powerful tool for extreme AO as the number of output channels available (and hence the number of actuators which can be employed) is determined by the number of CCD pixels used to image the interferogram. CCDs containing millions of pixels are commonplace today. This is also important because an interferometric WFS is well matched to a LC wavefront correctors with

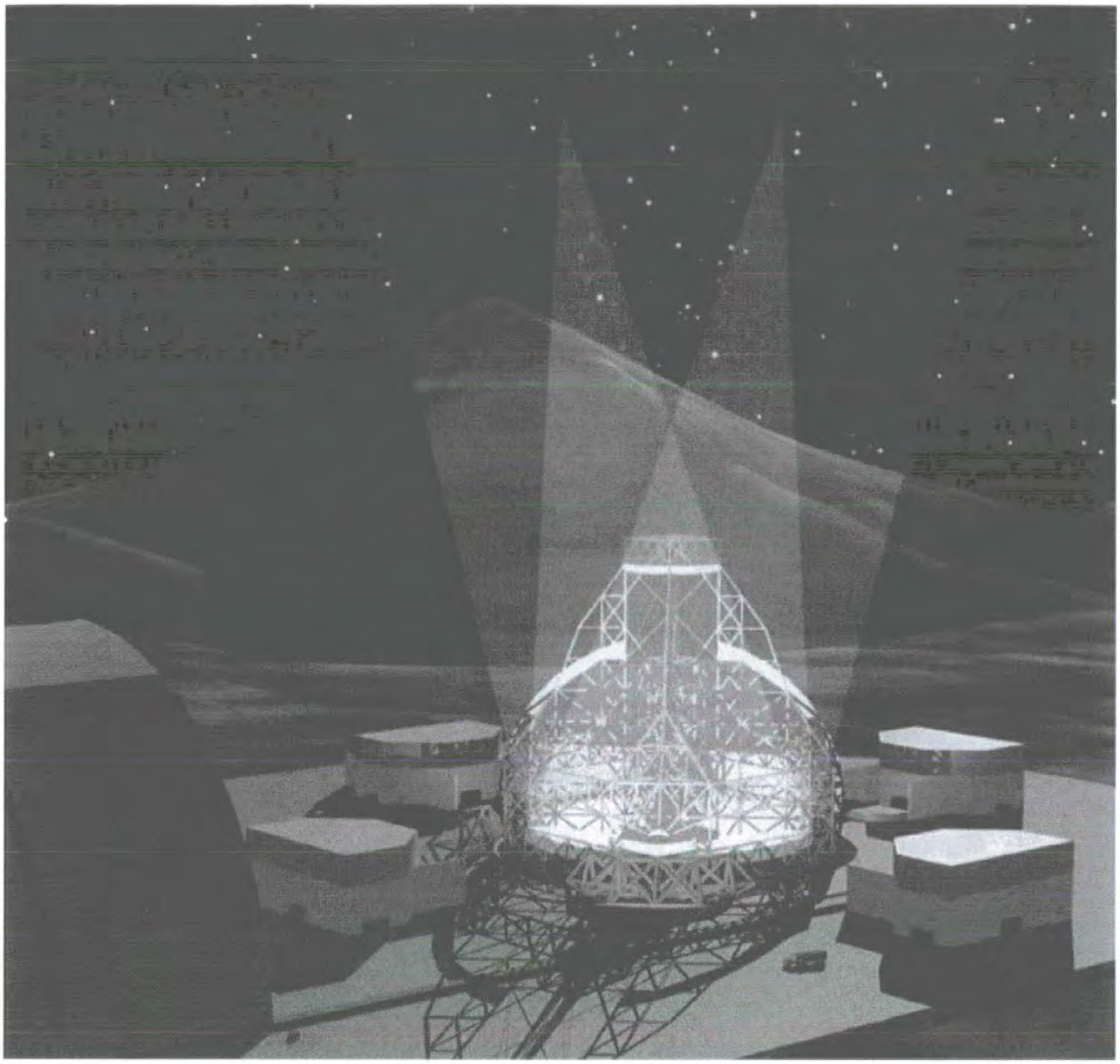

Figure 2.10: *An impression of what ESO's OWL telescope could be (32).*

a large number of actuators.

Chapter 3

Extreme Adaptive Optics and Interferometry

3.1 Extreme Adaptive Optics

3.1.1 High resolution visible imaging

In order for an AO system to deliver good correction it is considered that one corrective actuator is required for every unit of r_0 on the telescope primary (23). Therefore,

$$N = \left(\frac{D}{r_0}\right)^2 \tag{3.1}$$

where N is the number of actuators required, D is the diameter of the primary mirror and r_0 is Fried's parameter.

For a telescope with a 8 m primary mirror, to achieve correction in the visible region,

$$N = \left(\frac{800}{10}\right)^2 = 6400 \tag{3.2}$$

6400 actuators are needed for good correction. r_0 has been taken as 10 cm, representing a typical value for visible wavelengths. This is not an exact calculation and it can vary depending on what type of corrector is employed. If the seeing is worse, such that r_0 is halved then one would require 4 times as many actuators.

The number of actuators required also depends on the wavelength of the obser-

vation as r_o is dependent on the wavelength λ,

$$r_0 \propto \lambda^{\frac{6}{5}} \tag{3.3}$$

For IR wavelengths r_0 is typically 20 cm to 50 cm which reduces the required number of actuators by up to 25 times. For this reason many larger telescopes offer AO correction for IR observations. For a $100m$ telescope in the IR,

$$N = \left(\frac{10000}{50}\right)^2 = 40000 \tag{3.4}$$

40000 actuators would be required. This has assumed a value of 50 cm for r_0. AO capable of correcting on a scale of $r_0 = 12$ cm has been achieved on 3 m telescopes (35) (36) for visible observations.

For visible correction on a 100 m telescope, 1 million actuators would be required. The control loop needs sufficient information to drive the corrector. This requires one output channel from the wavefront sensor (WFS) per actuator. In the case of a Shack Hartmann (SH) WFS each lenslet outputs 2 channels as they measure both x and y slopes simultaneously. Extreme AO deals with developing AO systems with $> 10^3$ channels.

3.1.2 Extra solar planets

An active area of research in astronomy is the detection of planets orbiting stars outside of the solar system (37)(38), so called extra-solar planets. Radial velocity surveys have inferred the presence of bodies orbiting nearby stars. Very small Doppler shifts in the light from such stars have shown the star to be wobbling, most likely caused by the gravity of an orbiting companion. The size and frequency of the wobbles lead to an estimate of the size and orbital period of the companion. In rare cases the planet passes directly between the Earth and the host star which will cause a dimming of the host stars light. Out of many 100s of inferred extra solar planets only two have been observed (39) making a transit. This knowledge allows the size and orbital period to be more accurately estimated. One can also gain some information on the planet's composition by detecting specific spectral lines absorbed from the hosts star's light during transit.

A major goal in the search for extra solar planets is to detect directly some light from the planet itself and to ultimately record a spectrum. The extreme contrast ratio between the planet and host star makes direct detection extremely challenging. If such a planet could be imaged and a spectrum recorded, then information regarding the planet's orbital parameters, size, temperature, chemical composition and the presence of chemicals which could indicate signs of life could be detected. Extreme AO has the potential to allow large ground based telescopes to image directly faint star companions.

The number of actuators on the wavefront corrector directly relates to the spatial frequencies which the system can correct. AO systems generally correct the lower spatial frequencies well. The effect of this is to increase the peak intensity and decrease the width giving an increase in resolution. The high spatial frequencies remain uncorrected, and the effect of these are to scatter energy into a halo around the central peak. The extreme contrast ratio between planet and host star means that the planet can easily remain undetectable within this halo even if the AO has the required resolution to resolve the planet from the host star. This halo intensity becomes the limiting factor to detecting faint companions and means AO systems require more actuators than shown by equation 3.1 for superlative correction.

Extreme AO is a worthwhile development for planet searching even without these new designs for 30 m and larger telescopes. A well corrected 8 m telescope has the potential to directly image an extra solar planet. Consider a planet in a 1 AU orbit around a host star 20 pc away. This represents one of the nearer extra solar planets known. The angular separation ($\Delta\theta$) of these 2 objects is

$$\begin{aligned} \Delta\theta &= \frac{1\,\mathrm{AU}}{20\,\mathrm{pc}} \\ \Delta\theta &= 2.424 \times 10^{-7}\,\mathrm{rad} \end{aligned}$$

using the small angle approximation, $\sin\theta \approx \theta$. From the Raleigh criterion (equation 2.2) the minimum diameter telescope (D) required to resolve 2 objects sepa-

rated by this angle at a wavelength of $\lambda = 550\,\text{nm}$ is

$$\begin{aligned} D &= \frac{1.22\lambda}{\Delta\theta} \\ D &= 2.77\,\text{m} \end{aligned}$$

This shows that a 3 m class telescope could resolve these in the diffraction limited case. However the extreme contrast ratio between host star and planet mean that even the slightest amount of distortion means that the planet can not be observed in the image due to the halo from the host star. An Extreme AO system could be implemented on a smaller telescope to provide sufficient spatial correction such that these planets could be observed.

3.1.3 Extreme AO systems

A conceptual AO system in the design stage is the Extreme Adaptive Optics Planet Imager (XAOPI) (40) for the 10m W. M. Keck telescope in Hawaii. This is an AO system specially designed for high contrast imaging required for imaging faint star companions with a target Strehl ratio of 93%. The aim is to answer scientific questions such as the population of extra solar planets in wide (< 5 AU) orbits around nearby stars which are difficult to probe with the techniques outlined above. For high contrast imaging it is important to get good correction of the mid range spatial frequencies as they cause energy to be scattered into the halo where the planet's image exists. AO systems have the WFS operating in a plane conjugate to the system pupil. A drawback of the WFS in this pupil plane is that the finite sampling can impose aliasing where uncorrectable high spatial frequencies are detected as mid range spatial frequencies which cause correction errors significant for high contrast imaging due the the effect on the halo.

Figure 3.1 shows the proposed layout for the AO system. The wavefront corrector is to be a 4096 MEMS deformable mirror (DM). The MEMS design allows for a compact DM due to the actuator spacing being $300\mu m$. A 1024 version already exists (41), and a 4096 version would be constructed by scaling the current 1024 actuator design. A larger version would require a redesign of the driving electronics. The limited stroke available from a MEMS would require an additional DM

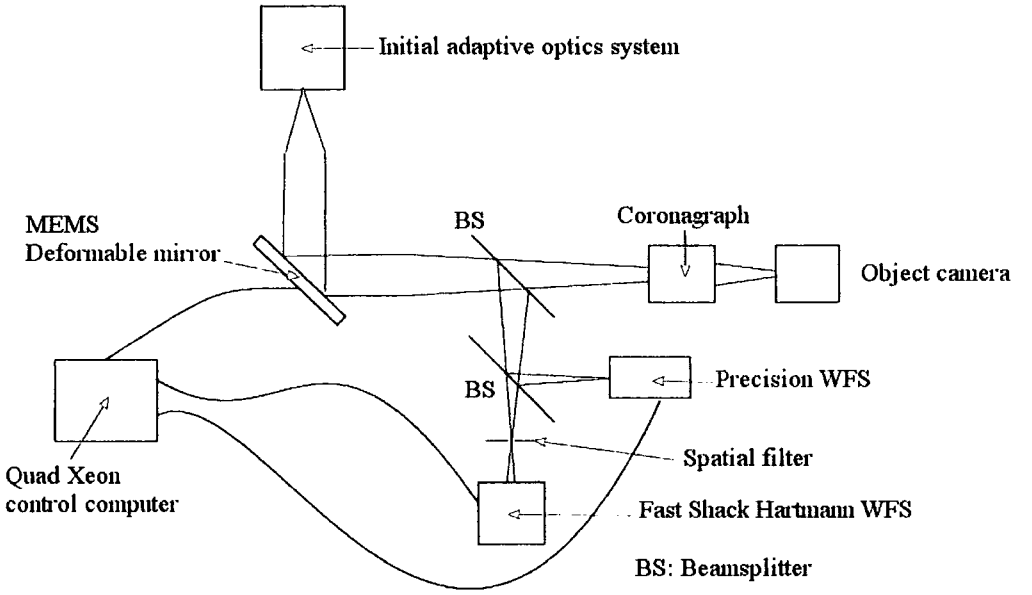

Figure 3.1: *The layout for the proposed XAOPI system*

to remove larger distortions. An initial stage AO system will perform this. The WFS will be a spatially filtered Shack Hartmann (SH). The spatial filter removes the high spatial frequencies which are not corrected by the MEMS DM thereby overcoming the aliasing problem described above. High spatial frequency induced by the boundaries of the primary mirror segments are also removed. The SH will consist of a 128x128 CCD with a 2x2 sensor per SH spot. A larger CCD would not meet the readout noise and framerate requirements. The design also allows for a high precision WFS which will operate much more slowly using a small fraction of the light. This could be a Mach Zehnder (see later) interferometer. This would produce a time averaged absolute wavefront measurement would could be used to update the SH output. A coronagraph is provided to mask out the light from the host star. The contrast ratio between the host and companion is likely to be 10^7 to 10^8. On the control side classic wavefront reconstruction techniques scale computationally as N^2 with N being the number of WFS channels. In order to keep the computational requirements lower a new Fourier based reconstructor (42) which scales as $N \log N$ could be employed.

3.2 Liquid Crystal wavefront corrector

Liquid crystal (LC) spatial light modulators (SLMs) have the potential to be used as wavefront correctors for extreme AO, as they can be produced with large numbers of actuators. The nematic liquid crystal (NLC) state is of the most interest for AO as this can produce a continuous phase change controlled by a voltage applied to the cell. The NLC shown in figure 3.2 consists of LC molecules between a pair of glass

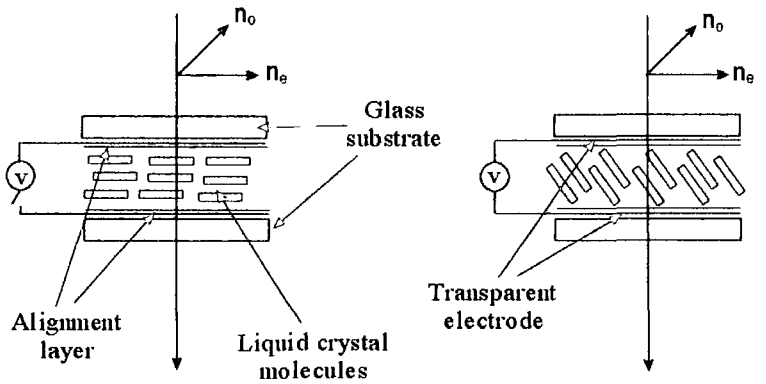

Figure 3.2: *A nematic liquid crystal cell. Applying an AC voltage causes the molecules to rotate and changes the refractive index (n_e) experienced by light polarized along the extra ordinary axis. When no voltage is applied the molecules will align themselves with small grooves present in the alignment layers.*

plates. The alignment layer is a thin layer of nylon or polyamide which is buffed in one direction. This will leave small grooves which cause the LC molecules to align with them. The electrode is created from a thin layer of indium tin oxide which is transparent. Applying an alternating voltage ($\approx 100Hz$) to the electrodes causes the LC molecules to rotate by an amount proportional to the voltage applied. The effect of the molecules rotating is to change the effective refractive index of the extra ordinary polarization axis (n_e), and hence the optical path length of light polarized along the extra ordinary axis. The phase shift is polarization dependent as only n_e varies while the refractive index along the ordinary axis (n_o) remains unchanged. Thus each NLC pixel is a waveplate with an electrically controllable retardance. Polarization insensitive operation has been achieved in one of two methods. The

first is to use two NLC layers with orthogonal optical axes such that the initial unshifted n_o plane then becomes n_e and is phase shifted in the second layer (43). The second method is to place a mirror behind the LC layer with a quarter wave plate in between. This setup rotates the polarization plane by 90^o before passing through the LC a second time (44). The effect of both methods is to vary n for both axes providing identical phase shifts. The effect of varying n is optically equivalent to varying the physical path of the light as with a deformable mirror (DM). A review of the issues concerned with using LC correctors in AO has been conducted by Bold (45). Other LC states exist such as the ferroelectric LC, however these are generally of less interest for wavefront correctors as it is not so simple to achieve variable phase modulation. LC wavefront correctors are small and inexpensive compared to a DM with the equivalent number of actuators. Presently LC devices with over a million pixels exist as displays so a wavefront corrector of this size is not unfeasible. A DM of this size would be much more challenging to create although a MEMS DM could provide an alternate wavefront corrector of this size. LCs also require much lower operating voltages than those required by a DM and since there are no physical moving parts they have the potential to be more reliable than their DM counterparts. A drawback to using LCs, especially the NLC, is the speed of operation. When a voltage is applied the molecules rotate quickly but when the voltage is switched off the molecules then relax back to the orientation defined by the alignment layer. As there is no driving force for this operation the time required to relax back is much slower requiring 10s of msec, too slow for AO. Advances in LC technology have found that by applying a high voltage high frequency (10s kHz) briefly to the cell forces the molecules into the relaxed state. These dual frequency LCs are suitable wavefront correctors for AO (46). A NLC wavefront corrector is composed of many individual NLC cells as shown in figure 3.2, each having piston only correction.

3.3 Reconstructor free AO

In AO it is important to match the wavefront corrector to the WFS. The aim is to reduce the complexity of the control section. The WFS/corrector pair is usually

chosen such that the the modes detectable by the WFS match those which can be corrected by the wavefront corrector. For instance, a SH WFS and a segmented mirror are a matched pair as the SH detects tip and tilt which the segmented mirror corrects. A curvature sensor is matched to a bimorph mirror in the same manner. In certain situations it is possible to take the WFS signals and send them directly to the corrector without explicitly reconstructing the wavefront in between. For extreme AO it is required that the corrector has a large number of actuators such as in a LC described above. The ideal WFS matched to a piston-only LC SLM is interferometry as it directly measures the phase. The interferogram is measured by a CCD camera where each camera pixel samples a small region of the phase. The camera and LC SLM geometries are then matched allowing every camera pixel to control the corresponding pixel on the corrector. This creates an entirely zonal system, as each pixel has no influence on the neighbouring ones. This method is reconstructor free as the entire wavefront is never considered as a whole. The control matrix C discussed in chapter 2 becomes diagonal.

3.4 Interferometry

Interferometry enables the phase distortions present on a wavefront to be imaged directly as amplitude modulations in an interferogram. The intensity at any point in the interferogram gives the phase at that point on the wavefront. In a conventional laboratory based interferometer a beam is divided and one beam is passed through the medium under test, the other remains undistorted and becomes the reference beam as shown in figure 3.3.

For an AO system this reference beam must be created from the incoming wavefronts. On such method is the Smartt or point diffraction interferometer (PDI) (20) illustrated in figure 2.8 in chapter 2. A pinhole is surrounded by a semi opaque mask such that the wavefronts are spatially filtered to create coherent reference wavefronts meanwhile the distorted wavefronts can pass through the surrounding region becoming the test wavefronts. These then travel coincidentally and combine to form an interferogram containing the phase information. This setup is a com-

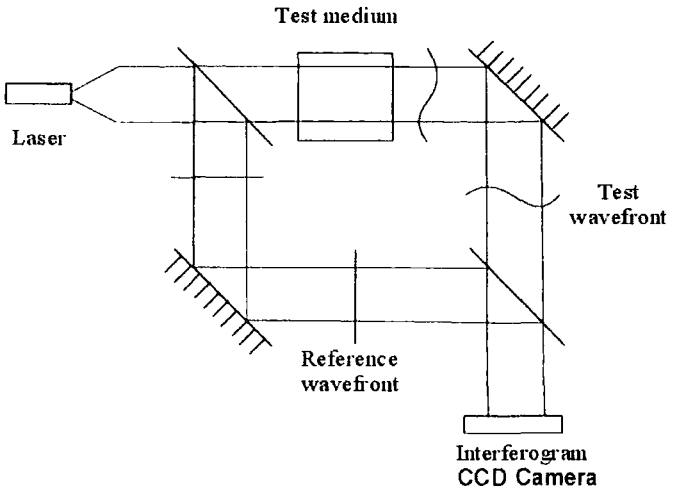

Figure 3.3: *A Mach Zehnder interferometer used to measure the phase distortions caused when a laser beam passes through the test medium*

mon path interferometer as both the reference and test wavefronts follow the same path throughout. Any external phase distortions such as vibrations then effect both beams together and do not show in the interferogram. This common path aspect also makes the PDI much easier to setup and align than the two beam setup where the length of both paths must be the same. A slight modification to the original design is to replace the pinhole by a transparent screen with the pinhole formed by a phase discontinuity of a different optical path length to that of the surround. This is similar to the Zernike phase contrast technique. This phase only design has the same effect in that it generates reference wavefronts while allowing the test wavefronts to pass unfiltered, however it has the advantage of greater light efficiency. The contrast of the interferogram is maximized when the relative intensities of both beams are the same. A filter could then be placed in the surrounding region to attenuate the test beam to the best intensity.

The quality of the interferograms is affected by the size of the pinhole used for the spatial filtering. The best contrast is obtained when the intensities of the test and reference beams are the same. However the accuracy of the interferogram is increased as the pinhole is made smaller. This is because a smaller pinhole produces a better reference wavefront by removing more of the distortions. When selecting

the size of pinhole to use there is a trade off between the accuracy and the contrast of the interferogram.

When measuring the phase from the resulting interferogram there are three unknowns: the amplitude of the test beam; the amplitude of the reference beam; and the phase distortions which contain the useful information. The intensity of the interferogram is measured to retrieve the phase. In order to determine accurately the actual phase distortions present on the initial wavefront exactly the interferogram should be measured while changing the overall phase difference between the test and reference beams in a known manner. With three unknowns to determine three separate interferograms are required each with a different phase shift. This is achieved by altering the path length of either the test or the reference beam. The sign along with the magnitude of the phase distortions is automatically determined, while with just one interferogram it is not. It is often possible to measure two separate phase shifted inteferograms and the remaining unknown can be determined experimentally before one begins to measure unknown phase distortions. The next section introduces various methods for producing varying phase shifts and retrieving the phase information from the interferograms. Phase shifting interferometric methods allow the phase to be recovered over a 2π range. For phase distortions greater than this phase shifting interferometry can not detect the absolute value and a 2π ambiguity occurs without "stitching". An interferometric AO system would most likely require a previous AO system capable of removing large low order distortions leaving distortions of less than 2π. Although phase shifting interferometry is desirable, AO systems using just a single interferogram have been produced (47) (48).

3.4.1 Phase shifting PDI

The PDI setup described so far does not offer phase shifting interferometry as the reference wave is generated from the test wavefronts with no simple way of inserting a variable phase shift between them. Phase shifting has been incorporated by placing a transmission grating in contact with the pinhole mask and translating the

grating with respect to the pinhole, as reported by (49).

A method reported by (50) splits the initial beam containing the distorted wavefronts into 2 beams with a small angular separation between them. The beams are focussed onto a mask containing a small pinhole and a larger transparent window as shown in figure 3.4. The beams are focussed into the centre of the pinhole and

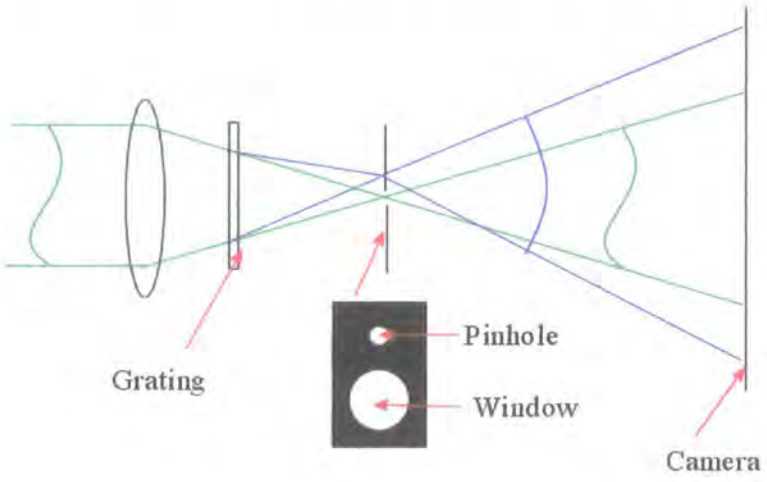

Figure 3.4: *A method for achieving phase shifting interferometry by separating the two beams and applying a phase shift to one.*

window respectively. The pinhole serves to create the reference beam in the usual way while the window being much larger allows the test beam to pass through without any significant filtering. A coarse grating is used as shown to split the beam initially. The separation of the beams must be large enough to prevent any overlap. If the separation is too small then a portion of the beam illuminating the pinhole can be transmitted via the window causing extra unwanted interference. However as the separation is increased the interference fringes become closer together making it harder to extract the phase from the interferogram. The beam division enables a phase shift to be applied to one beam relative to the other. This can be achieved by using the grating to provide the division. Translation of the grating by one grating period then introduces a first order phase shift of one full cycle. As the grating is physically moved the actual path length that the different orders pass through

changes. This is used to provide one beam where the phase can be shifted while the zeroth order transmitted beam (which passes straight through the grating) whose phase remains constant can provide the other.

3.4.2 Liquid Crystal based PDIs

The controllable variable phase offered by liquid crystals can also be utilized to provide a variable phase shift between the test and reference beams. The advantages over other phase modulators are the light transparency and the ease of creating the electrodes. Kadono (51) constructed a PDI from a NLC cell such that the NLC material is used to control the path length of one of the beams. A small circular region of electrode is removed from one surface of the NLC cell shown in figure 3.2 to create the pinhole. When an electric field is applied the molecules under this region do not rotate. Light polarized along the extra ordinary axis will experience different path lengths within the two regions. The pinhole region whose phase does not change generates the reference beam as per the PDI while the electric field is varied to control the phase shift applied to the test wavefronts passing through the surrounding region. The electric field is then varied to allow three interferograms to be obtained with phase shifts of $\frac{\pi}{2}$, π and $\frac{3\pi}{2}$ relative to the reference beam. This system retains the common path nature of the PDI, but does not generate the interferograms simultaneously as with the Mach Zehnder based setup outlined below. A significant drawback is that there is still some electric field present inside the pinhole associated with the electrode to pinhole boundary. The electric field becomes weaker further into the pinhole but the electric field does not follow a step function at this boundary. To overcome this such that there is a region with no electric field present (52), the area of electrode removed must be quite large, $\approx 20\,\mu$m .

An alternative method to overcome the problems due to the pinhole electric field boundaries is to remove the pinhole and remove a small amount of LC material for the LC layer. Such a device has been shown by (53) where small plastic microspheres of diameter $9\,\mu$m are scattered throughout the LC layer which is $9\,\mu$m thick

with continuous electrodes to overcome the edge effects, as shown in figure 3.5.

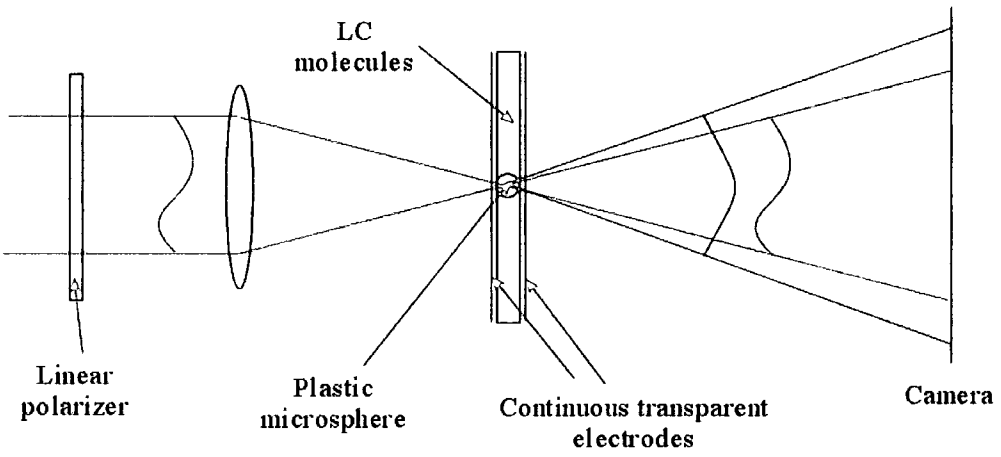

Figure 3.5: *The LC PDI with a plastic microsphere to create the reference beam. The voltage on the electrodes controls the phase shift relative to the reference beam*

The wavefronts under test are focussed on to one such microsphere which serves as the pinhole and generates the reference wavefronts. If the beam is polarized along the extra ordinary axis, n_e, then the phase shift of the test beam is controlled by the electric field in the same manner as the previous example. The extra ordinary refractive index can change by $\delta n = 0.24$ at 514nm. This permits a 2π phase shift with a comfortable margin in a $9\,\mu$m thick cell. A dye can be added to the LC molecules if any attenuation of the test wavefronts is required. The voltage across the LC cell is then varied to generate a series of interferograms at $\frac{\pi}{2}$ intervals. A significant drawback to these LC based PDIs is the necessity to operate with polarized light which is not ideal for astronomical AO uses. A solution to overcome this would be to place a quarter wave plate and mirror behind the LC. This rotates the polarization axes through 90^o allowing polarization insensitive operation.

3.4.3 Mach Zehnder derived WFS

A high order AO system based on the Mach Zehnder (MZ) interferometer has been demonstrated by Langlois (56). The system is specifically designed to remove only

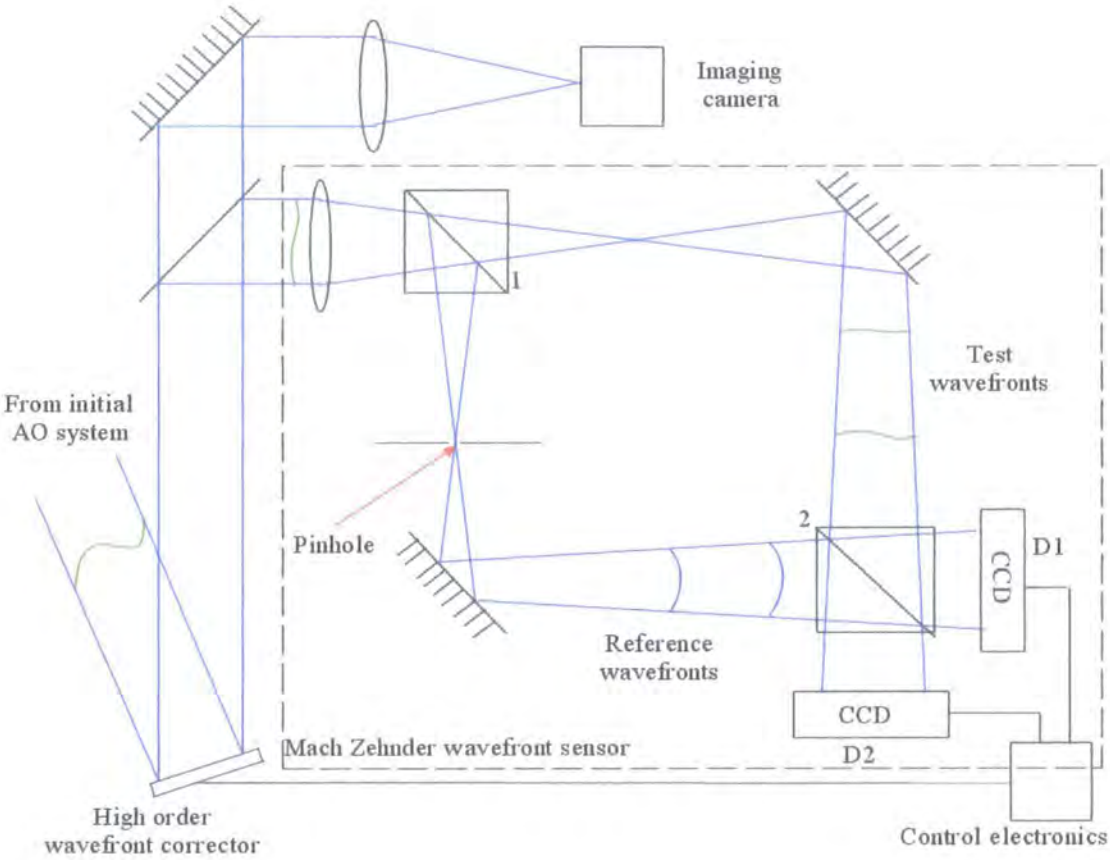

Figure 3.6: *The optical layout for the Mach Zehnder interferometer.*

high order low amplitude phase distortions after an initial AO system has already removed the larger low order distortions (55). The layout of the MZ interferometer is shown in figure 3.6.

On arrival at the interferometer the beam containing the distorted wavefronts is split by beamsplitter 1 to create two beams, each then travels along one arm of the interferometer. In one arm is a pinhole which spatially filters the beam to produce the reference beam. Unlike the PDI no test wavefronts then pass beyond the pinhole. In place of the test wavefronts passing around the pinhole they travel down the other arm of the MZ interferometer where beamsplitter 2 recombines the two beams. Interferograms are recorded at cameras D1 and D2. When the path length of the 2 arms is the same the extra reflections caused by the beamsplitters creates

a π phase difference between the optical path length of the two arms. Adjustment of the path length by $\frac{\lambda}{4}$ then means that the interferograms are phase shifted by $\frac{\lambda}{4}$ and $-\frac{\lambda}{4}$ respectively relative to the reference beam. When the incident wavefront is flat the output at D1 and D2 is equal. Any phase distortion then present causes a difference in D1 and D2 at the corresponding position. The phase is then retrieved by taking $D1 - D2$.

A closed-loop AO system is created by using a zonal piston only wavefront corrector such as an LC described previously. The control is implemented by simple digital differencing electronics without the use of a reconstructor. Since the setup generates the pair of interferograms simultaneously the subtraction can be performed without having to store initially an interferogram and wait for the next one to be generated. A CMOS sensor is considered preferable to a CCD for obtaining the data as the individual pixels can be directly read out whereas in a CCD there is a delay while the charge is transferred out. The drawback is that the CMOS sensor has higher readout noise and a lower quantum efficiency than a CCD.

3.4.4 Quadrature interferometric wave-front sensor

A coherent light based AO system has been demonstrated by Baker (57). The interferometer is based on a Twyman green quadrature interferometer. This can run in both open and closed loop. Open loop is where the feedback is omitted. The WFS is placed before the corrective element such that the actual distortion is measured. The merits of closed loop have already been discussed. Open loop has the facility for faster operation and the advantage that the WFS is not measuring the residual error left after correction. It is generally much more challenging to produce a stable open loop set up.

Figure 3.7 shows the optical layout for closed loop operation. A NLC SLM is used as the wavefront corrector, the WFS CCD camera images the interferograms and a computer is used to implement the control loop. Since this is a laboratory setup a Yd:NAG laser producing vertically polarized light is used. This is split by

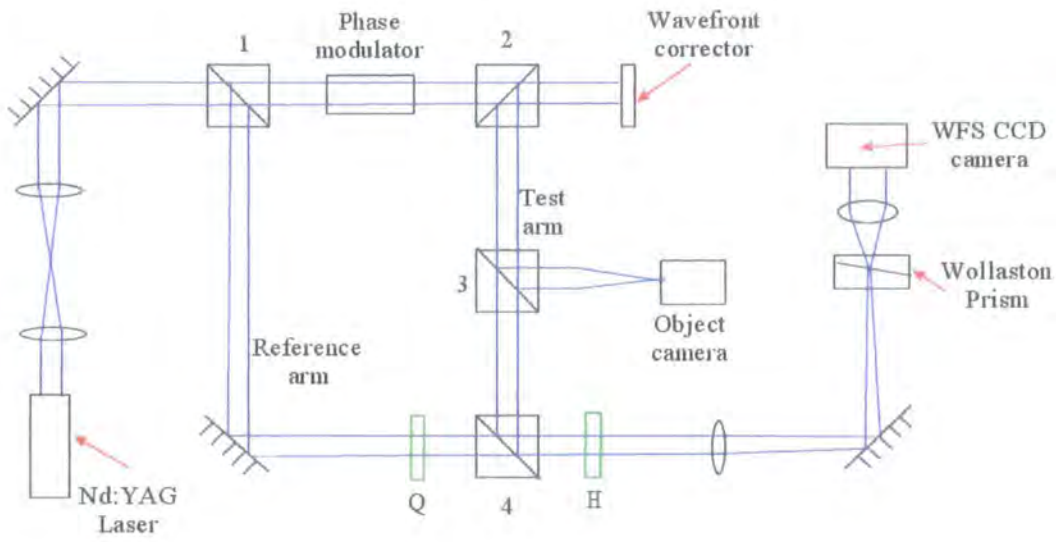

Figure 3.7: *The optical layout a closed loop AO system using a quadrature interferometric WFS. Q is a quarter wave plate, H is a half wave plate. Numbers 1-4 are beamsplitters.*

beamsplitter 1, and one beam becomes the reference beam while the other becomes the test beam. A phase modulator is used to generate the effect of turbulence and apply the distortions to the test beam which the system will then attempt to correct. The test beam is then reflected from the SLM where the correction is applied and recombined with the reference beam at beamsplitter 4. Beamsplitter 3 allows the image formed to be observed. Meanwhile the reference beam has passed through a quarter wave plate to produce circular polarized light. The reference and test arms are the same length such that the beams combine coherently and interference occurs. The combined beams then pass through a half wave plate to rotate the test beam polarization axis by 45^o to produce equal amplitude in both the horizontal and vertical directions. The $\frac{\pi}{2}$ phase difference in the reference beam is retained. The effect of this is to generate two phase shifted interferograms, with orthogonal polarizations. These are separated by a small angle (1.65^o) by the Wollaston Prism. The two interferograms are then imaged onto a CCD camera. The computer control then takes the output of this and applies the correction to the corrector. A prototype AO system has been run at $1.53\mu m$ using a 1024 element

MEMS as the corrector. The MEMS was used in this case as it allowed higher speed operation that the LC SLM. This setup in the described form is not suitable for use as an astronomical AO system since they started with an undistorted source to generate the reference beam. To modify the layout for conventional AO the laser would be replaced by the distorted wavefronts arriving from the object after having passed through the turbulent region. These must then be vertically polarized. The method employed by the Mach Zehnder described above could be used to generate the reference beam, i.e. use a pinhole in the reference arm to generate the reference beam. The corrector and camera imaging the object can be moved from within the interferometer so they are not limited to the polarized light operating within the interferometer.

In the next chapter an alternative interferometer derived from the PDI will be described. A LC waveplate will be used to create the pinhole retaining the common path nature of the PDI. Unlike the LC based interferometers outlined above, this interferometer will produce a pair of phase shifted interferograms simultaneously whilst operating with unpolarized light.

Chapter 4

Design and simulation of a novel liquid crystal point diffraction interferometer

4.1 The Interferometer

The interferometric wavefront sensor (WFS) constructed and evaluated in this thesis is a variation of the Smartt interferometer (20) or point diffraction interferomter (PDI) discussed in chapters 2 and 3. A phase PDI has a small phase discontinuity in a transparent window which serves to filter spatially the wavefronts in an incident beam focussed onto it. These spatially filtered wavefronts become the reference wavefronts which interfere with the initial distorted wavefronts which have passed around the pinhole. The resulting interferogram shows the phase distortions as amplitude modulations. To recover fully the phase information two or more interferograms are required each with a different phase shift relative to the reference beam.

The interferometer used is created from a ferroelectric liquid crystal (FLC) device with a small circle of $20\mu m$ diameter of electrode removed to form the phase discontinuity, which is referred to as a pinhole. A FLC is a birefringent material i.e. the refractive index is different in the orthogonal polarization directions n_o and n_e as with a NLC described in chapter 3. Unlike a NLC, a FLC is a waveplate with a fixed retardance but with electrically controllable optical axes. Application of an

electric field to the transparent electrodes causes the axes to rotate, except for the region under the pinhole, where they remain fixed. FLCs are usually bistable with the axes in one of two states separated by the switching angle. This angle is 45^o in this FLC. A square wave voltage is used to drive the FLC and causes it to switch between the two stable states.

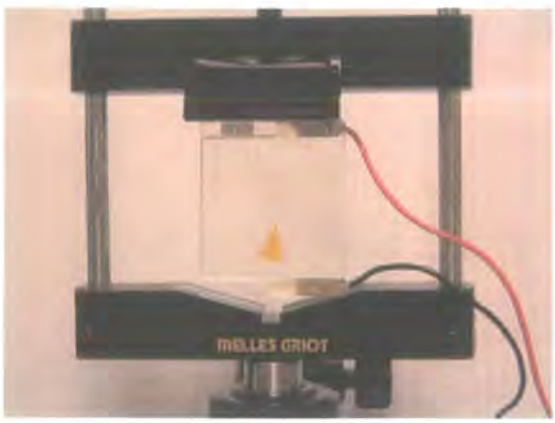

Figure 4.1: *A photograph of the FLC cell. The left hand image shows the overall cell, the two connecting wires are connected to the transparent electrodes and the yellow triangle marks the location of the pinhole. The right hand image shows the pinhole region under a polarizing microscope. The pinhole region dopes not appear uniformly dark as some of the LC molecules are trapped in the incorrect orientation.*

There are two main ways to produce phase only modulation with a FLC such that the pinhole region will generate a reference beam (58). The first is to place the FLC between crossed polarizers with the axes of the polarizers bisecting the two switchable positions of the FLC axes. When the axes are switched relative to the pinhole a phase shift of π will occur between the pinhole and its surrounding region. The advantage is that this occurs regardless of the switching angle or retardance of the waveplate. The disadvantage is the light throughput is not high and one can only create phase shifts of 0 or π.

The second method which is employed here is to create the FLC with a retardance of π i.e. it is a half wave plate (HWP) and place between two co-aligned quarter wave plates (QWP) (59). This setup is referred to as a "QHQ" and allows

two interferograms with separate phase shifts to be obtained as shown below:

For this analysis the QWP fast axes are considered to be horizontal, defined as 0^o with future angles measured relative to the horizontal. Light linearly polarized at 45^o is an eigenstate of the QHQ cell in the orientation used here. Jones Calculus (60) is used to calculate the effect of the QHQ on the incident beam. Let the Jones matrix of the QWP be given by J_{QWP}, the HWP as J_{HWP}, then the resulting beam, I_{out}, will be given by,

$$I_{out} = J_{QWP}J_{HWP}J_{QWP}I_{in},$$

where I_{in} is the incident beam. Since

$$J_{QWP} = \begin{bmatrix} 1 & 0 \\ 0 & e^{\frac{-i\pi}{2}} \end{bmatrix} \quad \text{and} \quad J_{HWP} = \begin{bmatrix} \cos 2\theta & \sin 2\theta \\ \sin 2\theta & -\cos 2\theta \end{bmatrix}$$

where θ represents the angle between the horizontal and the fast axis and

$$I_{in} = \begin{bmatrix} 1 \\ 1 \end{bmatrix} \frac{1}{\sqrt{2}},$$

where the $\frac{1}{\sqrt{2}}$ normalises the vector to have a magnitude of 1, then for the FLC axes in state 1, at an angle of θ to the horizontal,

$$\begin{aligned} I_{out} &= \begin{bmatrix} 1 & 0 \\ 0 & e^{\frac{-i\pi}{2}} \end{bmatrix} \times \begin{bmatrix} \cos 2\theta & \sin 2\theta \\ \sin 2\theta & -\cos 2\theta \end{bmatrix} \times \begin{bmatrix} 1 & 0 \\ 0 & e^{\frac{-i\pi}{2}} \end{bmatrix} \times \begin{bmatrix} 1 \\ 1 \end{bmatrix} \frac{1}{\sqrt{2}} \\ &= \frac{e^{-i2\theta}}{\sqrt{2}} \begin{bmatrix} 1 \\ 1 \end{bmatrix}. \end{aligned}$$

When the FLC switches the axes switch through 45^o and thus produces an angle of $\theta + 45^o$ relative to the horizontal, the resulting polarization for the same initial polarization I_{in} becomes

$$\frac{e^{-i2(\theta+\frac{\pi}{4})}}{\sqrt{2}} \begin{bmatrix} 1 \\ 1 \end{bmatrix}.$$

The axes within the pinhole remain fixed. If they are considered to be at an angle θ, then when the FLC switches to the $\theta + \frac{\pi}{4}$ state, the test and reference beam differ in phase by

$$-2i(\theta + \frac{\pi}{4}) - -2i\theta = -\frac{\pi}{2}, \tag{4.1}$$

as the argument of the complex notation holds the phase information. On passing through the QHQ cell the amplitude of the beam remains unchanged. The phase shift between the reference and test wavefronts is $-\frac{\pi}{2}$.

Although the FLC offers two different states, a reference beam will only be generated when the axes in the surrounding region are switched to 45^o relative to the pinhole axes. In the other state the pinhole is not detectable, so cannot be used for phase shifting interferometry. Due to the bistable nature a continuous phase shift between the test and reference beams cannot be generated by varying the electric field strength as with a NLC device. However, when the FLC is in the pinhole present state, a second phase is obtainable using the other orthogonal initial polarization state.

The orthogonal linear polarization state to the initial polarization, $I_{in,1}$, used above is also an eigenstate of the QHQ. The orthogonal polarization state is given by $A.B^* = 0$ with A and B as the polarization vectors with the $*$ meaning the complex conjugate of the second vector. The orthogonal polarization state, $I_{in,2}$ is

$$I_{in,2} = \frac{1}{\sqrt{2}} \begin{bmatrix} 1 \\ -1 \end{bmatrix} \quad \text{or} \quad \frac{1}{\sqrt{2}} \begin{bmatrix} 1 \\ e^{i\pi} \end{bmatrix}$$

which is linearly polarized at -45^o to the horizontal. With the FLC fast axis at an angle θ to the horizontal, then following a similar treatment, as with the $+45^o$ polarization, the resulting beam will be given by

$$I_{out,2} = J_{QWP} J_{HWP} J_{QWP} I_{in,2},$$

with $I_{out,2}$ the new output polarization. $I_{out,2}$ is given by,

$$I_{out,2} = \frac{e^{i2\theta}}{\sqrt{2}} \begin{bmatrix} 1 \\ -1 \end{bmatrix}.$$

When the FLC switched into the $\theta + \frac{\pi}{2}$ state, the resulting polarization is

$$\frac{e^{i2(\theta+\frac{\pi}{4})}}{\sqrt{2}} \begin{bmatrix} 1 \\ -1 \end{bmatrix}.$$

For the initial polarization $I_{in,2}$ the resulting phase shift between the test and reference beam is

$$2i(\theta + \frac{\pi}{4}) - 2i\theta = \frac{\pi}{2}. \tag{4.2}$$

Unpolarized light can be thought of as the superposition of two orthogonal incoherent linear polarization states. Considering the two orthogonal eigenstates at $\pm 45^o$ we see from equation (4.1) the $+45^o$ state is shifted by $-\frac{\pi}{2}$, and from equation (4.2) the -45^o state is shifted by $+\frac{\pi}{2}$ relative to the reference beams. A polarizing beam splitter as shown in figure 4.2 is used to separate out the two orthogonal states where the two interferograms are viewed on two separate outputs. The phase distortions on the beam are then measured by the difference in the corresponding pixel in both interferograms. This method gives us phase shifting interferometry with two interferograms with separate phase shifts. Although ideally we would like to have three, two is sufficient to obtain all the information needed for a working AO system. The FLC used in this way effectively is just an on/off switch for the PDI.

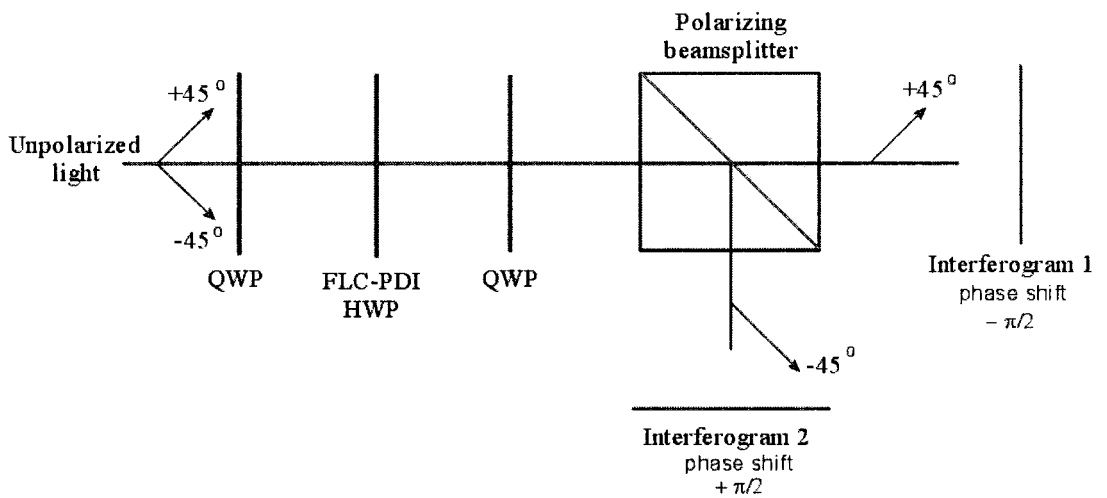

Figure 4.2: *Layout for the QHQ using unpolarized light. Unpolarized light is the superposition of two orthogonal linear polarization states which are separated by the beamsplitter cube. The linear states receive opposite phase shifts and are viewed on two separate outputs.*

It would be possible to create a PDI which functions in the same manner as this

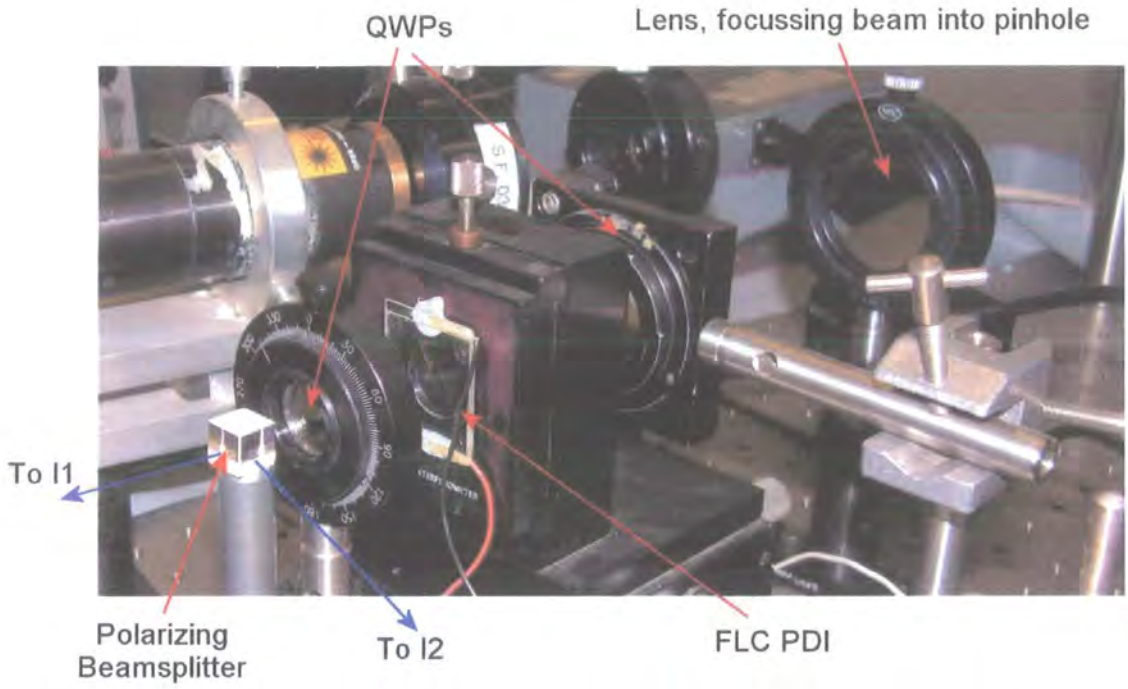

Figure 4.3: *Photograph of the operational QHQ interferometer. The lens focusses the initial beam containing the distortions into the pinhole of the FLC. I1 and I2 are the two phase shifted interferograms*

using just a HWP with a pinhole region where the optical axes have been rotated by 45^o. Using the FLC as the PDI, the PDI off state could be used to monitor any amplitude fluctuations on the initial beam and the FLC provides a simple way of creating the pinhole region.

This setup generates the pair of interferograms simultaneously which simplifies the control required for closed loop AO. A major benefit of this setup over the other LC based interferometers described in chapter 3 is that this uses unpolarized light so no photons have to be discarded by an initial polarizer. As with the alternate LC interferometers we have retained the common path nature of the original PDI design which is an advantage over the Mach Zehnder based setup where the two paths have to be carefully aligned and adjusted. A photograph of the actual optical components making up the QHQ cell is shown in figure 4.3.

4.2 Simulating the output of a PDI

The remainder of this chapter deals with simulating the response of a phase shifting PDI. The optical aberrations present on the initial wavefronts are modelled in terms of Zernike modes. The resulting wavefronts pass through a pupil, and are focused onto the PDI, which creates reference wavefronts while also allowing the initial wavefronts to pass through, and hence forming an interferogram. Fringe patterns generated using both the phase shifting PDI and a conventional PDI are simulated using the set up shown in figure 4.4 and compared so as to show the utility of the phase shifting method. This simulation is based on Fraunhofer Diffraction (see, e.g. Hecht (7) and Goodman (15)). All sources of noise have been ignored so as just to investigate the fundamental operation of the PDI.

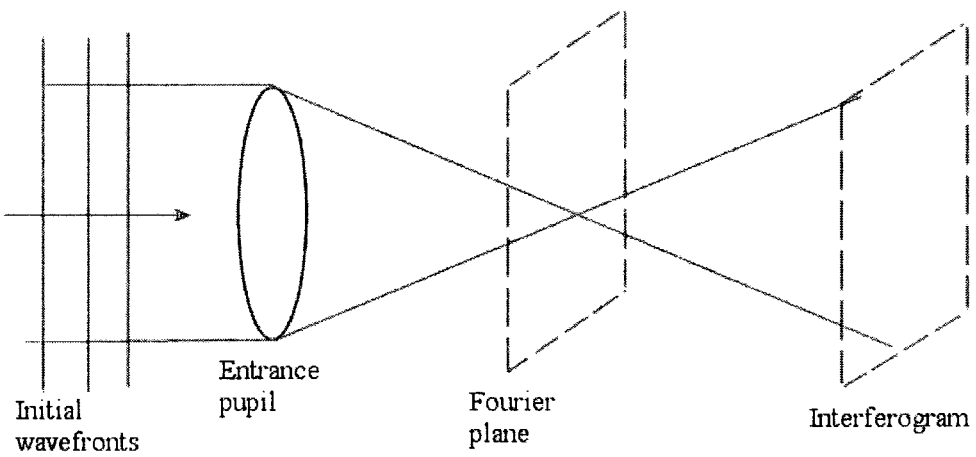

Figure 4.4: *Simulated optical setup. The PDI is placed in the Fourier plane and the resulting interference pattern is observed on the right hand side.*

4.2.1 Theoretical Background to the Simulation

Zernike Modes

Atmospheric turbulence can be modelled by Kolmogorov turbulence (61), which can be expanded using Zernike polynomials as described by Noll (62). This set of

polynomials was introduced by Zernike in 1934 and are a statistically independent set of polynomials describing the wavefront over a unit circle. Phase distortions are then a linear superposition of Zernike modes, although in the Kolmogorov model they are not necessarily orthogonal. They have a long tradition for describing aberrations in classical optics. Although they are well suited to modal adaptive optics systems where the mirror modes could be superpositions of Zernike modes, and the wavefront sensor measures the phase in terms of Zernike modes they are not so well suited to a piston only reconstructor free system. However we will use them here as they can be easily generated by a computer program. The general equations for a Zernike polynomial are given as defined by Mahajan (63) (64) and Roddier (65):

$$Z_{evenj} = \sqrt{n+1}R_n^m(r)\sqrt{2}\cos m\theta, m \neq 0,$$

$$Z_{oddj} = \sqrt{n+1}R_n^m(r)\sqrt{2}\sin m\theta, m \neq 0,$$

$$Z_j = \sqrt{n+1}R_n^0(r), m = 0,$$

where

$$R_n^m(r) = \Sigma_{s=0}^{(n-m)/2} \frac{(-1)^s(n-s)!}{s![(n+m)/2-s]![(n-m)/2-s]!} r^{n-2s}.$$

Z is the value of the phase distortion, and r, θ are the cylindrical polar co ordinates. n is the radial degree, which is the highest power of r, and m is the azimuthal frequency, which is the highest power of cos or sin θ. The value of R normalises the polynomials such that the root mean square value of the distortion over the circle is 1. In these simulations the value of R has been omitted. The first few Zernike modes are listed in table 4.1 (with $R = 1$).

n	m	Zernike Polynomial Z_j	Name
0	0	$Z_0 = 1$	Constant (Piston)
1	1	$Z_1 = 2r\cos\theta$	Tip
1	1	$Z_2 = 2r\sin\theta$	Tilt
2	0	$Z_3 = 2r^2 - 1$	Defocus
2	2	$Z_4 = r^2\cos 2\theta$	Astigmatism
2	2	$Z_5 = r^2\sin 2\theta$	Astigmatism
3	1	$Z_6 = (3r^3 - 2r)\cos\theta$	Pure Coma
3	1	$Z_7 = (3r^3 - 2r)\sin\theta$	Pure Coma
3	3	$Z_8 = r^3\cos 3\theta$	Trefoil (Zero Curvature Coma)
3	3	$Z_9 = r^3\sin 3\theta$	Trefoil (Zero Curvature Coma)
4	0	$Z_{10} = 6r^4 - 6r^2 + 1$	Pure Spherical
4	2	$Z_{11} = (4r^4 - 3r^2)\cos 2\theta$	5th Astigmatism
4	2	$Z_{12} = (4r^4 - 3r^2)\sin 2\theta$	5th Astigmatism
4	4	$Z_{13} = r^4\cos 4\theta$	
4	4	$Z_{14} = r^4\cos 4\theta$	

Table 4.1: *The first 15 Zernike Polynomials*

Other sources can use alternative numbering systems, sometimes calling the first mode (piston) Z_1 or by switching the cos and sin modes round. There is no set convention to their numbering and the modes used in this chapter are numbered as in table 4.1. Figure 4.5 shows the phase profile for mode Z_8 and figure 4.6 shows the phase profile for mode Z_{10}

Figure 4.5: *Phase profile of* Z_8

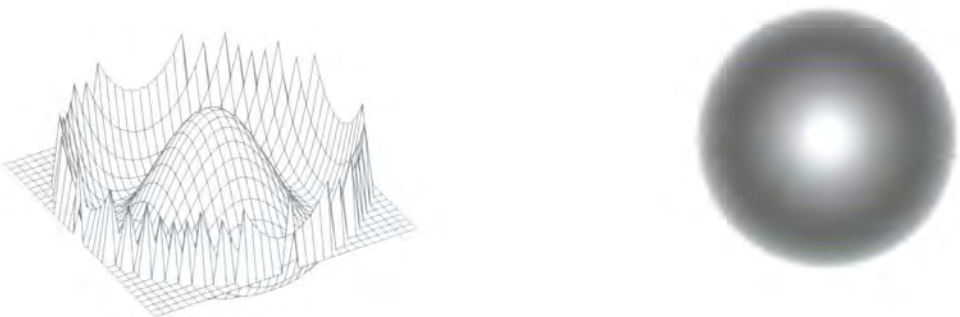

Figure 4.6: *Phase profile of* Z_{10}

Complex wave formation

An electromagnetic wave travelling in the **z** direction is represented by,

$$U = Ae^{i(kz-\omega t+\phi)},$$

where U is the wave vector, A is the amplitude of the wave, ω is the angular frequency, t is the time, k is the wave number and ϕ as the phase distortion. Since we are only interested in a snapshot of the propagating wave this equation can be reduced to,

$$U_{x,y} = A_{x,y}e^{i\phi_{x,y}}. \tag{4.3}$$

The values of A and ϕ are the amplitude and phase at a point x, y on the wavefront surface. The circular aperture defines the amplitude function A with,

$$A_{x,y} = \begin{cases} 1 & \text{Inside the Pupil} \\ 0 & \text{Outside the Pupil.} \end{cases}$$

The intensity of the wave at a point is given by the modulus, $|U|^2$, of the complex wave and the phase is given by the argument, arg(U).

Point Spread Function

The complex wavefunction in the Fourier plane is found by,

$$U_1 = F.T.(U),$$

with F.T. denoting the Fourier transform and U_1 is the wavefunction in the Fourier plane. Here we are ignoring a quadratic phase factor as it is not important here. The image which is observed in the Fourier plane is the intensity I of the wavefunction, given by,

$$I = |U_1|^2.$$

If the object is a point source then this is the point spread function (PSF). For flat wavefronts passing through a circular aperture then the pattern formed is the Airy disk. Adding a phase distortion to the wavefronts causes a degradation to the PSF. Figures 4.7 and 4.8 show the resulting PSF when the distortion is Zernike mode Z_{10} and Z_8 with the size of the distortion is 1λ respectively.

Figure 4.7: *PSF generated by* 1λ *of* Z_{10}

Figure 4.8: *PSF generated by* 1λ *of* Z_8

4.2.2 Mathematical model of a PDI

The PDI consists of a phase pinhole of phase shift $\frac{\pi}{2}$ relative to the surrounding area. The PDI function is then,

$$U_{pdi,A} = \begin{cases} e^{i\pi/2} & \text{Inside the pinhole} \\ 1 & \text{Outside the pinhole.} \end{cases}$$

The amplitude function is 1 throughout. The resulting wavefronts created by the PDI, U_A, are recovered by taking the Fourier transform of the resulting wavefunction in the Fourier plane,

$$U_A = F.T.(U_1 \times U_{pdi,A}),$$

and the interference pattern, I_A is obtained by $|U_A|^2$. The phase shifting PDI generates two interference patterns with a relative phase shift of $\pm\frac{\pi}{2}$ between the object and reference beam. The PDI simulation is run for a second time, but this time with the pinhole in the PDI has a phase shift of $-\frac{\pi}{2}$. The second PDI phase shift is defined,

$$U_{pdi,B} = \begin{cases} e^{-i\pi/2} & \text{Inside the pinhole} \\ 1 & \text{Outside the pinhole,} \end{cases}$$

the resulting wavefunction U_B is,

$$U_B = F.T.(U_1 \times U_{pdi,B}),$$

and the interference pattern, I_B is $|U_B|^2$.

The general equation for an interferogram is given by

$$I = I_0(1 + \gamma \cos\theta), \tag{4.4}$$

with θ as the phase difference between the 2 beams and

$$I_0 = I_{test} + I_{ref}.$$

I_{test} is the average intensity of the unfiltered distorted wavefronts and I_{ref} is the average intensity of the flat reference wavefronts produced by the pinhole. γ is the fringe visibilty and ϕ is the phase. In this case we have an unknown phase distortion given by ϕ and 2 interferograms with an additional phase shift of $\pm\frac{pi}{2}$ between the test beam and the reference beam. The 2 interferograms are given by

$$I_A = I_0\left(1 + \gamma \cos\left(\phi + \frac{\pi}{2}\right)\right),$$

for the $\frac{\pi}{2}$ phase shift and,

$$I_B = I_0\left(1 + \gamma \cos\left(\phi - \frac{\pi}{2}\right)\right),$$

for the $-\frac{\pi}{2}$ phase shift. Hence,

$$\begin{aligned} I_A &= I_0(1 + \gamma(\cos\phi\cos(\pi/2) - \sin\phi\sin(\pi/2))), \\ \text{and} & \\ I_B &= I_0(1 + \gamma(\cos\phi\cos(-\pi/2) - \sin\phi\sin(-\pi/2))), \\ \text{therefore} & \\ I_A &= I_0(1 - \gamma\sin\phi), \\ \text{and} & \\ I_B &= I_0(1 + \gamma\sin\phi). \end{aligned}$$

ϕ can be retrieved from the raw interferograms, I_A and I_B, via the following equation

$$\frac{I_B - I_A}{I_B + I_A} = \frac{I_0(1 - \sin\phi) - I_0(1 - \sin\phi)}{I_0(1 + \sin\phi + I_0(1 - \sin\phi)} \tag{4.5}$$

$$= \frac{2I_0\gamma\sin\phi}{2I_0} \tag{4.6}$$

$$= \gamma\sin\phi. \tag{4.7}$$

The fringe visibility γ is taken as being 1 in these simulations. Ideally a third phase shift would be used to create a third interfeorgram, then the three interferograms can be used to retrieve the phase regardless of γ. With just two phase shifts availible γ has to be determined experimentally by measuring known phase distortions first. For small phase variations $\sin\phi = \phi$ then

$$\phi_{detected} = \frac{I_A - I_B}{I_A + I_B}. \tag{4.8}$$

The detected phase $\phi_{detected}$ at a point (x,y) is then the difference between the two interference patterns at that point (x,y), normalised by the sum at that point.

4.2.3 Results

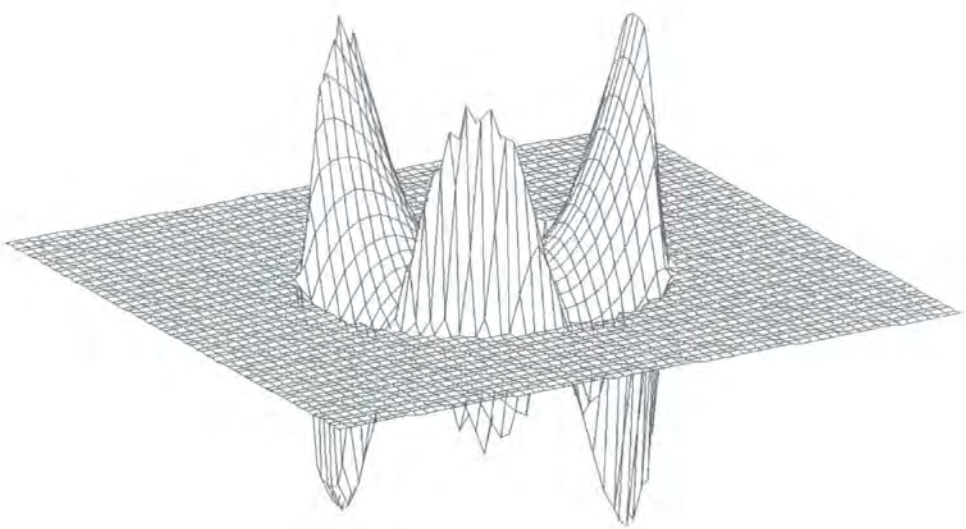

Figure 4.9: *Surface plot of the detected phase* $\frac{A-B}{A+B}$ *from* Z_8 *through the phase shifting PDI. Its shape matches that of the input. The flat surround is due to the aperture function*

Zernike modes were then applied to the phase shifting PDI and the resulting interference patterns investigated. Figure 4.9 shows the detected wavefront ($\phi_{detected}$ as defined by equation 4.8) surface for input wavefronts with Zernike mode Z_8 as the initial phase distortion. This can be compared to the initial phase shown in figure 4.5. These show the detected wavefront shape matches the initial wavefront

shape. This shows the phase shifting PDI is detecting the phase. Figure 4.10 shows

Figure 4.10: *The left hand image shows the initial phase and the right hand image is the detected phase. The scale is the phase distortion in radians*

the initial phase and the detected phase for Z_8. To see more clearly what is happening, figure 4.11 shows a slice through Z_8 (radially along $\theta = 0$) showing the initial and detected phase. The aperture function is defined such that $A = 1$ for $|r| < 1$ and $A = 0$ elsewhere.

The performance of the phase shifting PDI is evaluated by looking at the residual error, i.e. the difference between the initial phase and the detected phase, $\phi_{detected}$

$$\phi_{err} = \phi_{initial} - \phi_{detected}$$

with $\phi_{initial}$ as the initial phase distortion and ϕ_{err} as the residual phase error. The root mean square (RMS) is then calculated for ϕ_{err}, and is plotted as a function of the Zernike mode and the size of the phase distortion in figure 4.12.

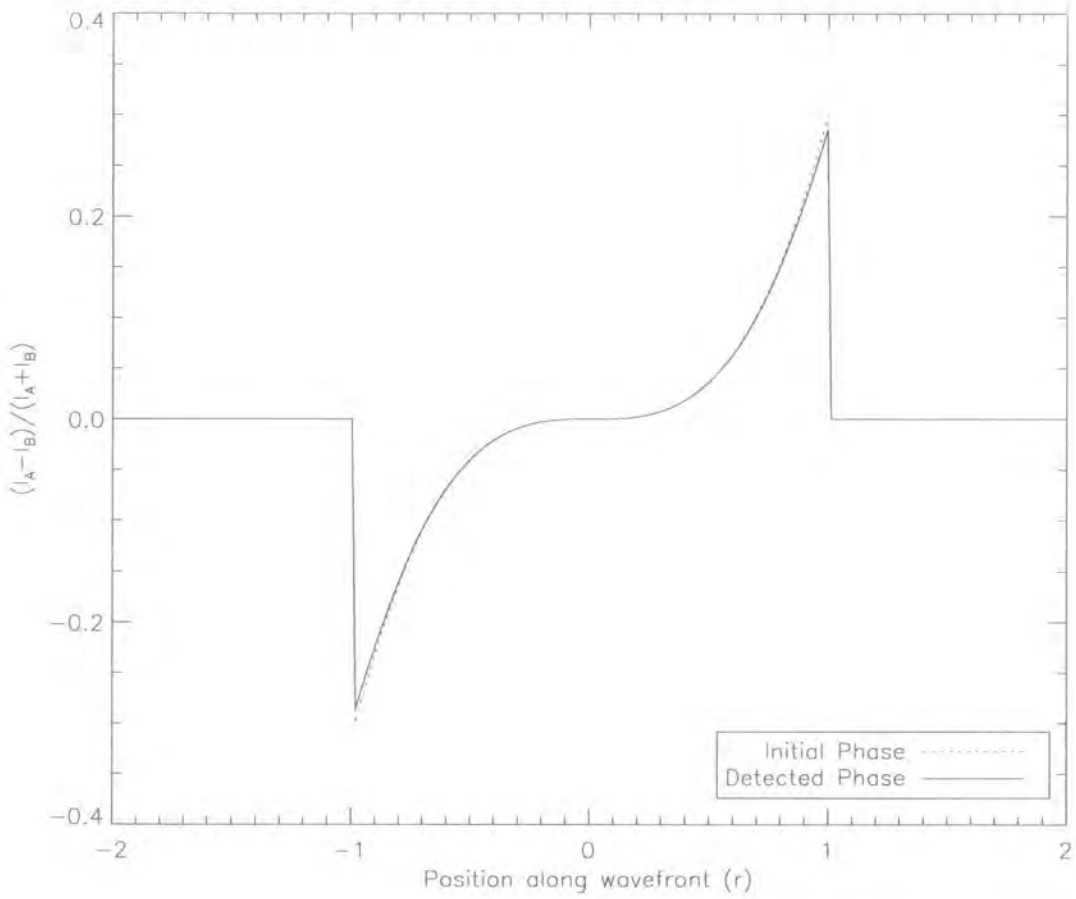

Figure 4.11: *A 2D view along the x axis of figure 4.10 showing very little error (in this noiseless simulation) between the initial and detected phases. In order to obtain the actual value of the phase distortion present, the visibility γ is required.*

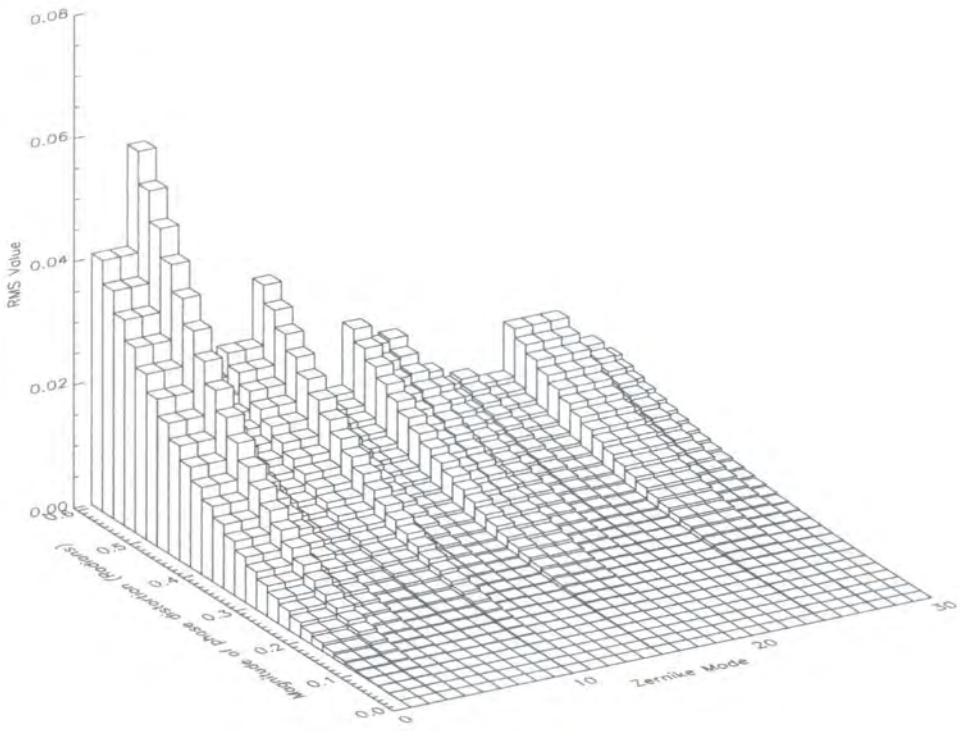

(a)

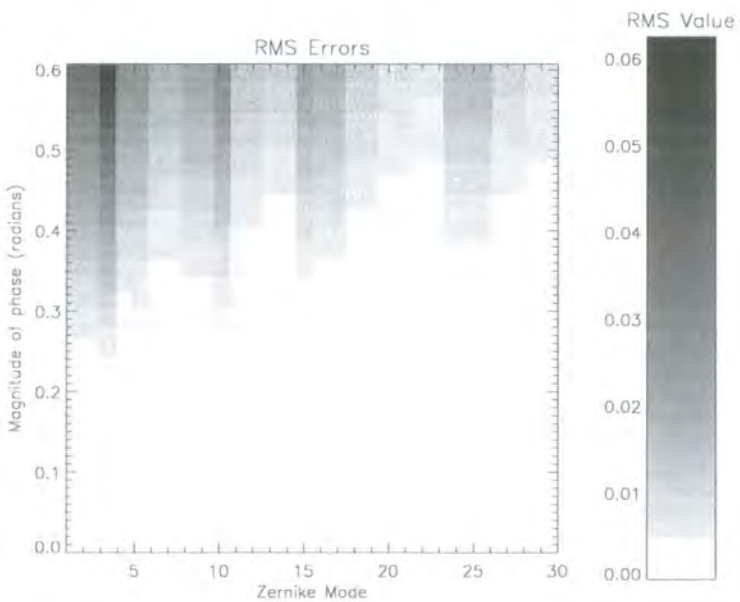

(b)

Figure 4.12: *The residual RMS errors with the detected phase using the phase shifting PDI, shown as a (a) surface plot and (b) intensity plot*

4.2.4 Effect of pinhole size

The simulation performed above has used the smallest possible pinhole in the PS-PDI. Figure 4.13 shows the output when a larger pinhole is used. make do with C++!) As the pinhole size is increased the accuracy of the detected phase is reduced.

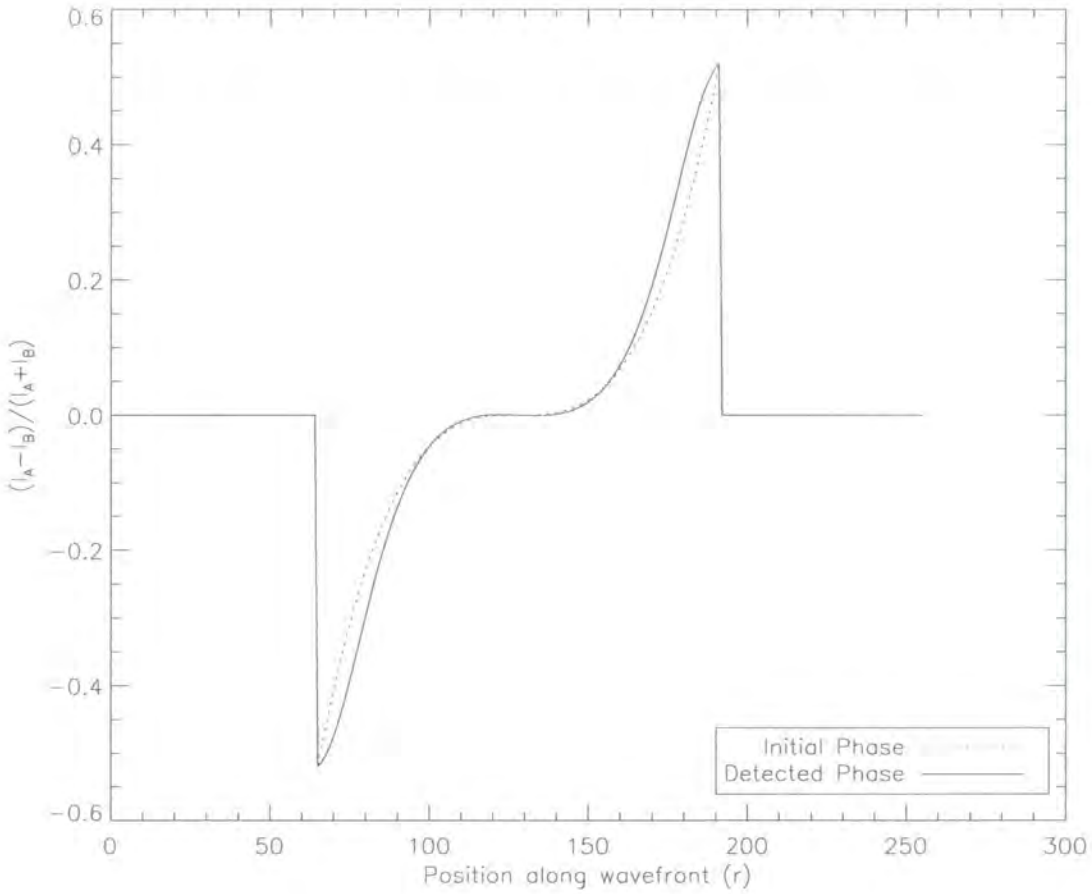

Figure 4.13: *A slice through the output for a larger pinhole than that used to create figure 4.11. This shows that although the contrast is improved for this larger pinhole the accuracy of the detected phase is lower.*

The contrast is observed to go through a maximum, the maximum contrast occurs when the relative intensities of the 2 beams are equal. For the purposes of the results shown in figure 4.12 the smallest pinhole is used as the aim of the simulation is to demonstrate the phase detecting capability of the LC-PDI.

4.2.5 Advantages of a phase shifting PDI over the standard PDI

A simpler method of using the PDI is to have only one phase shift and to use a single interference pattern produced to obtain the initial phase distortion. The detected phase becomes simply A ($A = |U_A|^2$) using the small angle approximation again. Figure 4.14 shows a slice through the x axis for mode Z_8 through the output from

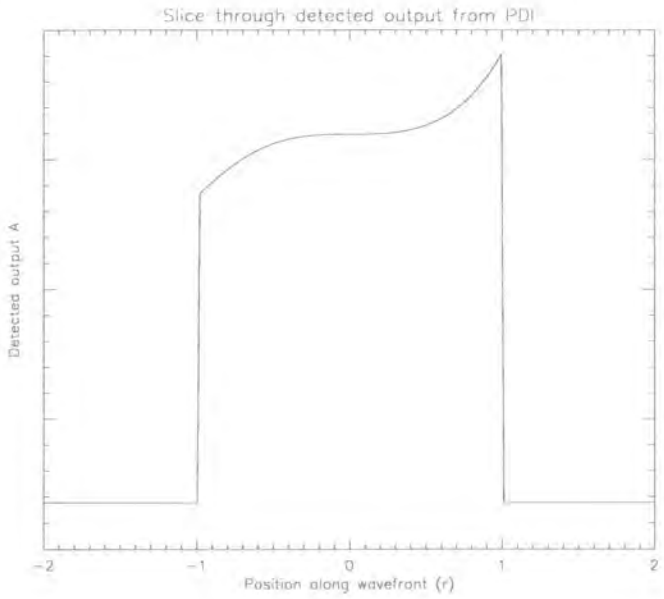

Figure 4.14: *A slice through the interference pattern $|U_A|^2$ from the simple PDI. The aperture function is defined $A = 1$ for $|r| < 1$. The phase distortion is detected along with a background intensity. There is alos some illumination present beyond the boundary of the original pupil function i.e. at $|r| > 1$. This is because the smallest pinhole is used for this simulation. The small pinhole causes the reference beam to emerge at a much wider angle from the PDI and hence illuminates the region outside the original pupil. There is no phase information out here as the test beam does not illuminate this region.*

the simple PDI with the smallest possible pinhole. The initial phase is visualised in the interferogram, but the initial intensity is also present, so the phase cannot be obtained without some knowledge of this, whereas with the phase shifting PDI the initial intensities cancel in subtracting the two interferograms. Secondly if we

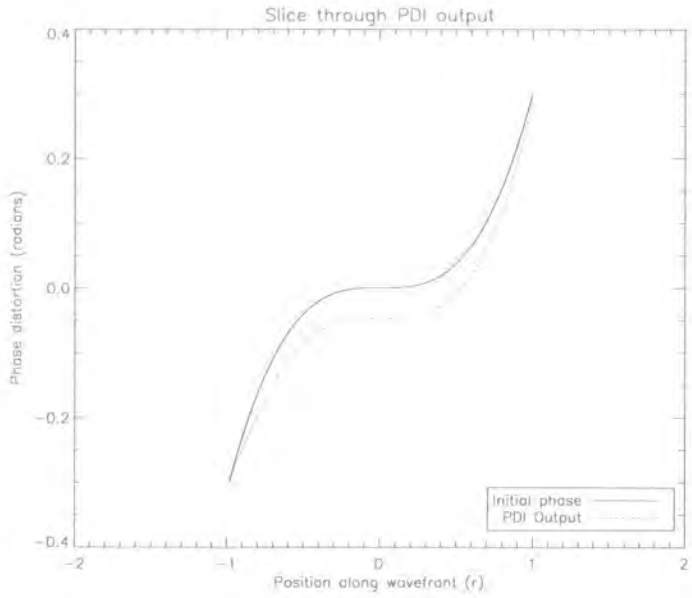

Figure 4.15: *The detected phase from figure 4.14 has been scaled to match the magnitude of the initial phase distortion and the region around the aperture has been removed. The detected shape does not match the initial phase as it did with the phase shifting PDI. The initial phase distortion is the same as in figure 4.11.*

are just concerned with the detected phase, i.e. the region $|r| < 1$ and scale this to match the initial phase, figure 4.15 shows the detected phase is not as accurate as that when using the phase shifting PDI (shown in figure 4.11).

4.3 Theoretical Correction with Amplitude Fluctuations

4.3.1 Effect of amplitude fluctuations

So far only the operation of the phase shifting PDI with no amplitude fluctuations across the beam has been considered. In this section the effect of amplitude fluctuations present on the initial beam cross section along with phase distortions are simulated to verify if the PDI can operate as a WFS when there are amplitude fluctuations present on the initial wavefronts. Amplitude fluctuations are added by changing A in equation 4.3 such that $A \neq 1$ inside the pupil. Figure 4.16 shows

Figure 4.16: *Right hand image is the phase detected for Z_8 (The left image shows the initial phase) when the pupil has amplitude distortions. Some of the original amplitude distortions are present in the detected phase.*

the detected phase, $\phi_{detected}$ for Z_8, with the same size as in figure 4.10 when an amplitude fluctuation is added such that A varies randomly between $\frac{1}{2}$ and 1 inside the pupil and $A = 0$ outside the pupil. The amplitude fluctuations appear in the detected phase, reducing the quality of the image.

4.3.2 Correcting with Amplitude Fluctuations Present

A proposed method to reduce the effect of these amplitude fluctuations and increase the accuracy of the measured phase distortions is to use the FLC off state. When the FLC is in the off state there is no pinhole present so no reference beam is created. This allows the initial beam U to pass through unaltered. Given that the initial beam is unpolarized then the outputs at I_A and I_B will measure $|U|^2$ and contain the amplitude fluctuations and not the phase distortion. The model to remove these is to subtract the amplitude fluctuations measured with the FLC off from the interferograms I_A and I_B obtained when the FLC is on.

$$I'_x = I_x - |U|^2$$

where x represents output A or B and I' the resultant intensity. Then the phase is retrieved by

$$\phi_{detected} = \frac{I'_A - I'_B}{I'_A + I'_B} \tag{4.9}$$

$$= \frac{(I_A - |U|^2) - (I_B - |U|^2)}{(I_A - |U|^2) + (I_B - |U|^2)} \tag{4.10}$$

$$= \frac{I_A - I_B}{I_A + I_B - 2|U|^2} \tag{4.11}$$

I_A and I_B are the measured intensities at the outputs with the FLC on.

4.3.3 Results

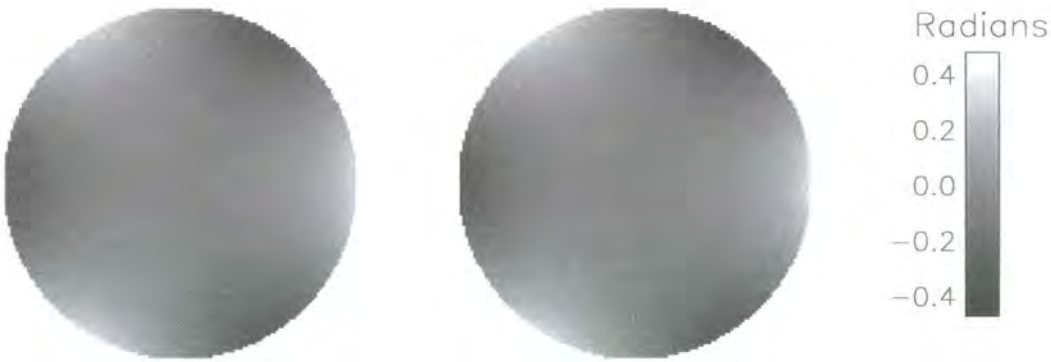

Figure 4.17: *The right hand image is the phase detected when the amplitude modulations measured with the FLC off are removed. The amplitude modulations have been very much reduced in the detected phase. The RMS errors for these results are shown in table 4.2.*

Figure 4.17 shows the initial phase and detected phase for Z_8 with the same amplitude fluctuations present, with the images formed with the FLC off subtracted as given by equation 4.11. Figure 4.18 shows the difference between the detected phase and the initial phase when amplitude fluctuations are present on the initial wavefronts and for when the FLC off state is subtracted. Table 4.2 shows the RMS residual errors for the results in figures 4.16 and 4.17. By using the FLC off

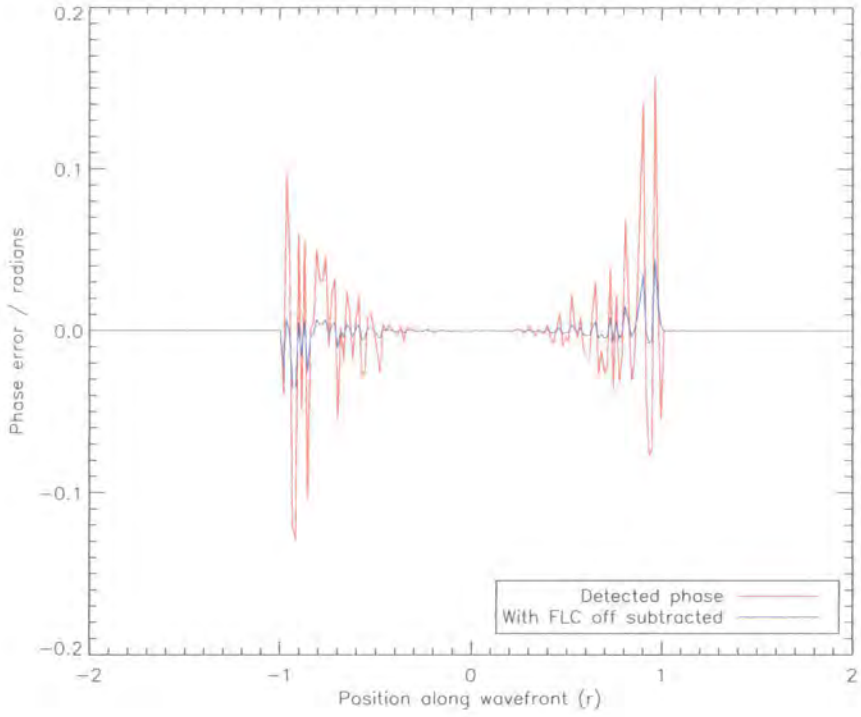

Figure 4.18: *Shows a slice through the wavefront for the difference between the initial phase and the phase detected by the PDI when amplitude fluctuations are present on the initial wavefronts. The "detected" line shows how any amplitude fluctuations cause an error in the measured phase and how these are much reduced by utilizing the FLC off states.*

Amplitude function	RMS Error
$A = 1$ inside aperture	0.0014
A varies $0.5 \rightarrow 1$ inside aperture	0.0141
A varies $0.5 \rightarrow 1$, FLC off state subtracted	0.0032

Table 4.2: *RMS residual phase errors for Zernike mode Z_8 from $-\frac{\pi}{10}$ to $\frac{\pi}{10}$ in the initial wavefronts.*

state to remove these from the detected phase, the distortions in the detected phase caused by the initial amplitude fluctuations have been very much reduced, with the RMS error is improved by more than a factor of 4. Table 4.3 shows the RMS errors when the initial amplitude fluctuations are smaller, now varying between 0.75 and

1. Again the RMS is improved by using the FLC off state, this time almost to the accuracy of the phase when there are no distortions present.

Amplitude function	RMS Error
$A = 1$ inside aperture	0.0014
A varies $0.75 \rightarrow 1$ inside aperture	0.0055
A varies $0.75 \rightarrow 1$, FLC off state subtracted	0.0015

Table 4.3: *RMS residual phase errors for Zernike mode* Z_8 *from* $-\frac{\pi}{10}$ *to* $\frac{\pi}{10}$ *in the initial wavefronts*

4.4 Conclusion

The results show that the phase shifting PDI accurately measures the phase distortion on the initial wavefronts, for small phase variations. The simple PDI is not so accurate, as it cannot determine the phase directly, and the phase that it does measure is not so accurate. The FLC phase shifting PDI offers a second advantage in that the FLC can be switched off allowing any amplitude variation to be removed from the detected phase.

Chapter 5

Static wavefront sensing and correction

5.1 Introduction

In this chapter the operation of the "QHQ" based point diffraction interferometer (PDI) described in the previous chapter is investigated to measure non time varying phase distortions. Since the operational wavelength of the components making the QHQ-PDI is 543nm, a Green HeNe laser (GreNe) of wavelength 543nm is used. This supplies a collimated laser beam onto which the phase distortions are added by a liquid crystal (LC) spatial light modulator (SLM).

In the first instance the capability of the QHQ-PDI to measure phase is tested. Known phase distortions generated using the LC-SLM are measured with the QHQ-PDI. This verifies that the phase can be recovered.

In the second instance the utility of the QHQ-PDI as a wavefront sensor (WFS) is investigated. Static phase distortions are again generated by the LC-SLM which are measured by the QHQ-PDI. The output is then used to calculate the correction which should be sent to the LC-SLM to null the initial distortion. This correction is then applied to the LC-SLM and the laser beam is focussed before and after correction and the image quality is measured.

5.2 The Hex 127 Spatial Light Modulator

5.2.1 Overview

The phase distortions are added by using a Meadowlark Optics Hex 127 LC spatial light modulator (SLM) (67). This is a reflective device used in place of a deformable mirror. It is a Nematic LC device consisting of 127 individually addressable hexagonal LC pixels each with piston-only phase modulation. This is a zonal SLM such that each pixel only affects the phase on its own surface. Figure 5.1 shows the layout

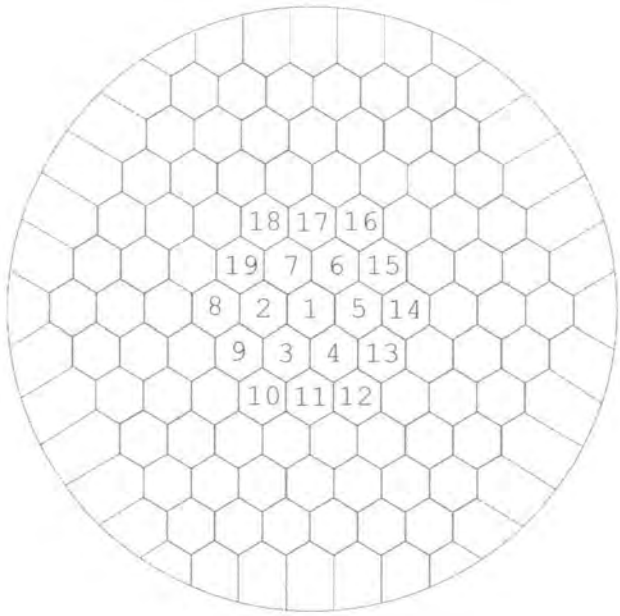

Figure 5.1: *Layout of the surface of the Hex 127 SLM. The innermost pixels have been numbered, the numbering is in concentric rings from the centre outwards*

of the hexagonal pixels on the LC-SLM. Phase patterns have to be approximated as a step wise piston only shape. The phase surface is not continuous as a phase discontinuity exists between each pixel. A slight drawback of a non continuous phase surface is diffraction from the pixel boundaries. Very fine wires run along the pixel boundaries to supply an independent electrical connection to every pixel. An amplifier which in turn is connected to a personal computer (PC) is used to

supply the drive voltages for the Hex 127 pixels. The software allows the voltages for individual pixels to be entered and it can also store patterns to send to the amplifier in succession. The amplifier can supply a voltage of 0 to 40V as a low frequency (137Hz) AC square wave to each pixel with a 12 bit resolution. The Hex 127 is a dual frequency device as outlined in chapter 3 section 3.2 where a short high frequency pulse can be sent to force the LC molecules to relax. This process helps to overcome one of the major drawbacks of LC-SLMs in that the time required for the molecules to relax is rather slow. The amplifier supplies the required high frequency AC pulse ($\leq 10ms$) of 35kHz for this.

5.2.2 Polarization insensitive operation

A single LC cell will only apply a phase shift to light polarized along one linear direction, the extra ordinary axis. The Hex 127 overcomes this limitation by passing the light through the LC twice using a mirror and a quarter wave plate (QWP) to rotate the polarization axis between each pass (44). Figure 5.2 shows the optical

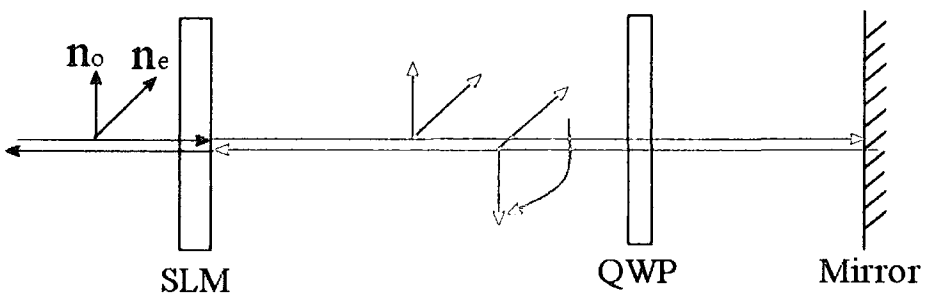

Figure 5.2: *Polarization insensitive operation using a NLC. The QWP and mirror rotate the polarization axis by* 90^o *enabling the phase shift to be applied to both axes of polarization*

layout of each pixel. The QWP axes are at 45^o to the axes of the NLC. For the purpose of imaging it does not matter that the plane of polarization has been rotated by the layout. The important result is the phase shift ϕ has been applied to both polarization directions. It should also be noted that an additional phase shift of $\frac{\pi}{2}$ has been picked up regardless of the applied phase shift ϕ. Since this is true for every Hex 127 pixel this is applied to the entire wavefront, along with an overall

phase shift due to the thickness of the optical components. Although operating in this manner is dependent on the wavelength due to the QWP, Kelly and Love (66) have shown that satisfactory performance is obtained with white light.

5.2.3 Phase to voltage relationship

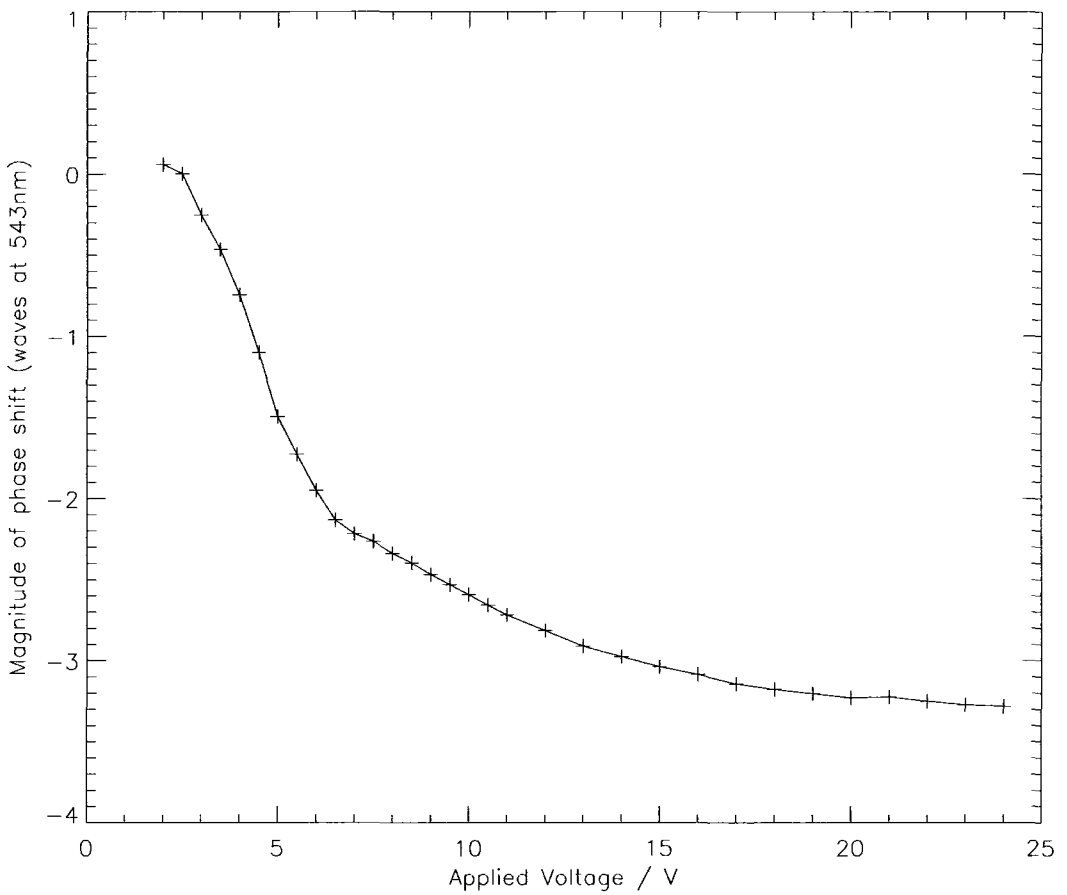

Figure 5.3: *Graph showing the phase shift at 543nm induced by the voltage applied to a pixel in the Hex 127. The line is a guide to the eye.*

In order to generate known phase distortions with the Hex 127, the relationship between the voltage applied to a Hex 127 pixel and the actual phase change obtained is required. A Zygo phase shifting interferometer (68) is used to measure the phase shifts obtained. The Zygo interferometer uses a stitching method to overcome the 2π ambiguity usually associated with interferometry.Voltages are sent to the pixels on the Hex 127 and the output phase given by the Zygo interferometer are recorded.

These are shown in figure 5.3. The Zygo's internal stitching method was unable to determine this plot entirely on its own when a large phase step is present between 2 neighbouring pixels. This was overcome by investigating the results from the Zygo and manually stitching together the plot in figure 5.3. This plot is used in the succeeding sections to convert a voltage on the Hex 127 into an actual phase shift. The response for each pixel is the same to within 0.04λ.

5.3 Experimental setup

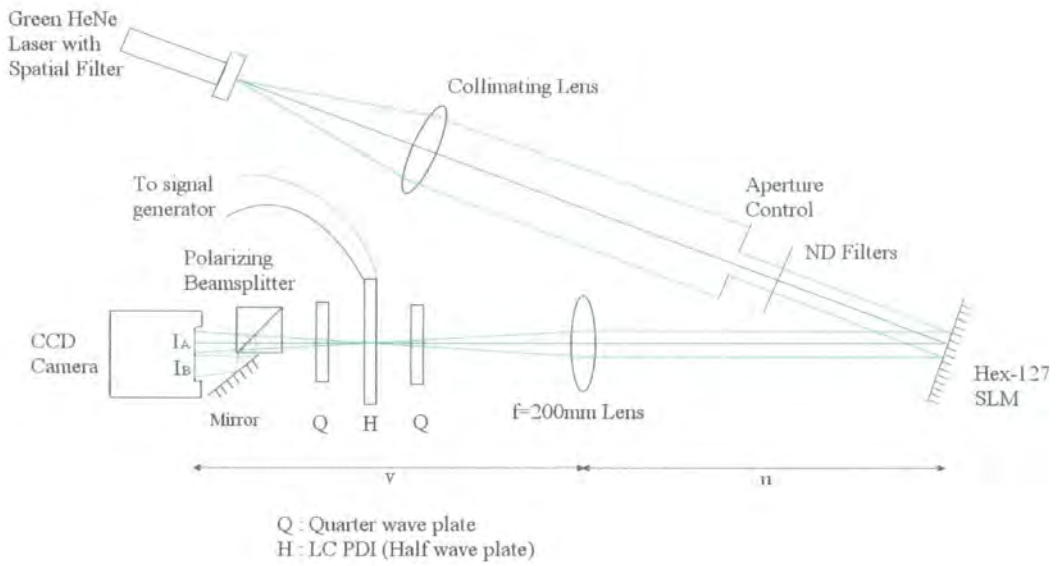

Figure 5.4: *Optical layout for operating the phase shifting PDI to detect the applied phase distortions.*

Figure 5.4 shows the optical setup used to measure the QHQ based PDIs response to phase distortions. A lens of focal length 200mm is used to focus the collimated laser beam containing the phase distortions into the pinhole. The pinhole is slowly moved such that the focal point of the beam is in the pinhole. Another advantage of using the FLC is that it switches the pinhole on and off and thereby causes the interferogram to flash. This makes locating the correct position much simpler. The QWP axes are set at 45^o to the horizontal such that the two orthogonal polarization

states separated by the polarzing beamsplitter are horizontal and vertical. Phase shifted interferograms, I_A and I_B are recorded with a CCD camera. For simplicity the beam containing I_B is folded back such that both interferogram are imaged on one camera. The interferograms need to be at an image plane of the Hex 127 so the pixel boundaries appear in focus. The lengths u and v are set to satisfy this criteria and to maximize the area of the CCD illuminated by the interferograms. The folding mirror is placed close to the polarizing beamsplitter so as to keep the path length difference PDI to I_A and PDI to I_B as small as possible, in this case the difference in length was 5 mm. Neutral density (ND) filters are placed in the laser path and values are chosen such that the camera's dynamic range is used to good effect without saturating it. The CCD camera is connected to a frame grabber and a computer where the interferograms are recorded.

Figure 5.5 shows an example of the interferograms recorded. The individual hexagonal pixels of the Hex 127 can easily be observed by the dark boundaries between them. The phase difference of the centre pixel can be observed by the different shade of the pixel to the surrounding ones.

5.3.1 Geometry matching

In a reconstructor free AO system using an interferometer and a piston only corrector each pixel on the camera corresponds to each pixel on the corrector. In this case the CCD camera has many more pixels than on the Hex 127 therefore each Hex 127 pixel covers many pixels on the camera. All these camera pixels covered by a Hex 127 pixel are re-binned to return one value representing the output at that location. Figure 5.6 shows the area considered as each pixel on the camera. As shown in chapter 4 the phase is then recovered for a given pixel by taking

$$\phi = \frac{I_A - I_B}{I_A + I_B} \tag{5.1}$$

where ϕ is the phase, I_A and I_B are the recorded intensities at the corresponding pixels on the two interferograms.

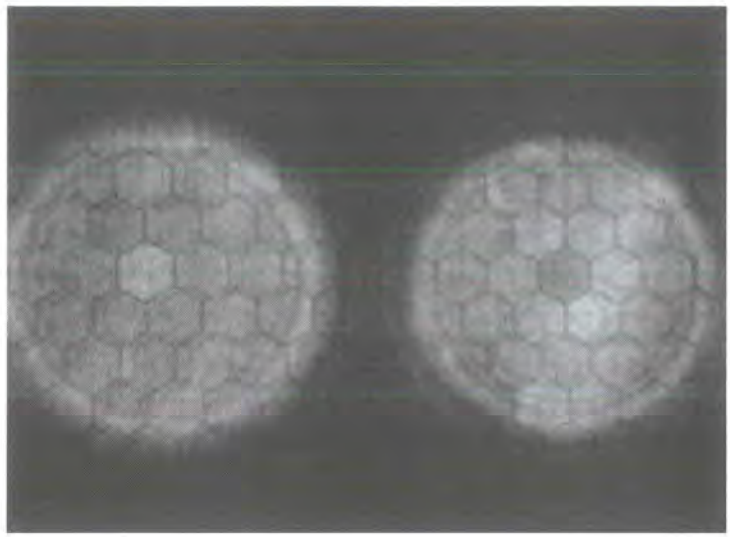

Figure 5.5: *Image obtained from the CCD camera with a voltage of 8V (≅ 2.4 waves) applied to the centre pixel and 14V (≅ 3 waves) applied to the rest. The 2 visible circular images are the 2 interferograms. The hexagonal structure is the pixel boundaries from the Hex 127. The fainter shadow Hex structure visible is caused as the laser beam is not incident normally onto the Hex 127 surface. Only the central portion of the Hex 127 is used here.*

5.4 Detecting phase with the PDI

Voltages are sent in turn to the centremost pixel on the Hex 127 (Number 1 in figure 5.1) while all of the remaining pixels are held at a constant voltage for which 14V was used. 14V is selected for these as it is away from the region where small changes in voltage result in large changes in phase on the Hex 127. In the next section a 1 wave region is selected for operation and 14 V lies within the selected region. The centre pixel is varied between 3V and 24V as this covers the range where the phase is observed to change in figure 5.3. The phase is retrieved using equation 5.1 for the centre pixel.

Figure 5.7 shows the PDI output obtained. The theory would suggest a more sinusoidal output than this. Phase shifting interferometery can normally only measure the phase changes uniquely over one wave (2π rad) and this is confirmed to be the case here by these results. Since the aim is to show the PDI can function as a wavefront sensor on an AO system where the phase distortions present are within a

Figure 5.6: *The CCD pixels are re binned to correspond to the detector pixels. The hexagonal pixels of the Hex 127 can be seen, with the black circles representing the binned detector pixels*

one wave (2π rad) range then a region covering 1λ can be selected as the operating region. The region 2.3λ to $3.3\lambda$is chosen as the QHQ-PDI has a linear response within that region. This corresponds to a voltage region of 7.5V to 24V. Figure 5.8 shows in more detail the response for the region 2.3λ to 3.3λ. Providing the phase distortion is within this operating region then the QHQ-PDI can measure the distortion present. The plot shows that when there is no phase distortion present on the Hex 127 when all pixels are at 14 V there is an offset signal present. This was verified by measuring $\frac{I_A - I_B}{I_A + I_B}$ with no voltages applied to the Hex 127. The output in this case was found to be -0.146 in agreement with the offset present on figure 5.8.

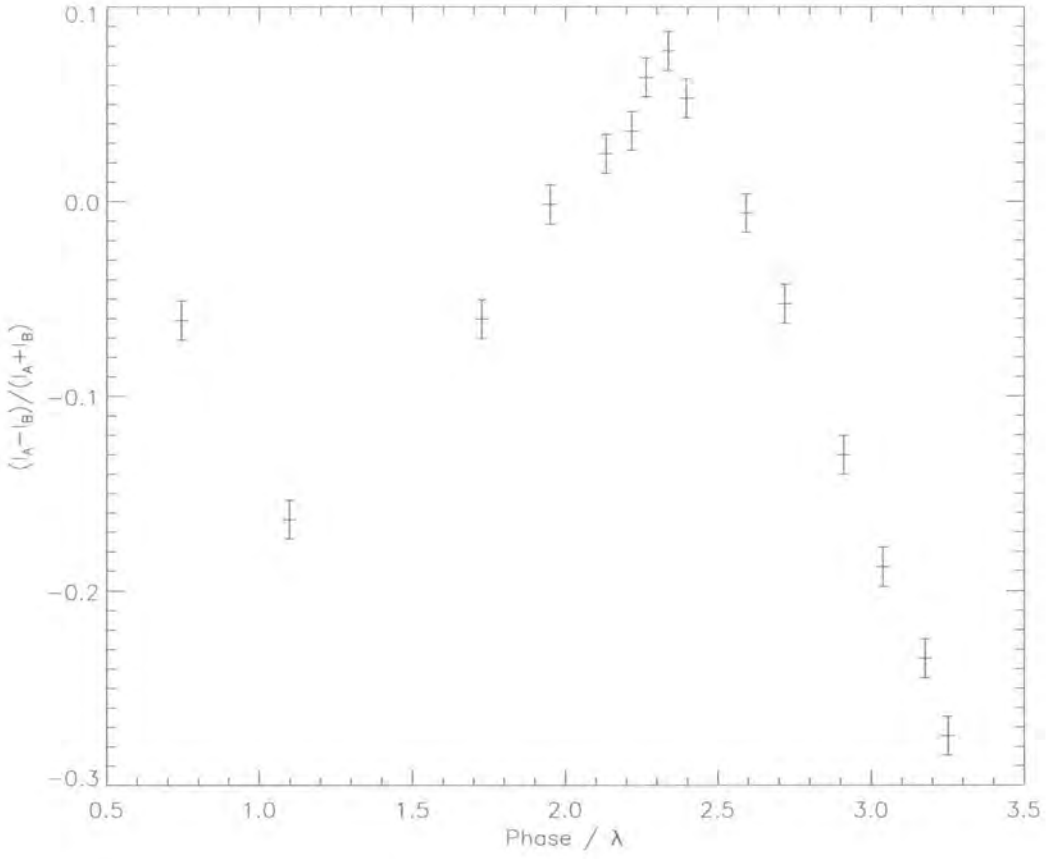

Figure 5.7: *Results for varying the phase on the centre pixel. The voltage value applied to the Hex 127 has been converted to phase using the results in figure 5.3. The surrounding pixels were maintained at 16V (= 3λ). The aim is to show the phase can be detected over a 1λ range. The region 2.3λ to 3.3λis selected where this is true.*

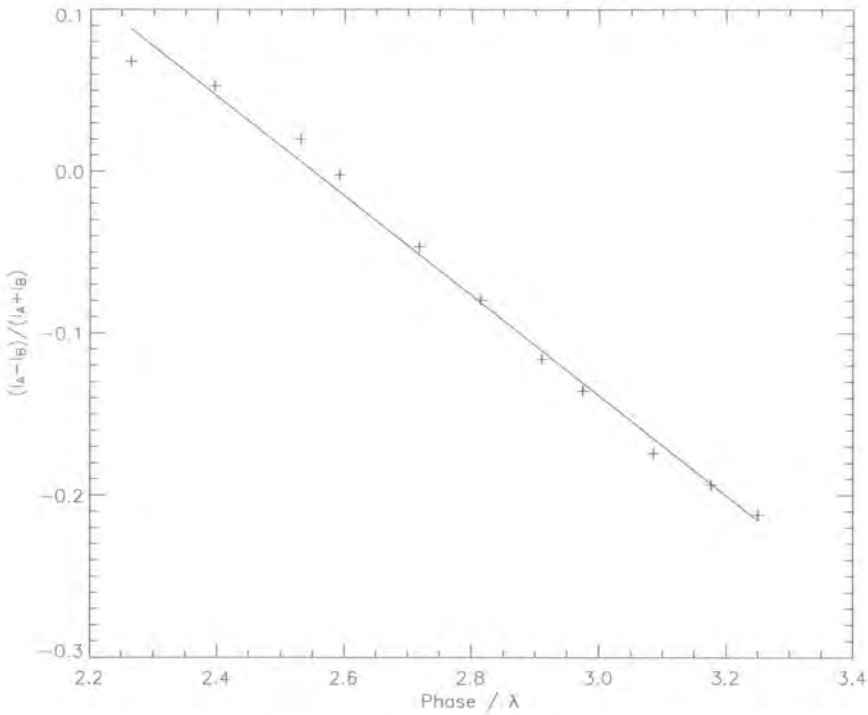

Figure 5.8: *The response of the QHQ-PDI to phase distortions over a 1λ range. A linear fit is applied to the data points. The fit parameters can then be used to convert the value* $\frac{I_A - I_B}{I_A + I_B}$ *measured by the QHQ-PDI into the actual phase distortion present.*

The actual value of the phase distortion present cannot be determined exactly by the QHQ-PDI as there are only 2 interferograms present. The fringe visibility γ is still unknown. However the results shown in figure 5.8 can be used to obtain the remaining unknown experimentally. The gradient obtained from a linear fit applied to the data points measures the fringe visibility γ. Unknown phase distortions can now be measured by using these results to determine the exact value of the phase distortion present.

5.4.1 Detecting unknown phase

The QHQ-PDI can be used to measure unknown phase distortions within the operating range 2.3λ to 3.3λ. This is tested by applying various phases within 2.3λ to 3.3λto the Hex 127 centre pixel, while the surrounding ones are held at 14V. The

PDI output $\frac{I_A - I_B}{I_A + I_B}$ is then recorded for each point and the slope obtained previously from figure 5.8 is used to determine the value of the phase on the Hex 127. This measured phase value from the QHQ-PDI is compared to the actual phase present on the Hex127 in table 5.1. The third column shows the detection error by taking the difference between the detected phase and the actual phase present.

Detected	Actual	Residual
2.46	2.40	0.06
2.55	2.57	-0.02
2.63	2.67	-0.04
2.80	2.88	0.08
2.92	3.03	-0.11
3.06	2.91	0.15
3.17	2.98	0.19

Table 5.1: *Residual phase errors*

For a larger sample of phases detected, the rms error is 0.103λ. This shows that the PDI is able to detect the phase distortions to an accuracy of $\frac{1}{10}$ of a wave.

5.4.2 Operating with more than one pixel

In a real AO system the phase distortions are present over the entire beam area as opposed to the phase distortion being a single pixel with a flat surround as considered so far. To verify the phase can be detected over an area containing more than one pixel, the centre 7 Hex 127 pixels are used (pixels 1 to 7 in figure 5.1). The aperture control shown in figure 5.4 is set to illuminate these 7 pixels. Voltages from within the operating region are then sent to these pixels simultaneously such that the pixels do not all have the same voltage on them at the same time and the output $\frac{I_A - I_B}{I_A + I_B}$ for each pixel is recorded, using the geometry matching shown in figure 5.6. This process is repeated so that a range of voltages are applied to each pixel. The results of these are shown in figures 5.9 and 5.10. Again these show that the phase can be recovered from multiple pixels over a 1λ range.

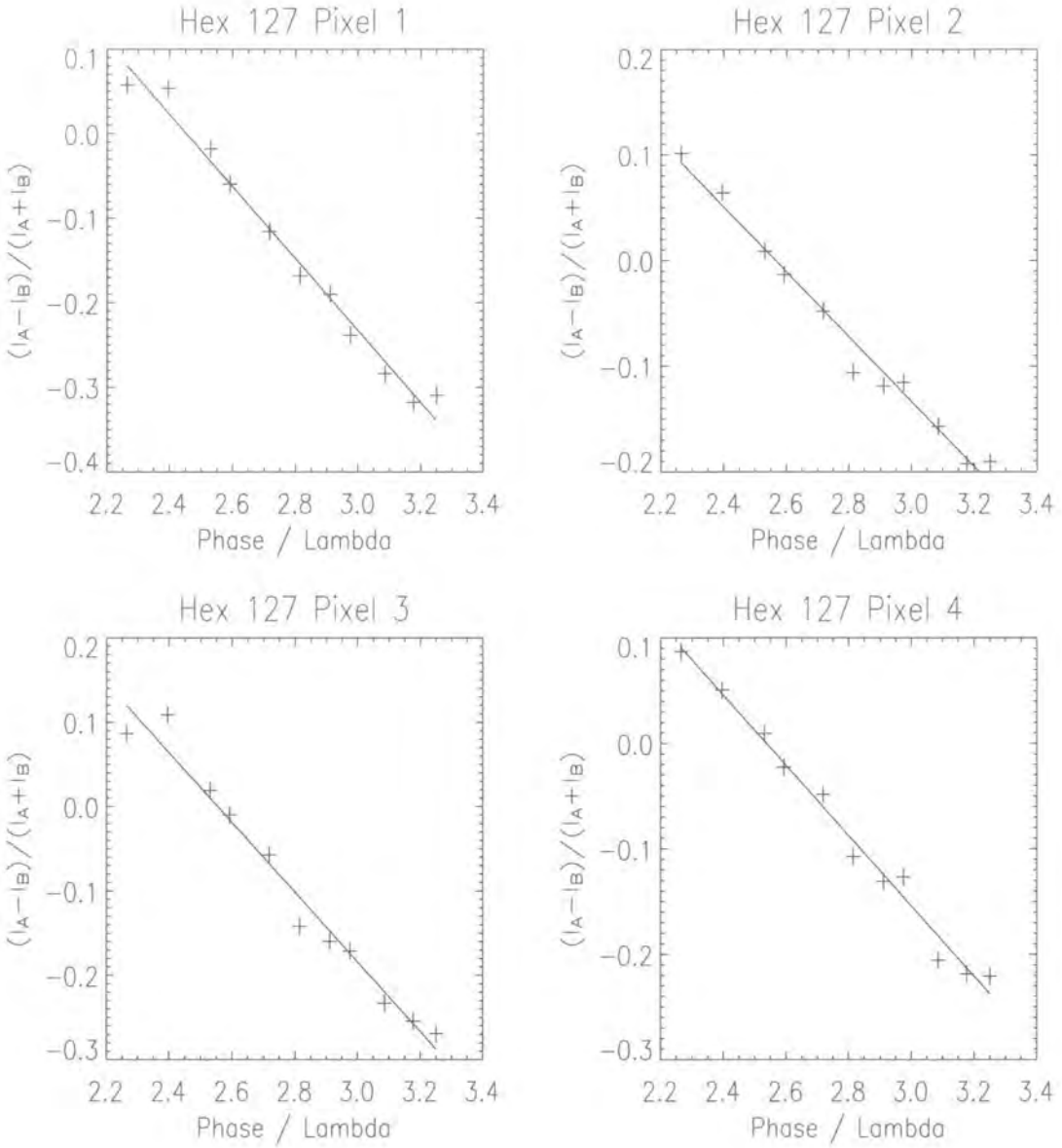

Figure 5.9: *The response for the first 4 Hex 127 pixels for known phase distortions.*

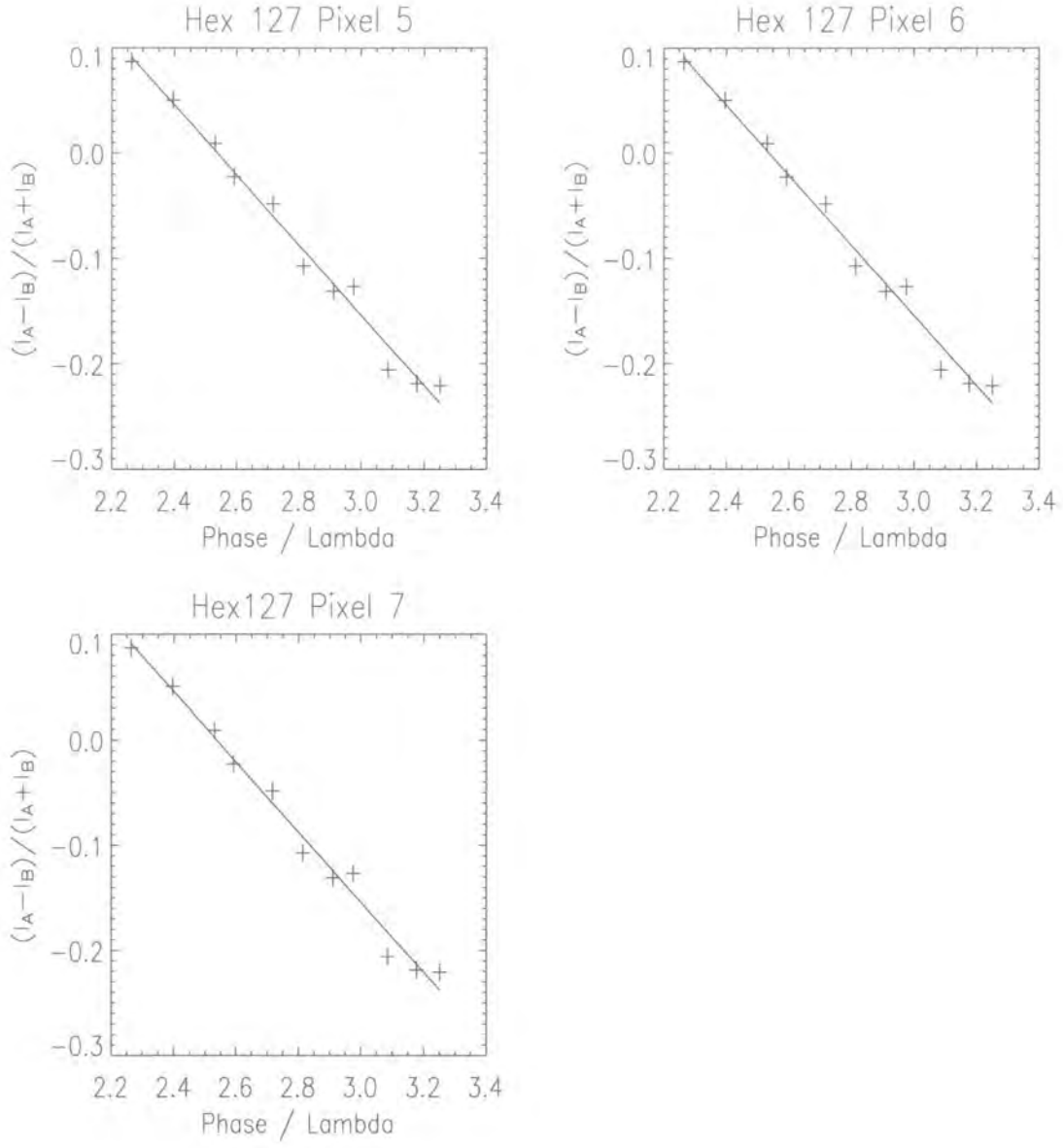

Figure 5.10: *The response for the next 3 Hex 127 pixels for known phase distortions. These show a linear response as was found previously. Linear fits are applied so that the fit parameters can be used to recover unknown phase distortions present on the corresponding pixel*

5.4.3 Residual phase errors

The linear fits shown on the data points in figures 5.9 and 5.10 are used to measure unknown phase distortions on the 7 pixels. Random voltages from within the operating range are then applied to these 7 pixels. These are measured using the QHQ-PDI and the linear fits used to recover the measured phase. The phase detected by the QHQ-PDI is compared to the phase actually applied to each Hex 127 pixel. The difference gives the residual phase error (in waves). The rms of the residual phase error for each pixel is shown in table 5.2. These errors will remain

Hex 127 Pixel	Phase error (λ)
1	0.094
2	0.125
3	0.154
4	0.188
5	0.178
6	0.162
7	0.234

Table 5.2: *The average difference between the detected phase and the actual phase on the Hex 127*

present on the wavefronts after correction. Although the values are larger than those obtained for a single pixel on a flat surround, the next section shows that the system still works and correction is obtained.

5.4.4 Conclusion

These results show that the QHQ based PDI can detect the phase distortions present on a wavefront. Using the results when known phase distortions are initially measured, the actual value of the phase distortion present can be determined to an accuracy of $\frac{\lambda}{5}$ to $\frac{\lambda}{10}$.

5.5 Static wavefront correction

The QHQ-PDI is intended as a WFS in an adaptive optics (AO) system. So far the ability to measure phase has been demonstrated. The next stage is to show that this information can be used to correct a distortion and produce an improvement in the observed image. In a closed loop AO system distorted wavefronts will be incident onto the Hex 127 which is the wavefront corrector. These then are detected in the PDI where the correction is calculated from the 2 interferograms and applied to the Hex 127 to recover a flat wavefront.

The Hex 127 will be utilized as both the wavefront corrector and a means to generate a phase distortion to correct. Flat wavefronts are be incident onto the Hex 127 as before, and a phase distortion is added to the Hex 127 within the operating range 2.3λ to 3.3λ. This is detected by the PDI as in the previous section. The required correction is calculated from the detected phase and applied to the Hex 127 to correct for the initial distortion. The advantage of using the Hex 127 to apply both the initial phase distortion and then correct for itself is that there are no distortions which are undetectable (such as phase distortions greater than one wave) or uncorrectable (If the phase distortion varied with a higher spatial frequency than that of the Hex 127 pixels, then they would not be able to create the required shape. By using the Hex 127 pixels to create the distortions we guarantee the distortions are of the correct spatial frequency). It can be argued that this is unrealistic, however our main purpose here is to test the wavefront sensing concept using the Hex 127. The initial phase distortion remains static as once it is applied it does not vary in time.

5.5.1 Method

Figure 5.11 shows the optical setup used. This is the same layout as used previously but with the addition of the object camera. The aperture remains illuminating the centre 7 pixels only. A non polarizing beam splitter is used to send half of the beam to the PDI and the remainder to the object camera where the corrected beam is observed. Further ND filters are placed before the object camera to prevent

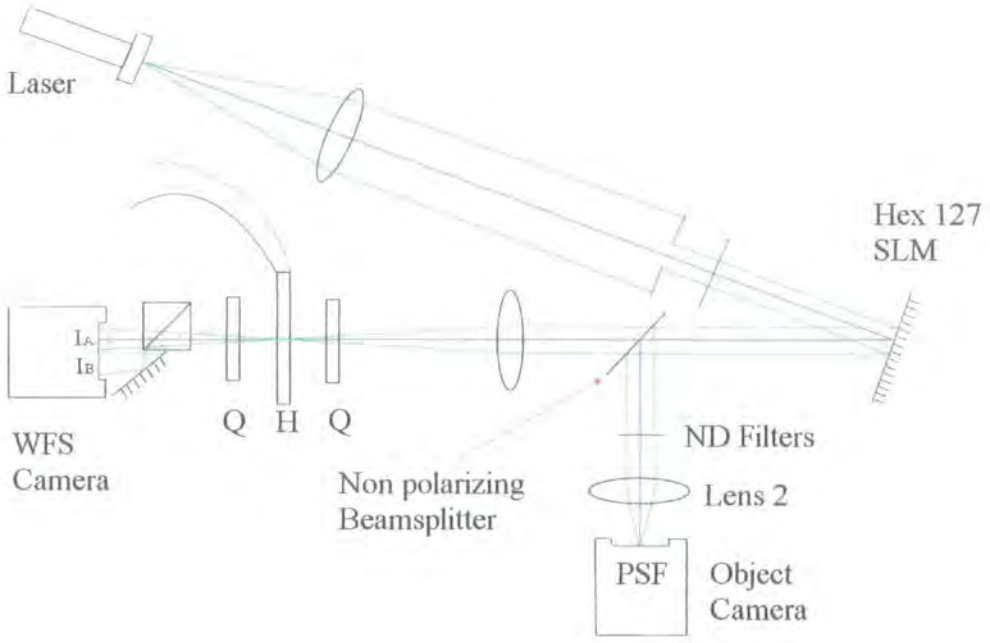

Figure 5.11: *Modified setup, with the addition of a beamsplitter to allow the image to be observed at a second camera. In a real closed loop AO system distorted wavefronts would arrive from the source from where the laser is shown. The unlabelled components are as they are in figure 5.4*

it saturating. Before the first unknown phase distortion is applied to the Hex 127, known phase distortions are applied and the output used to generate the fit parameters required to recover the actual phase value from 2.3λ to 3.3λ. This process creates results such as those shown in figures 5.9 and 5.10. A random phase distortion with phases within 2.3λ to $3.3\lambda$is applied to the Hex 127. This is measured by the QHQ-PDI where $\frac{I_A - I_B}{I_A + I_B}$ is used along with the fit parameters to measure the phase distortion present.

5.5.2 Correcting the distortion

To correct the distortion the phase measured by the QHQ-PDI must be subtracted from the corresponding pixel on the Hex 127. In order that the resulting wavefront

has phases within the operating region a constant phase of 2.8λ is added. 2.8λ is chosen so that the corrected flat wavefront lies within the operating region 2.3λ to 3.3λ. Adding the same constant to every pixel has no effect on the observed image.

The correction is applied by calculating the residual error that is left over when the detected phase is subtracted from the Hex 127. This residual phase error is then converted to a voltage and sent the Hex 127. The residual phase, $\phi_{err,pix}$ is given by,

$$\phi_{err,pix} = \phi_{present,pix} - \phi_{det,pix} + \phi_{flat},$$

where $\phi_{present,pix}$ is the original phase distortion present on the Hex 127 pixel, $\phi_{det,pix}$ is the phase detected by the QHQ-PDI and ϕ_{flat} is the desired corrected phase.

5.5.3 Measuring the improvement in image

The effectiveness of how well the system has corrected the distortion is determined by measuring the peak intensity of the PSF. A 2D Gaussian is fitted to each PSF and the height measured. The ratio of this intensity to that of the ideal PSF is the Strehl ratio for the image. Figure 5.12 shows the PSF imaged with the Hex 127 in a powered off state. This is considered as the reference PSF with a Strehl ratio of 1. The Strehl ratio for this reference will not be exactly 1 as some distortions will still be present due to the optical components and external vibrations.

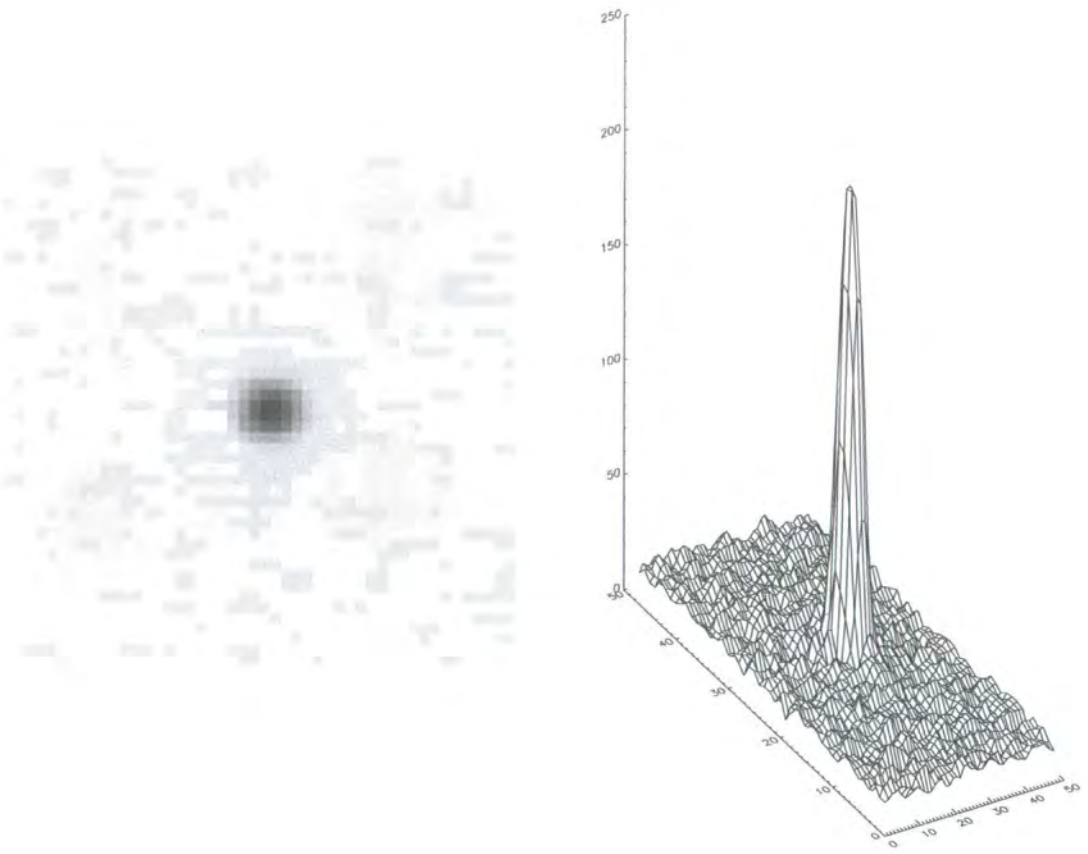

Figure 5.12: *PSF created with no distortions present. This is the reference PSF, shown as an intensity plot (left) and a surface plot (right).*

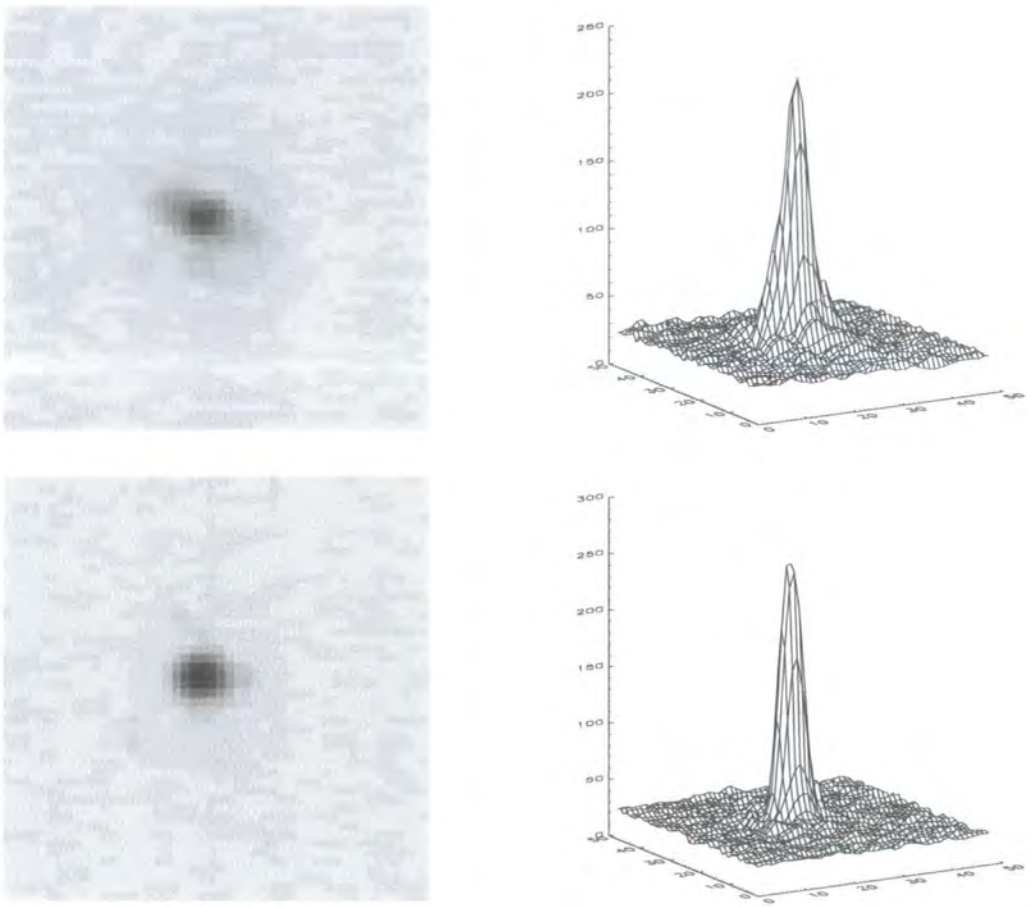

Figure 5.13: *Top line is with a phase distortion applied to the Hex 127, the bottom line is with the correction then applied. The ratio in central intensities show an improvement in Strehl ratio of 1.35.*

The top line of plots in figure 5.13 show the PSF created for a random phase distortions applied to the Hex 127. The initial phase distortions vary up to $\frac{\lambda}{2}$. The bottom line show the resulting PSF after the correction has been calculated and applied. The correction has a residual phase error of 0.1λ meaning that the calculated correction has phase variations of $\frac{\lambda}{10}$ relative to the flat wavefront across the surface. This is derived from the pixel voltages remaining on the Hex 127. The central intensity in the uncorrected PSF has a ratio of 0.735 relative to the reference PSF. The corrected PSF has a ratio of 0.9910 relative to the reference PSF showing an improvement of 1.35.

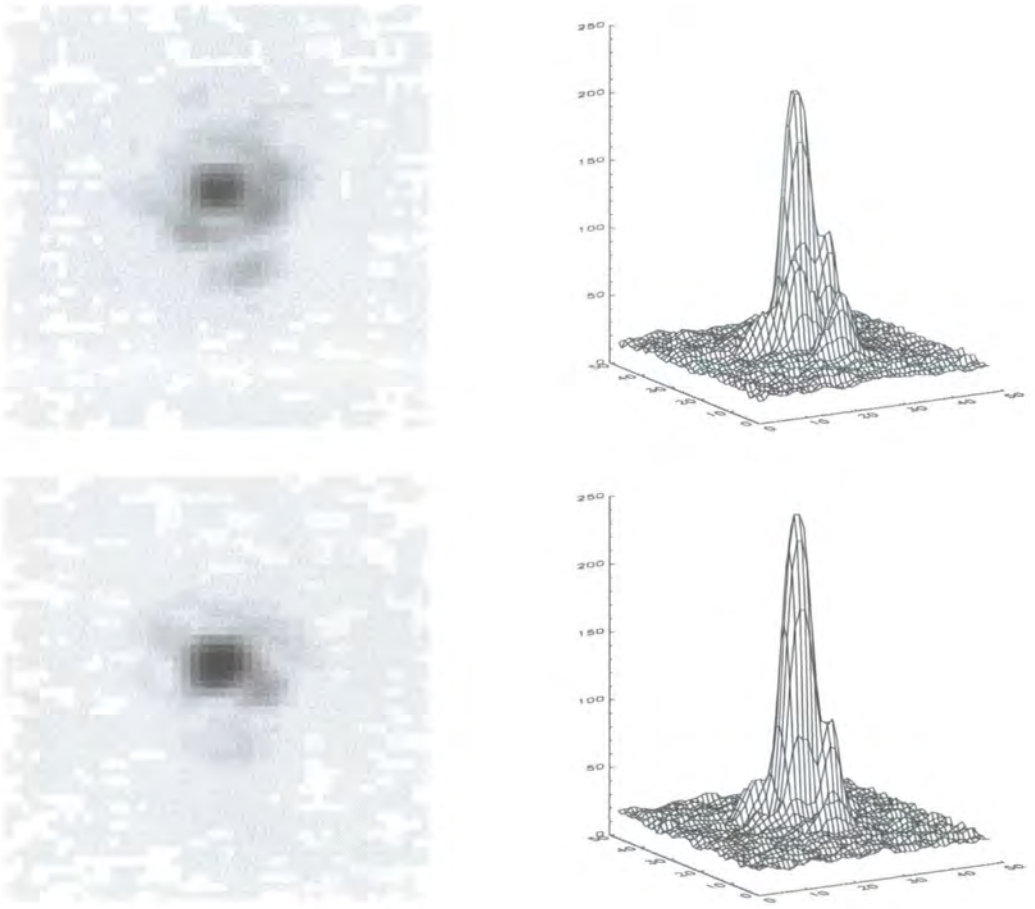

Figure 5.14: *PSF created with larger initial phase distortions than in figure 5.13. The top plots are for the uncorrected case, the bottom ones are the corrected case showing an improvement in Strehl ratio of 1.58.*

The top line of plots in figure 5.14 shows the PSF created with larger initial phase distortions present on the Hex 127, varying up to $\frac{3\lambda}{4}$. It can be observed that a significant amount of light has been scattered away from the central peak which will severely limit the resolution of an extended image. The central intensity has a ratio of 0.577 relative the the reference PSF. The bottom line shows the obtained corrected PSF's in this case with a ratio of 0.9124 to the reference PSF showing an improvement of 1.58.

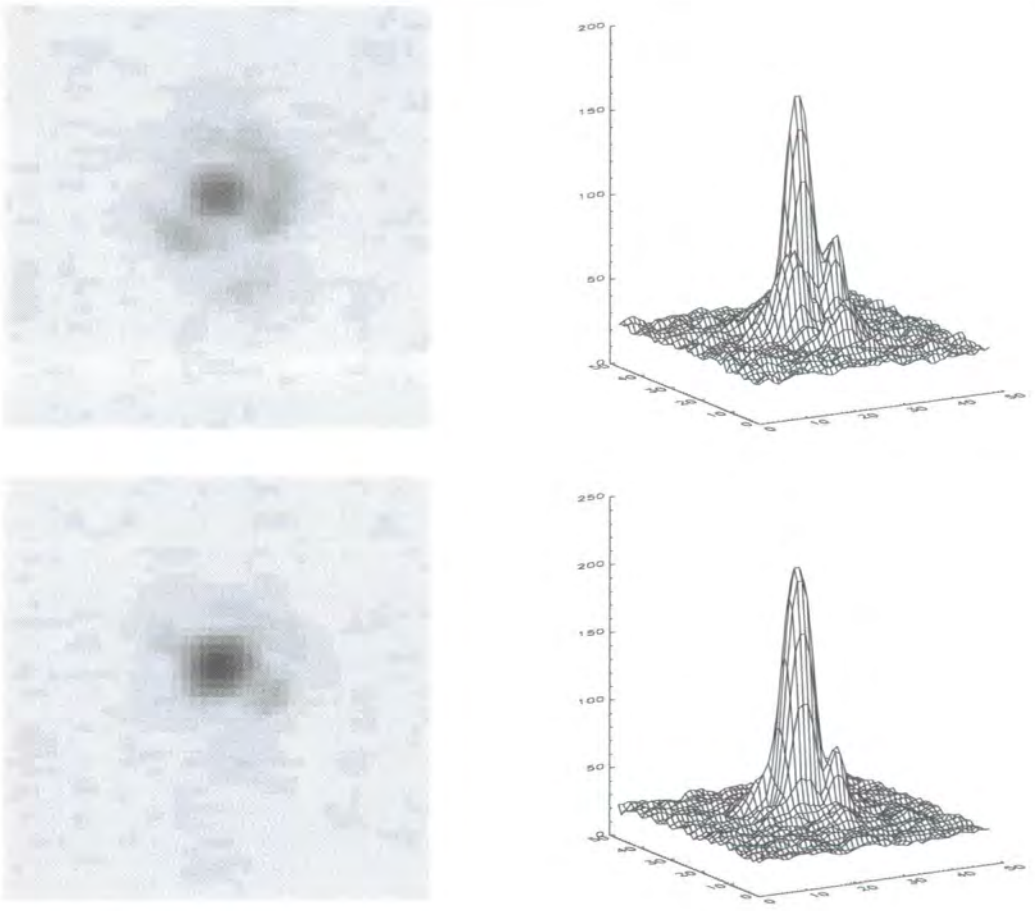

Figure 5.15: *PSF created with phase distortions varying by up to* 1λ *are present in the initial distortion. The top plots are for the uncorrected case, the bottom ones are the corrected case showing an improvement in Strehl ratio of 1.86.*

The top line of plots in figure 5.15 shows the PSF created when phase distortions up to $1\lambda$are applied. The intensity of the central peak has a ratio of 0.516 relative to the reference PSF. The bottom line of plots show the corrected PSF with a ratio of 0.958 relative the reference PSF showing an improvement of 1.86. An iterative approach was also tested by re measuring the residual error with the QHQ-PDI and calculating a new correction from these. This was found to have an insignificant effect mainly due to the error in determining the phase shown in table 5.2.

5.6 Conclusion

This chapter has shown that the PDI used as a wavefront sensor is able to detect phase distortions, and provide enough information to correct for them. Although the improvement ratio between the uncorrected and corrected PSF is only of the order 1.5, the main limitation is that the corrected PSFs are approaching the theoretical maximum i.e. that of the reference PSF. The initial distorted PSFs would be considered a good image in a real astronomical telescope.

This chapter has shown one requirement for an AO system in that the QHQ-PDI coupled with a LC-SLM can correct spatial phase distortions for initial phase distortions over 1 wave. This is consistent with using a PDI based wavefront sensor to measure distortions after an initial stage AO system has removed larger lower spatial frequency distortions. The other requirement is that an AO system can correct for time varying phase distortions as the atmosphere is constantly changing. The next chapter describes and tests a method to use the QHQ-PDI coupled with the Hex 127 to correct for time varying distortions.

Chapter 6

Dynamic wavefront sensing and correction

6.1 Introduction

This chapter will demonstrate the dynamic capabilities of the interferometer (QHQ-PDI) outlined in chapter 4 as the wavefront sensor (WFS) and the Hex 127 wavefront corrector operating as a closed loop adaptive optics (AO) system. An external turbulence source is used to create continually varying phase distortions which are measured and corrected by the AO system. The AO system operates as a closed-loop where the incoming distorted wavefronts firstly have a corrective phase added then the resulting wavefronts are measured by the QHQ-PDI where an updated correction is calculated. For simplicity the AO system will only operate over a single channel i.e. correction will only be applied to a single pixel on the Hex 127 and the corresponding area on the interferograms used for wavefront sensing.

As described in chapter 3 Langlois (56) has previously shown high spatial correction using a Mach Zehnder interferometer as the WFS although not at high speed. Restaino (69) showed a dual frequency (see below) LC AO system using a Shack Hartmann (SH) WFS. The Strehl ratio was improved from 8% up to 34% by the system. Correction was not achieved at high speed, only at about 20Hz. The main limitation to the correcting speed was the control system being based on a SH with a wavefront reconstructor rather than the LC itself. Kirby and Love (70) showed high speed operation of a dual frequency LC where phase shifts of upto half a wave were obtained at 120Hz. However their system was not an AO system. This chapter shows that high speed correction using interferometry coupled with

an LC-SLM suitable for AO is achievable.

6.2 Dual Frequency Operation

In order to operate at speeds sufficient for closed loop AO, the dual frequency nature of the Hex 127 liquid crystals is required. In a nematic liquid crystal (NLC) cell described previously the time required for the molecules to relax back to align with the alignment layers is much slower than that required for the molecules to rise up on application of an electric field. This fall time is too slow for good closed loop AO operation.

Various methods exist to speed up the switching time of LCs (71)(72). The best method discovered so far is a dual frequency NLC of which the Hex 127 is such a device. A LC material is selected which has a low frequency inversion of the sign of its dielectric anisotropy. When the applied electric field's frequency is below this inversion frequency the molecules rotate one way, whilst above this inversion frequency, for the same electric field strength and direction, the molecules rotate the other. However a high frequency electric field can only be applied for a short time otherwise overheating can occur which can damage the LC layer.

6.2.1 High speed wavefront correction

When a voltage/frequency is applied to the LC which applies to a specific phase value (as shown in figure 5.3) the rate of change of the phase shift on the LC gets slower as it approaches this phase value. For high speed wavefront correction the fastest possible phase shifting times are more useful. The fastest phase change on a dual frequency NLC is obtained when a signal corresponding to either of the two extremes of the phase range is applied. The problem is knowing when to stop the LC at the required phase. When a high voltage, low frequency signal is applied this causes the molecules to rotate away from the alignment direction to align fully with

the electric field at the fastest rate and hence turn the LC cell on. When a high voltage, high frequency signal is applied this causes the opposite, i.e. turns the LC cell off.

The method used to implement the fastest phase changes when using the hex 127 as a wavefront corrector is based on a method demonstrated by Kirby and Love (70) and Naumov (73). The Hex 127 is driven by either a high voltage low frequency signal or a high voltage high frequency signal thereby ensuring the fastest phase changes. The voltage applied was chosen as 40 V as this was the maximum suggested voltage for the Hex 127. The phase recorded by the QHQ-PDI, ϕ_{det},[1] is compared to a reference phase value, ϕ_{ref}, where ϕ_{ref} is the desired corrected phase. If $\phi_{det} < \phi_{ref}$ then the Hex 127 is sent a signal to increase the phase such that ϕ_{det} is driven up towards ϕ_{ref}. If $\phi_{det} > \phi_{ref}$ then the Hex 127 is sent a signal to decrease the phase such that ϕ_{det} is driven down towards ϕ_{ref}. At any given instance the feedback is always working to minimize the error signal $\phi_{det} - \phi_{ref}$. At any given instance in time the Hex 127 is always either "turning on" or "turning off". This is sometimes referred to as a "Bang-Bang" system. Which Hex 127 driving frequency corresponds to which condition, $\phi_{det} < \phi_{ref}$ or $\phi_{det} > \phi_{ref}$, is determined from the actual physical setup. Although this method can never hold a constant phase value on the Hex 127 this is not a concern as the initial phase is continually varying. This also helps with the overheating problem when using high frequency signals as the driving signal is continually switching between high and low frequency.

[1]Note: In closed loop operation ϕ_{det} is not the phase on the Hex 127 but the resulting phase after the initial distortion has been corrected by the Hex 127.

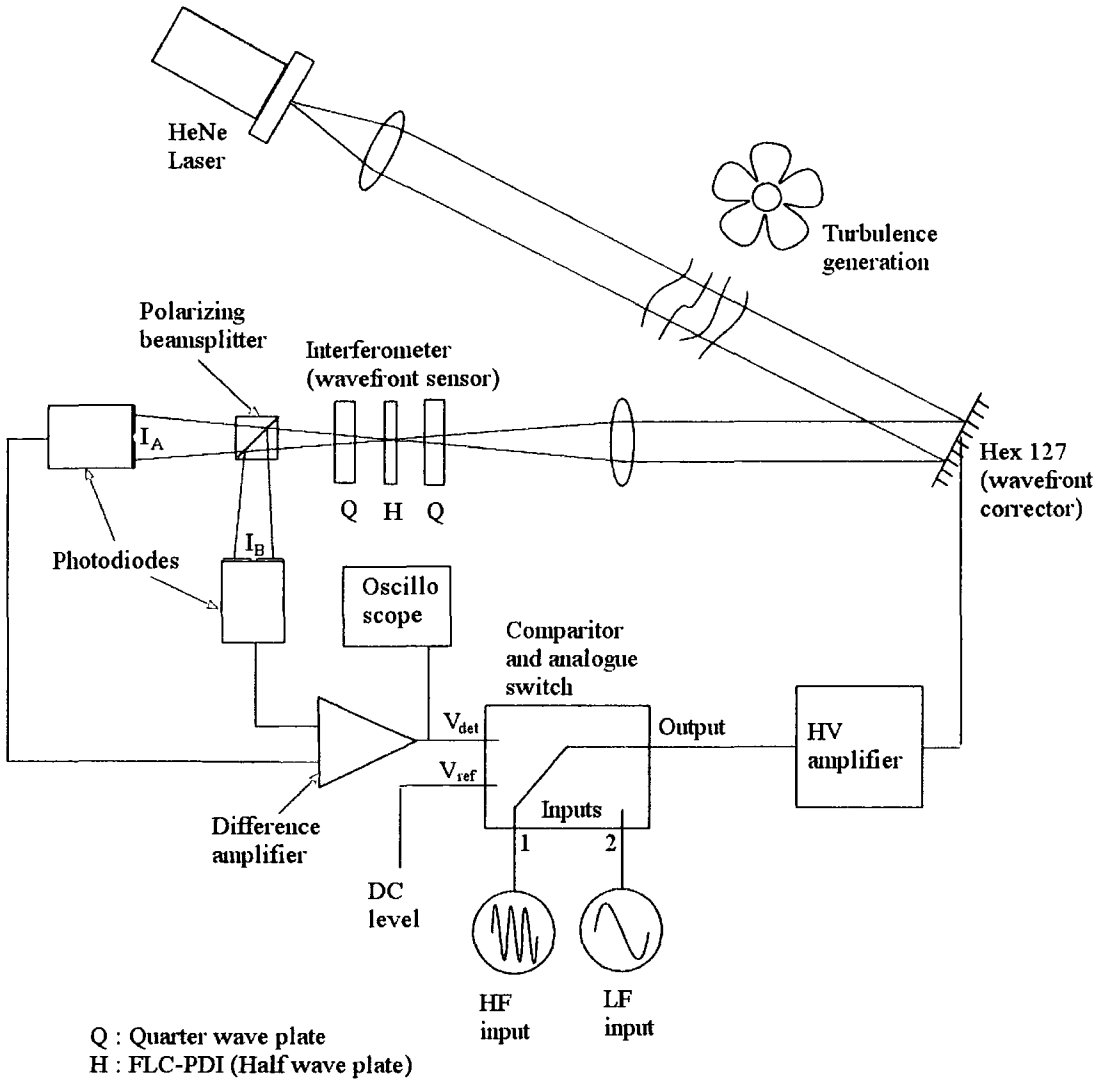

Figure 6.1: *Experimental layout for the closed loop AO system.* V_{det} *is the voltage corresponding to the phase measured by the QHQ, and* V_{ref} *corresponds to the desired corrected phase. The comparator switches between a low frequency (LF) and a high frequency (HF) driving signal depending whether* V_{det} *is above or below* V_{ref}*. The feedback loop applies the correction to the Hex 127 to minimize the difference* $V_{det} - V_{ref}$*. The QHQ is as previously described. The FLC PDI is maintained in the on state while the AO system is running.*

6.3 Optical layout

Turbulence is generated by using a fan and heater which blows warm air across the laser beam. In order to simplify the AO system, the correction takes place on one channel only. Correction is therefore only applied to a single Hex 127 pixel with the wavefront sensing taking place using the corresponding area on the interferograms. By operating with only one pixel a pair of photodiodes can be used to record I_A and I_B. These are positioned such that the area on the interferogram corresponding to the selected pixel on the Hex 127 illuminates the active area on the photodiodes. This is done by using the applying a phase shift to the Hex 127 centre pixel so it can be observed by eye in the interferogram. The photodiodes are then carefully aligned such that they only sample the centre pixel and none of the surrounding ones. Each photodiode outputs a voltage proportional to the intensity (and hence the phase) present. The main motivation for using a pair of photodiodes is that the video camera employed in the previous chapter cannot read out fast enough for high speed correction. Using a single channel also simplifies the electronics required for control. Figure 6.1 shows the experimental layout. The outputs of the photodiodes is fed into a difference amplifier which performs the operation $I_A - I_B$ and amplifies the resultant signal. This output is proportional to the phase measured by the QHQ-PDI. Unlike previously, the output is not normalised with $I_A + I_B$ as this keeps the design of the electronics simple while retaining all of the required information. The comparator/switch is where the actual control of the AO system takes place. The inputs to the comparator/switch are the high and low frequency signals which drive the Hex 127 pixel via a high voltage amplifier. The comparator/switch takes the output signal from the difference amplifier (shown as V_{det} in figure 6.1) and compares this to a reference voltage (shown as v_{ref}). This reference voltage is set such that it is the voltage output from the difference amplifier when the phase detected by the QHQ-PDI is that of the desired corrected level. If V_{det} is less than V_{ref} then the comparator/switch switches the output to one of the inputs. If V_{det} is greater than V_{ref} then the other input is switched to the output. The physical connections to which input the high and low frequency drive voltages are connected to is determined from operating the system. As described above the

inputs are connected such that they are switched such that V_{det} is driven towards V_{ref}.

6.4 Results

Since correction is only applied to a single pixel which represents a small area on the beam cross section any correction applied will not show in the PSF due to the large area which remains uncorrected. The residual wavefront error left on the wavefront at the corrected pixel is viewed as a measure of the correction. The output from the difference amplifier is split with connections to the comparator/switch as detailed above and to an oscilloscope where the detected phase can be viewed. Figure 6.2

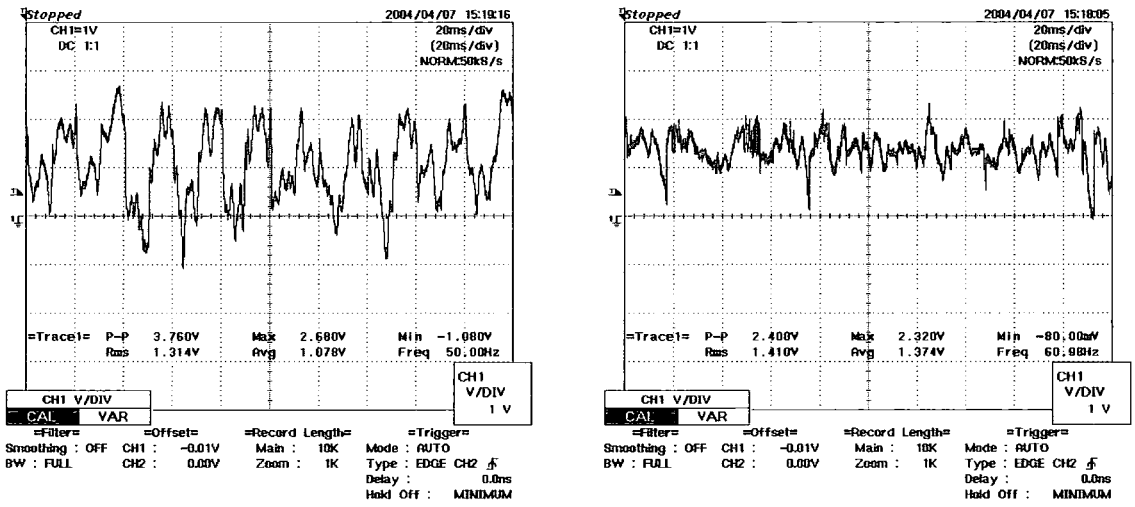

Figure 6.2: *Oscilloscope traces for the uncorrected turbulence on the left and the corrected turbulence on the right. The time base is 20ms per division.*

shows the initial results from the closed loop AO system. The left hand image is the oscilloscope trace obtained from the turbulence alone without any feedback operational. The right hand image is the same trace but with the feedback operational providing correction. It can easily be seen that the right hand trace shows smaller fluctuations suggesting the feedback is correcting the phase. The position and settings of the turbulence generator are set to ensure that the initial phase distortions are $\leq 1\lambda$ so they can be determined by the PDI. This is achieved by initially setting a very small amount of turbulence and increasing it until the distortions are just less than one wave.

The oscilloscope traces show the voltage output from the difference amplifier, however, in order to quantify these results the actual phase distortions are required. As with the results in the previous chapter, the QHQ-PDI does not output the phase directly but a voltage proportional to the phase. Known phase distortions must firstly be measured such that the output voltages can be converted into phase. Two phase values differing by 1 wavelength (λ) are applied alternately to the Hex 127 pixel with no feedback in operation such that the QHQ-PDI response to them can be measured. These are shown in figure 6.3. The maxima and minima have

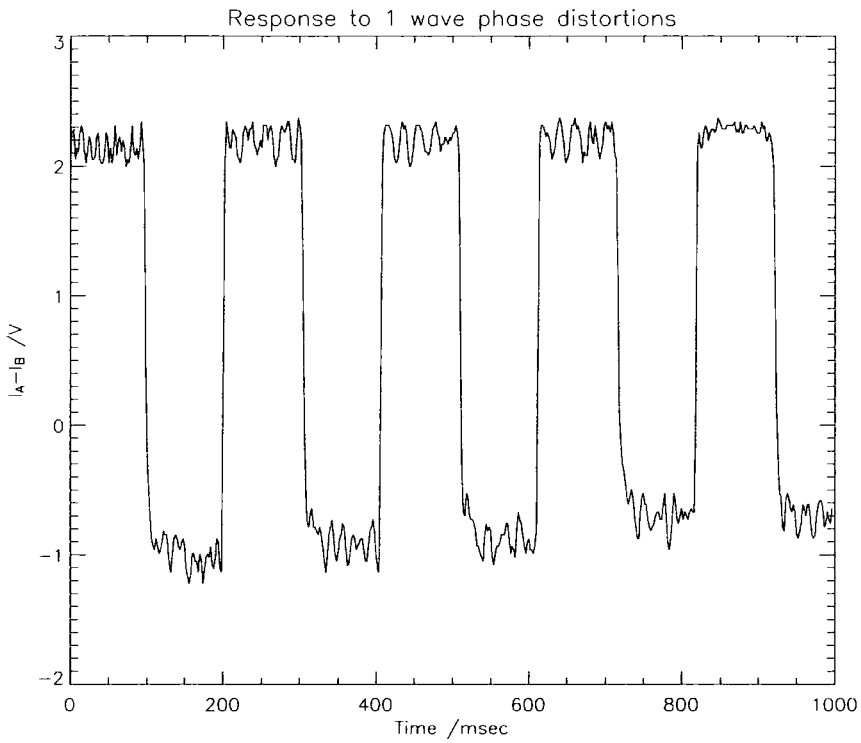

Figure 6.3: *The output from the difference amplifier for known phase shifts separated by 1 wave. The voltage difference between the maxima and minima corresponds to a phase change of* 2π *radians. This is used to enable the root mean squared (rms) phase error to be calculated for uncorrected and corrected turbulence.*

a phase difference of 1λ. The maxima are considered to have a phase of $+\pi$ and the minima a phase of $-\pi$. These are then used to convert the voltage output v_{det} into the actual phase present. Figure 6.4 shows that the oscillations present on

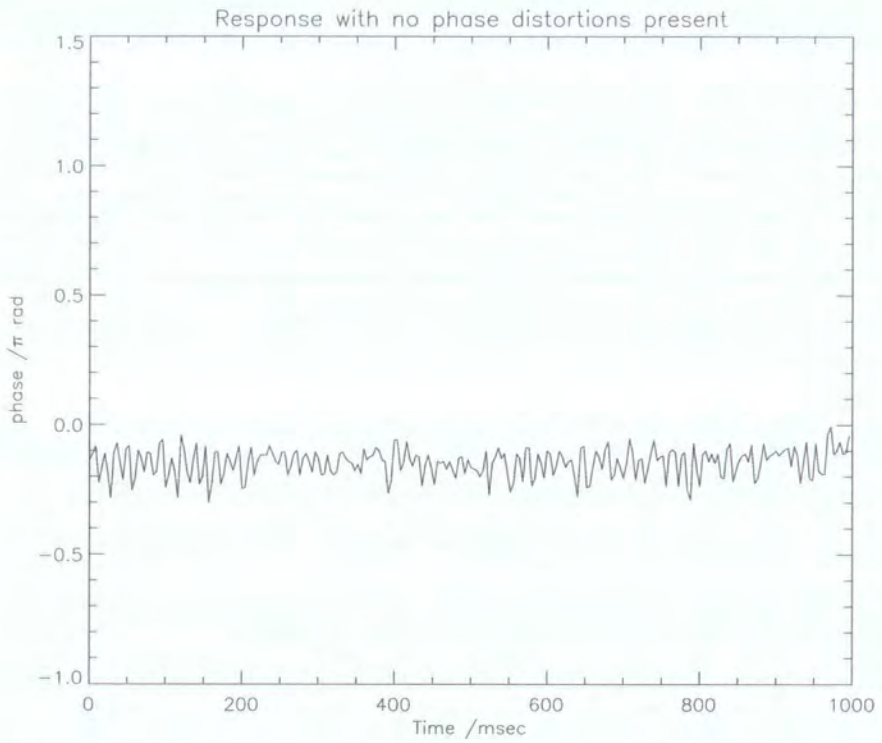

Figure 6.4: *The output from the difference amplifier when there is no phase distortions present on the beam. This shows the same noise oscillations as in figure 6.3. Note the y axis is scaled with phase, not volts as in figure 6.3. The rms of this noise is 0.09744 rad.*

the square wave are noise in the system and are present when there are no phase distortions added onto the laser beam.

6.4.1 Measuring the phase errors

Figure 6.5 shows the residual phase errors before and after correction. The data segment in this case is 200ms long, this is determined by the FLC switching frequency. The rms phase error in the uncorrected case is 1.561 rad and after correction the rms phase error is 0.632 rad. The reduction in rms phase error shows that correction is achieved for the single pixel by the AO system.

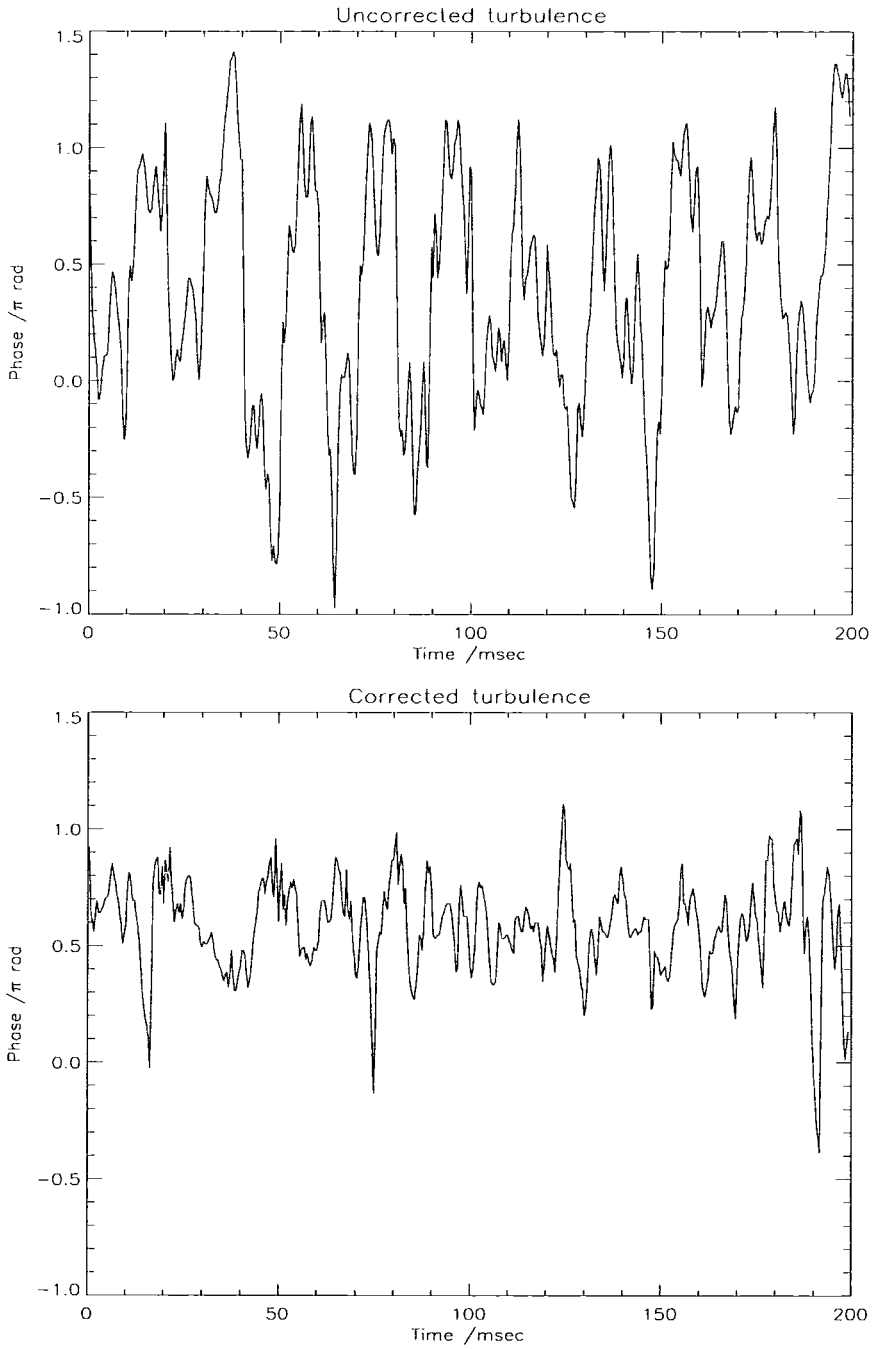

Figure 6.5: *Top: The output for uncorrected turbulence. The feedback loop is not operational allowing the turbulence to be measured. The rms phase error is 1.561. Bottom: The output when the turbulence is corrected using the feedback. This is the residual phase errors left over after correction. The rms phase error is 0.632. The data segment is* 200 ms *long. These are the same results as shown in figure 6.2 but with the voltages converted into phase values. Although large negative spikes can be observed this is statistically random turbulence.*

6.4.2 Strehl Ratio

As detailed previously the Strehl ratio is used to measure the image quality and hence the effectiveness of AO correction. The Strehl ratio is the ratio of the central intensities of the distorted PSF and the diffraction limited case. In this situation the PSFs are unavailable due to the correction only over a small area of the entire beam cross section. However, the Strehl ratio can be obtained directly from the residual phase errors present on the wavefront. For a random Gaussian distortion such as that given by atmospheric turbulence, the Strehl ratio, S is given by (74)

$$S = exp(-\sigma_0^2) \tag{6.1}$$

where σ_o^2 is the variance of the phase errors.

For the rms phase errors obtained from the results in figure 6.5 the Strehl ratios calculated from equation 6.1 are

$$\begin{aligned} \text{Uncorrected} \quad S &= 0.088 \\ \text{Corrected} \quad S &= 0.671 \end{aligned}$$

These Strehl ratios apply for the time varying phase distortions present on the pixel where AO takes place.

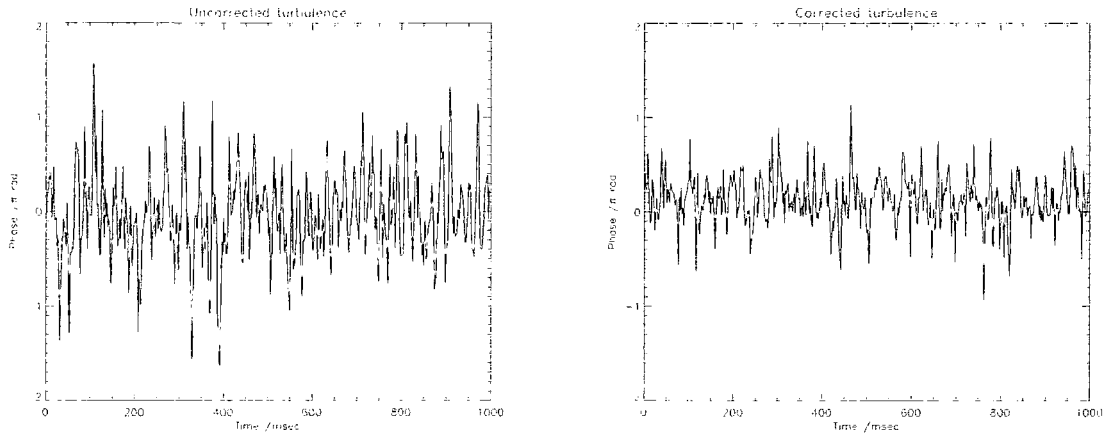

Figure 6.6: *Left: Phase errors for uncorrected turbulence. The rms phase error is 1.481 rad. Right: Phase errors for corrected turbulence. The rms phase error is 0.818 rad. The data segment is* 1 *second long.*

Figure 6.6 shows another pair of results from the closed loop AO system. In this case the FLC switching frequency has been slowed to allow a 1 second data segment. The uncorrected rms phase error is 1.481 rad and the corrected rms phase error is 0.818 rad. The corresponding Strehl ratios given by equation 6.1 are:

$$\begin{aligned} \text{Uncorrected} \quad S &= 0.111 \\ \text{Corrected} \quad S &= 0.512 \end{aligned}$$

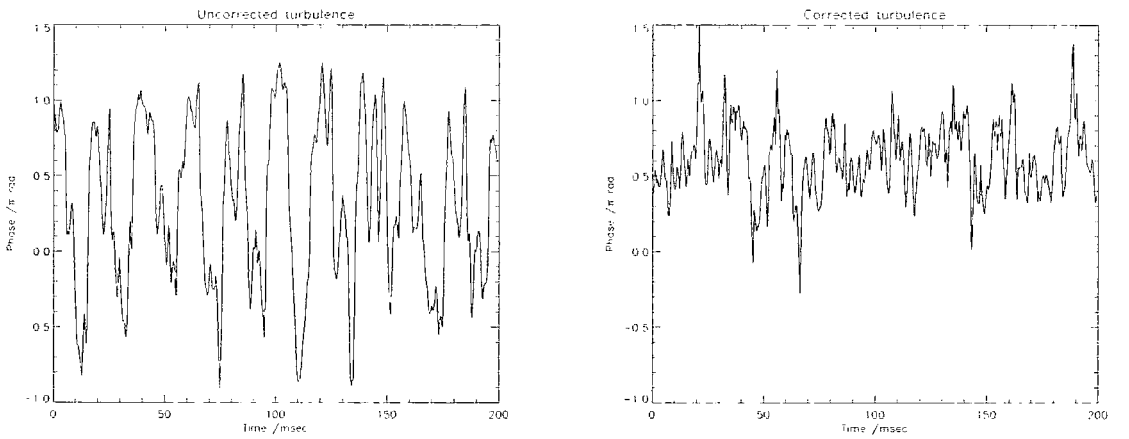

Figure 6.7: *Left: Phase errors for uncorrected turbulence. The rms phase error is 1.701 rad. Right: Phase errors for corrected turbulence. The rms phase error is 0.724 rad. The data segment is* 200 ms *long*

Figure 6.7 shows a final pair of results from the closed loop AO system. The uncorrected rms phase error is 1.701 rad and the corrected rms phase error is 0.724 rad. The corresponding Strehl ratios given by equation 6.1 are:

$$\begin{aligned} \text{Uncorrected} \quad S &= 0.055 \\ \text{Corrected} \quad S &= 0.592. \end{aligned}$$

The Strehl ratios obtained above, while not at the Marechal limit (Strehl of 80%) are still considered to be well corrected.

6.4.3 Power Spectra

The power spectra associated with the results presented previously are shown next. Figure 6.8 shows the power spectrum obtained for the phase errors obtained in figure 6.5. The y axis is a logarithmic scale and the central peak at 0Hz corresponding to the DC level has been omitted due to the fact that most of the power exists there. This constant level arises from the reference level set by the comparator/switch.

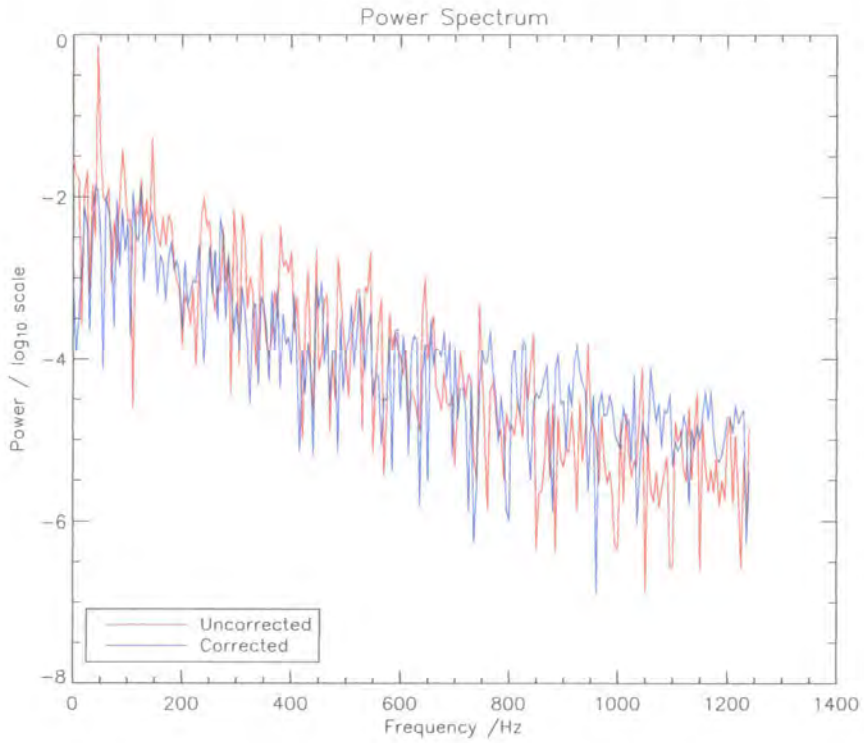

Figure 6.8: *Power spectra obtained from the phase errors shown in figure 6.5. The 0Hz spike has been omitted.*

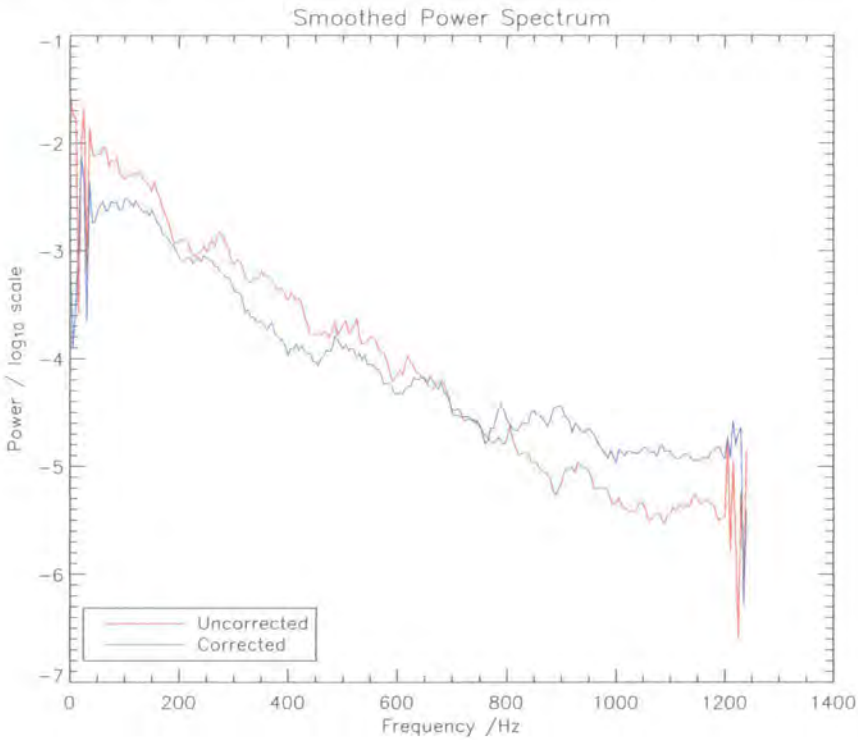

Figure 6.9: *Smoothed version of figure 6.8. Frequencies below 700Hz are corrected, while higher frequencies actually get slightly worse.*

Figure 6.9 shows the same power spectrum after smoothing. This shows that for lower frequency time varying distortions the power is reduced and hence corrected by the AO system. For high frequencies the correction actually makes it slightly worse, but these have powers 2 orders of magnitude less than the lower frequencies where correction is obtained. The crossover frequency where the correction becomes ineffective is 700Hz.

Figure 6.10 shows another example of the obtained power spectrum and the smoothed power spectrum. These show a similar pattern although the frequency at which AO correction ceases is not so well defined but is still around 700Hz.

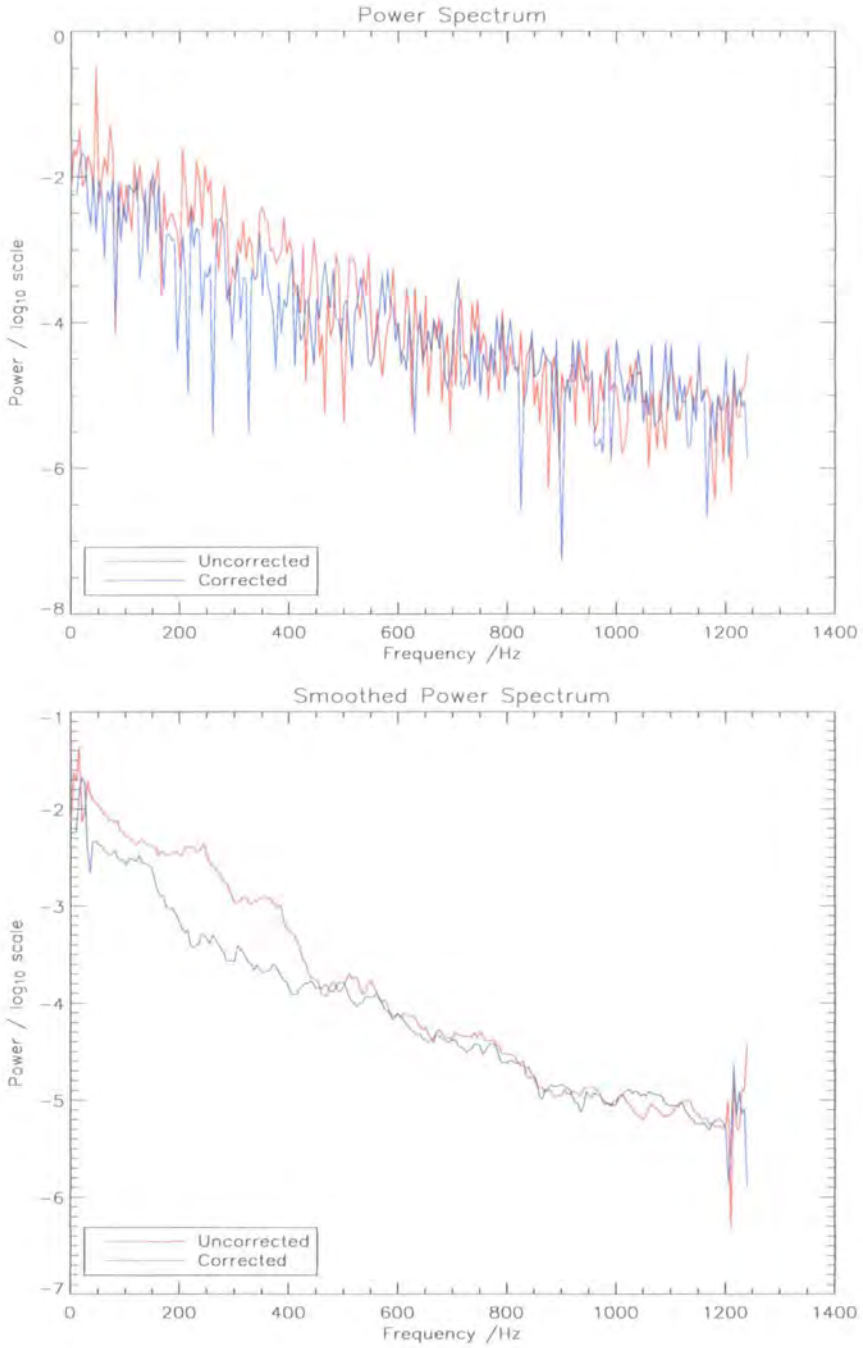

Figure 6.10: A 2^{nd} example of the power spectrum obtained from the AO system. The bottom plot is the smoothed version of the top one. These show a similar pattern to those in figure 6.9.

6.5 Conclusion

The results show that a good improvement in Strehl ratio is obtained with this AO system. The non linear relationship between the rms phase error and the Strehl ratio means that just reducing the rms phase error does not guarantee good correction. Good correction is obtained by reducing the rms phase error towards 0.5 rad which corresponds to a Strehl of 80%. In some cases the results show that the rms phase error has only been improved by a factor of ≈ 1.5, however the Strehl ratio improves from less than 10% to in excess of 50%. This is considered good correction even though it is not at the Marechal limit (a Strehl of 80% or better).

One drawback of only using 2 interferograms for wavefront sensing is that the actual value of the phase is not recovered directly. The phase is recovered by initially measuring known phase distortions against which to compare. This is not an issue with this AO method as the actual phase distortions are only required to enable the Strehl ratio to be calculated. The AO system functions by simply comparing the output from the QHQ-PDI to the reference voltage.

In this AO system the correction has only been implemented on a single channel. One of the major advantages of this type of AO system is the reconstructor free operation where each channel is independent of the neighbouring ones. Further channels would be added simply by adding additional pixels to the QHQ-PDI using perhaps fast video cameras in place of the photodiode and using the corresponding pixels on a zonal LC-SLM such as the Hex 127 used here. The electronic control here would be repeated for each channel, although it is more likely a computer would be used to perform the task of the comparator/switch on numerous channels.

The Strehl ratios above are calculated for the single pixel where correction operates. As outlined above a full AO system would consist of multiple channels all operating in the same manner. Similar correction would be expected across all channels such that the Strehl values calculated are considered representative for the entire beam and thus the final image formed by an AO system.

The power spectrum shows that for temporal frequencies above $\approx 700Hz$ correction is no longer achieved. This means that this AO system is able to correct for time varying distortions up to 700Hz. The turbulence generated by blowing warm air across the initially undistorted beam can be considered similar to atmospheric turbulence. Above 700Hz the effect of the AO system is to make the phase errors worse. This is typical of an AO system and is not a point of concern as most of the power is shown to exist at lower frequencies where good correction is needed and achieved.

These results show that an AO system using a QHQ-PDI coupled with a dual frequency LC SLM controlled in this "Bang-Bang" style of operation is sufficiently fast enough to correct for atmospheric turbulence.

Chapter 7 | *Conclusion*

7.1 Summary

The aims of this thesis were to evaluate the functionality of components suitable for use in an extreme AO system. The AO system comprises of a novel phase shifting interferometer based on a liquid crystal (LC) waveplate as the wavefront sensor (WFS) and a zonal LC spatial light modulator (SLM) as the wavefront corrector. The AO system was investigated in two parts: firstly the spatial capability was tested by measuring static phase distortions and secondly the operating speed was tested by correcting turbulence over a single pixel on the corrector.

The spatial capability of the interferometer with a LC-SLM as an AO system was investigated in chapter 5. The utility of the interferometer to detect phase was firstly shown by measuring known phase distortions. This information was then used to show that an unknown phase distortion can be measured and the phase recovered. Since the interferometer only creates two phase shifted interferograms it is not possible to recover fully the phase from the interferometer output alone. Non time varying phase distortions were measured to an accuracy of $\frac{\lambda}{10}$. This information was then used to correct distortions which were applied to the LC-SLM. The image quality was shown to be improved from an initial relative Strehl of $\approx 60\%$ to a relative Strehl of $\approx 90\%$. Although the improvement ratios were small this is mainly due to starting with small phase distortions which are corrected towards the theoretical maximum. This shows that the interferometer coupled to a LC-SLM can correct over multiple pixels as required for an AO system.

The temporal capabilities of the interferometer with a LC-SLM as an AO system

were investigated in chapter 6. In order that time varying phase distortions could be measured a feedback system analagous to pulse width modulation was described and utilized. This enables the fastest phase change of the LC-SLM to be obtained. This method of control means that the actual phase value is not required overcoming the need to compare to known phase distortions. The interferometer output is simply compared to a reference value corresponding to the desired corrected phase. The feedback is implemented over a single WFS to corrector channel using an analogue circuit. The correction shows an equivalent improvement in Strehl ratio from $< 10\%$ upto $50 \rightarrow 70\%$. It also shows that correction is achieved upto 700Hz. Better correction is shown for lower frequencies where the distortions are larger. This shows that sufficient operational speed is obtained for an AO system. These results show that this AO system is suitable for correcting atmospheric turbulence in the visible wavelengths.

7.2 The sum of the parts make a whole

The aim has been to demonstrate that an AO system based on the described phase shifting interferometer coupled to a zonal LC-SLM is a realistic option for extreme AO. This thesis has shown in two separate instances the spatial and the temporal functionality. A real AO system however needs both attributes together. The design of the AO system whereby each corrector pixel is controlled only by the corresponding WFS area means that a full size AO system with N actuators is simply built by adding additional pairs of corrector pixels / WFS areas. In effect the control matrix for this AO system is diagonal, meaning that the control requirement simply scales as N. This is one of the advantages of this AO system over other more conventional tried and tested AO systems as in these systems the control requirement often scales as N^2 with a non diagonal control matrix. Another major advantage is that LC devices can theoretically be constructed with a large number of pixels. LCs for display purposes currently exist with over a million pixels. The interferograms need to be imaged at a resolution to match the number of pixels with the required frame rate for high speed operation. CCD arrays currently exist with over a million pixels, and provided the readout noise is sufficiently low then

one CCD pixel could be used to control one LC-SLM pixel. The proposed control system for this AO system is that presented in chapter 6. The all analogue system used would not be practical for a system where N is large as the electronic components would have to be duplicated N times and the output from a CCD camera could not be directly connected to multiple difference amplifiers as was done with the photodiodes. A more practical implementation would be to use a computer to perform the function of the difference amplifier and comparator/switch for every pixel/WFS output. The computing requirements simply scale as N. A high voltage amplifier actually to drive the LC-SLM and capable of supplying N independent signals (of either high or low frequency), one for each pixel, would be required. This could become a constraint on the maximum size of N.

The AO system outlined above would be suitable as a secondary system designated to correct small high order distortions. The interferometer operating as proposed cannot detect phase distortions greater than 2π. Although it is possible to use phase shifting interferometry in a manner such that greater phase shifts can be measured, the wavefront would need to be reconstructed. This then means the advantage of reconstructor free operation is not gained and the control matrix in effect becomes much more complex. An initial AO system would be required to correct large low order distortions. It will be important that phase distortions greater than 2π are removed as they will cause an error in the secondary AO system proposed here.

This proposed Extreme AO system offers an alternative approach to the XAOPI system described in chapter 3. The XAOPI system has the advantage that it can correct over a larger wavelength band and that the deformable mirror used can correct faster than a LC device. The LC-PDI system investigated by this Thesis has the advantage that it uses a LC wavefront corrector which should scale to create devices with much larger number of actuators and that the reconstructor free operation means the control requirement is less than for other systems of a similar proposed size.

7.3 Suggestions for continuing this work

The most obvious place to continue is to build an AO system described above which brings together the two sets of results presented here. Continuing with the feedback proposed additional channels can be added such that the actual PSF can be observed to see how it evolves in time as the correction is applied across multiple pixels.

The use of the LC-PDI pinhole off state could be investigated to removed amplitude fluctuations from the beam. The simulation of this showed that if amplitude fluctuations are present on the initial beam then they cause an error in the measured phase. The simulation also showed that data obtained when the LC-PDI is in the off state can be used to reduce these errors. This could be verified experimentally.

Another important aspect which has not been investigated by this thesis is the photon requirements of the QHQ-PDI. The relationship between the number of channels present and how many photons are required for accurate wavefront sensing could be investigated. Is it feasible to use a natural guide star to operate this AO system or would a brighter laser guide star be required?

One final investigation could be that of the white light performance. The qhq-PDI has a design wavelength determined by the waveplates which in this thesis matched that of the laser light used. How is the accuracy of the wavefront sensing affected by using white light?

Bibliography

[1] D. S. Acton, P. L. Wiznowich, P. J. Stomski, J. C. Shelton, O. Lai and J. M. Brase

Laboratory calibration of the W.M. Keck observatory adaptive optics facility

Proc. Soc. Photo-Opt. Inst. Eng (SPIE), **3353**:125 (1998)

[2] J. Spinhirne, D. Anafi, R. Freeman and H. Garcia

Intracavity adaptive optics. 1: Astigmatism correction performance

Applied Optics, **20**:976-984 (1981)

[3] J. Liang, D. R. Williams and D. T. Miller

Supernormal vision and high-resolution retinal imaging through adaptive optics

J. Opt. Soc. Am. A, **14**:2884-2892 (1997)

[4] A. Roorda and D. R. Williams

Nature, **397**:520-522 (1999)

[5] Opto and Laser Europe, **115**:20-21 (2004)

[6] D. L. Fried

Optical resolution through a randomly inhomogeneous medium for very long and very short exposures

J. Opt. Soc. Am, **56(10)**:1372 (1966)

[7] E. Hecht

Optics, third edition

Addison Wesley (1998)

[8] D. L. Fried

Anisoplanatism in adaptive optics

J. Opt. Soc. Am, **72**:52 (1982)

[9] D. P. Greenwood

Bandwidth specification for adaptive optics systems

J. Opt. Soc. Am., **67**:390-393 (1977)

[10] E. Steinhaus and S. Lipson

Bimorph piezoelectric flexible mirror

J. Opt. Soc. Am., **69**:478-481 (1978)

[11] R. P. Grosso and M. Yellin

J. Opt. Soc. Am., **67**:399 (1977)

[12] M. Loktev, D. W. De Lima Monteiro and G. Vdovin

Comparison study of the performance of piston, thin plate and membrane mirrors for correction of turbulence-induced phase distortions

Optics Commun., **192**:91-99

[13] C. Paterson, I. Munro and J.C. Dainty

A low cost adaptive optics system using a membrane mirror

Optics Express, **6**:175-185 (2000)

[14] G. D. Love

Wavefront control using a high quality nematic liquid crystal spatial light modulator

Proc. Soc. Photo-Opt. Inst. Eng. (SPIE), **2566**:43-47 (1995)

[15] J. W. Goodman

Introduction to Fourier optics

McGraw-Hill international editions (1996)

[16] J. Primot and L. Sogno

Achromatic three-wave (or more) lateral shearing interferometer

J. Opt. Soc. Am. A, **12**:2679-2685 (1995)

[17] F. Roddier, C. Roddier and N. Roddier

Curvature sensing: a new wavefront sensing technique

Proc. Soc. Photo-opt. Inst Eng. (SPIE), **976**:203 (1998)

[18] F. Roddier

Curvature sensing and compensation: a new concept in adaptive optics

Applied Optics, **27**:1223 (1988)

[19] Francois Rigaut, Brent L. Ellerbroek and Malcolm J. Northcott

Comparison of curvature-based and Shack-Hartmann-based adaptive optics for the Gemini telescope

Applied Optics, **36(13)**:2857-2868 (1997)

[20] Raymond N. Smartt and Strong J.

J. Opt. Soc. Am., **62**, 737, (1972)

[21] R. Ragazzoni

J. Mod. Opt., **43**:289 (1996)

[22] E.P. Wallner

Optimal wave-front correction using slope measurements

J. Opt. Soc. Am., **73**:1771 (1983)

[23] H. Fearn and A. M. Arroyo

Seeing clearly through the atmosphere

Contemporary Physics, **39**:49-66 (1998)

[24] R. A. Humphreys, C. A. Primmerman, L. C. Bradley and J. Herrman

Atmospheric-turbulence measurements using a synthetic beacon in the mesospheric sodium layer

Opt. Lett., **16**:1367-1369 (1991)

[25] S. L. Valley (editor)

Handbook of Geophysics and Space Environments

Cambridge MA; Air Force Cambridge Research Laboratories, Office of Aerospace Research, USAF

[26] W. Happer
J. Opt. Soc. Am. A, **11**:263 (1994)

[27] F. Rigaut and E. Gendron
Laser guide star in adaptive optics - the tilt determining problem
Astron. and Astrophy., **261**:677-684 (1992)

[28] R. Foy, A. Migus, F. Biraben, G. Grynberg, P.R. Mccullough and M. Tallon
The Polychromatic artificial sodium guide star - a new concept for correcting atmospheric tilt
Astron. Astrophys. Suppl. Series, **111**:569-578 (1995)

[29] R. Ragazzoni, E. Marchetti, and G. Valente
Adaptive-optics corrections available for the whole sky
Nature (2000)

[30] J. E. Nelson
Design Concepts for the California Extremely Large Telescope (CELT).
Proceedings of the SPIE **4004** (2000)

[31] B. Delabre, P. Dierickx, N. Hubin , F. Koch, G. Monnet, M. Quattri, F. Rigaut and R.N. Wilson
The future of filled aperture telescopes: Is a 100m feasable? R. Gilmozzi, Advanced Technology Optical/IR Telescopes VI, SPIE **3352**:778 (1998)

[32] http://www.eso.org/projects/owl/

[33] T. G. Hawarden, D. Dravins, G. F. Gilmore, R. Gilmozzi, O. Hainaut, K. Kuijken, B. Leibundgut, M. R. Merrifield, D. Queloz and R. F. G. Wyse
Critical science with the largest telescopes: Science drivers for a 100m ground-based optical-IR telescope

[34] N. Hubin and M. Le Louarn
New challenges for adaptive optics: The OWL project
Proceedings Backaskog Workshop on Extremely Large Telescopes (Eds T. Andersen, A. Ardeberg, R. Gilmozzi), p 202 (2000)

[35] J. M. Spinhirne, J. G. Allen, G. A. Ameer, J. M. B. II, J. C. Christou, T. S. Duncan, R. J. Eager, M. A. Ealey, B. L. Ellerbroek, R. Q. Fugate, G. M. Jones, R. M. Kuhns, D. J. Lee, W. H. Lowrey, M. D. Oliker, R. E. Ruane, D. W. Swindle, J. K. Voas, W. J. Wild, K. Wilson and J. L. Wyania
The starfire optical range 3.5m telescope adaptive optical system
In D. Bonaccini and R. K. Tyson, editors, Adaptive optical system technologies, **3353**:189 (1998)

[36] C. Shelton, T. Schneider, D. McKenna and S. Baliunas
First tests of the cassegrain adaptive optics system of the Mount Wilson 100-inch telescope.
In D. Bonaccini and R. K. Tyson, editors, Adaptive optical system technologies, **2532**:72 (1995)

[37] J. R. P. Angel
Ground-based imaging of extrasolar planes using adaptive optics
Nature, **368**:203 (1994)

[38] S. M. Stahl and D. G. Sandler
Optimization and performance of adaptive optics for imaging extrasolar planets
APJ Letters, **454**:L153 (1995)

[39] New Scientist, Vol 182 **2441**:40-43 (2004)

[40] Bruce Macintosh, James Graham, Lisa Poyneer, Gary Sommargen, Julia Wilhelmsen, Don Gavel, Steve Jones, Paul Kalas, James Lloyd, Russ Makidon, Scot Olivier, Dave Palmer, Jennifer Patience, Marshall Perrin, Scott Severson, Andrew Sheinis, Anand Sivaramakrishnan, Mitchell Troy and Kent Wallace
Extreme Adaptive Optics Planet Imager: XAOPI
SPIE: "Techniques and instrumentation for detection of extrasolar planets" San Diego CA, USA (2003)

[41] Krulevitch, P. A., Bierden, P. A., Bifano, T. G., Carr, E., Dimas, C. E., Dyson, H., Helmbrecht, M. A., Kurczynski, P., Muller, R. S., Olivier, S. S., Peter, Y-A,

Sadoulet, B., Solgaard, O., Yang, E-H.
Proc. SPIE **4985**:182 (2003)

[42] Poyneer, L.A., Gavel, D. and Brase, J.
J. Opt. Soc. Am., **19**:2100 (2002)

[43] G. D. Love
Liquid-crystal phase modulator for unpolarized light
Applied Optics, **32**:2222-2232 (1993)

[44] Gordon D. Love, Sergio R. Restaino, Richard C. Carreras, Gary C. Loos, Rob V. Morrison, Tom Baur, and Greg Kopp.
Polarization insensitive 127-segment liquid crystal wavefront corrector.
OSA summer topical meeting on adaptive optics. p. 288-290 (1996)

[45] G. T. Bold, T. H. Barnes, J. Gourlay, R. M. Sharples and T. G. Haskell
Practical issues for the use of liquid crystal spatial light modulators in adaptive optics
Opt. Commun., **148**:323-330 (1998)

[46] G. D. Love
Wave-Front control using a high-quality nematic liquid crystal spatial light modulator
Proc. Soc. Photo-Opt. Inst. Eng. (SPIE) **2566**:43-47 (1995)

[47] R. Dou and M. K. Giles
Close loop adaptive-optics systems with a liquid crystal television as a phase modulator
Opt. Lett., **20**:1583 (1995)

[48] T. Shirai, T. H. Barnes and T. G. Haskell
Adaptive wavefront correction by means of all-optical feedback interferometry
Opt. Lett., **25**:773 (2000)

[49] O. Y. Kwon
Opt. Lett., **9**:59 (1984)

[50] H. Medecki, E. Tejnil, K. A. Goldberg and J. Bokor
Phase-shifting point diffraction interferometer
Opt. Lett., Vol **21,19**:1526-1528 (1996)

[51] H. Kadono, M. Ogusu and S. Toyooka
Phase shifting common path interferometer using a liquid-crystal phase modulator
Opt. Commun., **110**:391-400 (1994)

[52] J. Ojeda-Castaneda
Optical shop testing 2nd Edition, Chap 8
Edited by Malacara, D. Wiley, New York (1992)

[53] C. R. Mercer and K. Creath
Liquid crystal point diffraction interferometer for wave-front measurements
Applied Optics, **35**:1633-1642 (1996)

[54] Mark J. Guardalben, Lutao Ning, Nieraj Dain, Devon J. Battaglia and Kenneth L. Marshall
Experimental comparison of a liquid crystal point diffraction interferomter (LCPDI) and a conventional interferometer and methods to improve LCPDI accuracy
Applied Optics, **41** 1353-1365 (2002)

[55] M. Lloyd-Hart, F. P. Wildi, B. Martin, P. C. McGuire, M. A. Kenworthy, R. L. Johnson, B. C. Fitz-Partick, G. Z. Angeli, S. M. Miller and J. P. R. Angel
Adaptive optics for the 6.5m MMT
In Adaptive optics systems technology Editor: P. L. Wizinowich Proc. SPIE **4007**:167 (2000)

[56] Maud Langlois, Roger Angel, Michael Lloyd-Hart, Francois Wildi, Gordon D. Love and Alexander Naumov
High Order Reconstructor Free Adaptive Optics for 6-8 metre class telescopes
From the Proceedings of the ESO Conference on Beyond Conventional Adaptive Optics, May 7-10, Venice (2001)

[57] K. L. Baker, E. A. Stappaerts, S. C. Wilks, P. E. Young, D. T. Gavel, J. W. Tucker, D. A. Silva and S. S. Olivier

Open- and closed-loop aberration correction by use of a quadrature interferometric wave-front sensor

Opt. Lett., **29**:47-49

[58] T. J. D. Oag, M. Langlois and G. D. Love

Wavefront sensing with point diffraction interferometry

Photon 02, 2-5 Sept, OP5.3.1, ISBN 0-7503-0916-4 (2002)

[59] Gordon D. Love and Rajendra Bhandari

Optical properties of a QHQ ferroelectric liquid crystal phase modulator

Opt. Commun., **110**:475-478 (1994)

[60] W. A. Shurcliff

Polarized Light

Harvard University Press (1962)

[61] A. Kolmogorov

Turbulence - Classic papers in statistical theory

Inter-science Publishers Inc, New York (1961)

[62] R. J. Noll

Zernike polynomials and atmospheric turbulence

J. Opt. Soc. Am., **66**:201-211 (1976)

[63] V. N. Mahajan

Zernike circle polynomials and optical aberrations of systems with circular pupils

Opt. Phot. News, 5Engng Lab Notes (1994)

[64] V. N. Mahajan

Zernike annular polynomials and optical aberrations of systems with annular pupils

Opt. Phot. News, 5Engng Lab Notes (1994)

[65] Nicholas Roddier

Atmospheric wavefront simulation using Zernike polynomials

Optical Engineering (1990)

[66] Kelly, T-L. and Love, G.D.

White light performance of a polarization independent liquid crystal phase modulator

Applied Optics **38**:1986 (1998)

[67] *Meadowlark Hex-127 Liquid Crystal Spatial Light Modulator*

Meadowlark Optics, 5964 Iris Parkway, Frederick, CO 80530-1000, USA

http://www.meadowlark.com

[68] *Zygo Corporation ZyMod/PC Phase shift Adapter*

Laurel Brook Road, Middlefield, CT 06455-448, USA

[69] Sergio R. Restaino, David Dayton, Steve Browne, John Gonglewski, Jeff Baker, Sam Rogers, Scott McDermott, Joe Gallegos and Mike Shilko

On the use of dual frequency nematic material for adaptive optics systems: first results of a closed-loop experiment

Optic Express, **6**:2-5 (1999)

[70] Andrew K. Kirby, Gordon D. Love

Fast, large and controllable phase modulation using dual frequency liquid crystals

Optics Express, **12**:1470-1475 (2004)

[71] P. J. Bos and K. R. Beran

The Pi-cell, A fast Liquid-Crystal optical switching device

Mol. Cryst. Liq. Cryst., **113**:329 (1984)

[72] S. T. Wu and C. S. Wu

High speed liquid crystal modulators using transient nematic effect

J. Appl. Phys., **65**:527 (1989)

[73] V. A. Dorezyuk, A.F. Naumov, V.I. Shmal'gauzen

Control of liquid crystal correctors in adaptive optical systems

Sov. Tech. Phys., **34**:1389 (1989).

[74] J. C. Dainty, G. D. Love and C. Paterson

A Short course in Adaptive Optics

4-6 June, Imperial College, London (2001)